Using Circular DIchroism and Fluorescence Spectroscopy to Study the Impact of 2-Aminopurine on RNA Folding

by

JANSON ERICH HOEHER

A dissertation accepted and approved in partial fulfillment of the

requirements for the degree of

Doctor of Philosophy

in Chemistry

Dissertation Committee:

Andy Marcus, Chair

Julia Widom, Advisor

Marina Guenza, Core Member

David Garcia, Institutional Representative

University of Oregon

Winter 2024

DISSERTATION ABSTRACT

Janson Erich Hoeher

Doctor of Philosophy in Chemistry

Title: Using Circular Dichroism and Fluorescence Spectroscopy to Study the Impact of 2-Aminopurine on RNA Folding

RNA is an important biological molecule, with its function helping out with different processes in cells. How RNA functions is related to its structure, with different structured RNA behaving in different ways. Studying RNA structure is thus important to understand its function. One example of this are riboswitches, which help regulate gene expression. By binding a ligand, the riboswitch refolds, causing a change in gene expression. One method of studying RNA structure is by utilizing fluorescent base analogues of the native bases. To study the riboswitch, the fluorescent base analogue 2-aminopurine (2-AP) was substituted into six different locations in the L3 region of the $preQ_1$ riboswitch. Using circular dichroism (CD) and fluorescence spectroscopy, along with fluorescence lifetimes, it was discovered that all modified locations were detrimental to the riboswitch's ability to bind the ligand. In addition, fluorescence-detected circular dichroism (FDCD) was used to study short RNA molecules containing 2-AP, of up to three nucleotides in length. By comparing FDCD to CD, it was determined that in dinucleotides, the fluorescence came almost entirely from unstacked populations. Comparatively, while most of the fluorescence from the trinucleotide came from unstacked populations, some came from stacked populations. Through FDCD and CD, the amount of each construct in stacked and unstacked populations can be determined.

This dissertation includes previously published co-authored material.

CURRICULUM VITAE

NAME OF AUTHOR: Janson Erich Hoeher

GRADUATE AND UNDERGRADUATE SCHOOLS ATTENDED:

University of Oregon, Eugene
SUNY Plattsburgh, Plattsburgh

DEGREES AWARDED:

Doctor of Philosophy, Chemistry, 2024, University of Oregon
Bachelor of Science, Chemistry, 2018, SUNY Plattsburgh

AREAS OF SPECIAL INTEREST:

Spectroscopy
RNA

PROFESSIONAL EXPERIENCE:

Rework Laborer, GlaxoSmithKline, June – July 2014, June – July 2015

GRANTS, AWARDS, AND HONORS:

Emmanuel OMQ Fellowship, Using Circular Dichroism and Fluorescence Spectroscopy to Study the Impact of 2-Aminopurine on RNA Folding. University of Oregon, 2024

PUBLICATIONS:

Hoeher JE, Sande NE, Widom JR. Probing and perturbing riboswitch folding using a fluorescent base analogue. *Photochem Photobiol*. 2024; 100: 419-433. doi:10.1111/php.13896

Widom, J. R.; Hoeher, J. E. Base-Stacking Heterogeneity in RNA Resolved by Fluorescence-Detected Circular Dichroism Spectroscopy. *J. Phys. Chem. Lett.* **2022**, *13* (34), 8010–8018. https://doi.org/10.1021/acs.jpclett.2c01778.

ACKNOWLEDGMENTS

I wish to thank Dr. Julia Widom for her guidance during my PhD and her assistance in the preparation of this manuscript. I would also like to thank Michael Viers for helping to train me and Natalie Sande for helping with experiments. In addition, this would not have been possible without the support of my family. The investigation was supported in part by a National Institutes of Health grant, number R00 GM120457, and by University of Oregon start-up funds, to Dr. Julia R. Widom.

TABLE OF CONTENTS

Chapter Page

LIST OF FIGURES

LIST OF TABLES

CHAPTER I

INTRODUCTION

Biological Significance of RNA and RNA Structure

Ribonucleic acid (RNA) is an important biological macromolecule that was originally determined to be an intermediate between DNA and proteins. There are many different types of RNA with different functions, such as mRNAs that encode proteins, snRNAs that help to catalyze splicing, and siRNAs that mediate post-transcriptional gene silencing.[1,2] RNA is a polymer that includes a negatively charged sugar-phosphate backbone and a series of planar aromatic ring systems called "bases", with the rings differing between bases.[3] Four of the common bases found in RNA are adenine (A), guanine (G), cytosine (C), and uracil (U), which are known as the "native" bases.

RNA structure and function go hand in hand, with the structure determining the function and how flexible the RNA is.[3,4] How RNA folds depends on various factors including base sequence, local structure, local chemical environment, and hydrogen bonding with nearby bases. The most basic property that impacts RNA folding is the specific sequence of bases that make up the RNA, also known as the primary structure.[4] On a larger scale, the structure is determined by hydrogen bonding (known as the secondary structure), and stacking between bases. This leads to specific structural features of RNA such as double helices, which are formed through hydrogen bonding between G and C, and between A and U. The tertiary structure is the global structure of the RNA that defines the 3-dimensional arrangement of all the local structural features. The global and local structure of RNA can be impacted by external factors such as interactions with proteins. In addition, cations can interact with the negatively charged backbone of RNA,

inducing it to fold into a more compact structure, with magnesium being of particularly high biological significance.[5] How the RNA folds determine its function, so understanding RNA function requires experimental methods that probe the aspects of structure discussed above.

Fluorescent Base Analogues

Many useful methods for probing RNA structure are based on fluorescence. One such approach uses modified bases known as fluorescent base analogues (FBAs), which are chemically modified bases that can be substituted in for the native bases. This difference in structure allows the FBA to absorb light at a longer wavelength than the native bases (which have absorption maxima near 260 nm) and causes them to have a significantly higher fluorescence quantum yields. Ideally, FBAs are similar in structure to the native bases, with particular attention to maintaining the functional groups that engage in hydrogen bonding.[6] Several hundred different FBAs have been reported, allowing for different bases to be replaced at specific locations of interest in RNA.[7] This can be used to study local structure in RNA, as the fluorescence is impacted by changes in base stacking and/or hydrogen bonding.[7] The most commonly used FBAs are particularly sensitive to base stacking, which occurs when neighboring bases align with each other on the same side of the backbone and plays an important role in helping to stabilize single stranded RNA.[8–10] Due to their fluorescence intensity changing with changing structure, FBAs can be used to study refolding of RNA.[7]

Different FBAs exhibit different relationships between their photophysics and RNA structure and sequence.[6] Many FBAs are quenched when placed in DNA or RNA, with the extent of quenching being sequence- and conformation-dependent.[7] In stacked structures, interactions with the native bases can change the energies and oscillator strengths of the

electronic transitions of FBAs, as well as altering the potential energy surfaces of the excited states that determine which relaxation pathways are most favorable.[11,12] In addition, some FBAs can change their emission wavelength if the local environmental changes.[6,13]

The most extensively studied FBA is 2-aminopurine (2-AP), which was also one of the first to be discovered back in the 1960s.[6,14] 2-AP is an analogue of adenine, with the location of an amine group changing from position 6 in adenine to position 2 in 2-AP (Fig. 1.1). 2-AP absorbs at ~305 nm and emits at ~370 nm, and has been utilized in both DNA and RNA.[9] While 2-AP is primarily used as an analogue of adenine, it can base pair with cytosine and guanine in addition to uracil, meaning it can be used in place of other bases as well.[9] When free in solution, 2-AP has a fluorescence quantum yield of 0.68, compared to adenine's quantum yield of ~10^{-4}.[9] The fluorescence intensity of 2-AP can decrease by up to 100 times when it is incorporated into RNA or DNA. 2-AP's fluorescence is sensitive to its sequence context. Guanine, the base that most easily undergoes electron transfer to 2-AP, can quench 2-AP from up to ~14 angstroms away,[9,15] while cytosine quenches 2-AP the least.[10,16] In time-resolved fluorescence measurements, 2-AP exhibits multiple excited state lifetimes when incorporated into RNA and DNA, which are impacted by the bases surrounding 2-AP along with whether it is in a single-stranded or double-stranded region.[9,15] The lifetimes are typically shorter in base-stacked and double-stranded environments.[9]

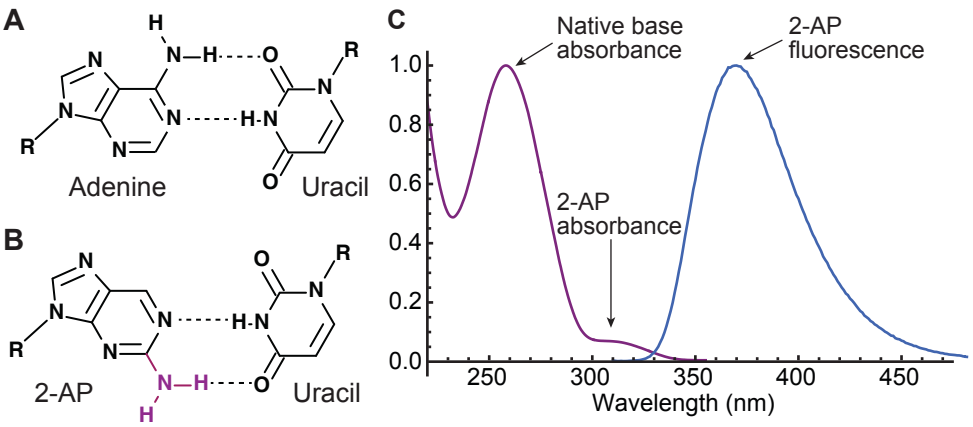

Figure 1.1 A. Structure of adenine base-pairing with uracil. B. Structure of 2-AP base-pairing with uracil. C. Absorbance (purple) and emission (blue) spectra of RNA labeled with 2-AP.

Model RNA Systems under Investigation

The work reported in this thesis pursued the dual aims of studying the fundamental relationship between RNA structure and 2-AP photophysics (Chapter 3), and utilizing 2-AP as a probe in complex RNA structures (Chapter 4). Model systems with limited structural degrees of freedom were used to investigate the nuances of how RNA structure impacts 2-AP photophysics. RNA constructs of up to three nucleotides in length used to investigate RNA in its simplest form.[17] Small RNA constructs like this can help to reveal information about how bases next to each other interact without the influence of larger structural features like a double helix.

Additional consideration arise when fluorophores are used in structures more complex than di- or trinucleotides. For example, their differences in structure from native bases can impact the structure of the RNA being studied, causing it to no longer function properly. Structural impacts are observed with fluorophores other than FBAs as well. For example, adding the dye Cy3 has been shown to over stabilize the helical structure of single stranded DNA, making the bases less accessible for base pairing.[18] This was found to be due to π-π stacking between the DNA bases and the aromatic groups of Cy3. In addition, the location of the

modification impacts the extent of perturbation, with locations closer to important sites like binding pockets where hydrogen bonding plays an important role having more of an impact.[19] Different fluorophores can have different impacts on folding, so a fluorophore can be chosen to have a lesser or greater perturbation on the structure depending on what is being investigated. When working with FBAs and RNA, the FBA can be placed in a weakly conserved region where disruptions to the bases should be of lesser impact, or in a location that can potentially be more disrupting.[20,21] Both options can be of interest. Less conserved regions can be used to study RNA without mutating it, while substitution in more conserved regions can reveal how mutations impact the RNA. In this aim, I used 2-AP to investigate base-stacking in a functional RNA while also characterizing the perturbations it induced.[19]

As a model RNA system for this study, we investigated a riboswitch. Riboswitches are segments of mRNAs that help to regulate gene expression by sensing ligands that include small molecules, ions, and other RNAs. They are most commonly found in bacteria.[22,23] A riboswitch is made up of two domains, an aptamer domain that binds the ligand and an expression platform that refolds in response to ligand binding. This structural change either enhances or suppresses expression of downstream genes, depending on the specific riboswitch. Due to this, investigating the structure of riboswitches and how it relates to their function is an important area of study. Riboswitches can control gene expression at different stages, most commonly at the transcriptional or translational level.[24] The aptamer domain can range in size from around 30 nucleotides in length up to around 250 nucleotides, allowing for the riboswitch to be highly specific in the ligand that it senses.[25] Riboswitches are promising targets to help develop antibiotics due to their control over gene expression, and work has been done to develop synthetic ligands meant to help turn off gene expression.[26,27] Riboswitches are classified based

on the aptamer domain and the ligand they bind, with over 40 different classes known to exist currently.[27,28] The aptamer domain is typically highly conserved among species. A typical riboswitch has a high affinity for the ligand it binds, with the K_D often being under 10 nM, and decreases in affinity of two orders of magnitude even for closely related compounds.[27]

Certain properties are advantageous for a riboswitch to be a good antibacterial target. The riboswitch needs to be in a pathogenic bacteria and act as an off switch for expression of an essential gene or for multiple synthetically lethal genes.[27,29] In addition, the aptamer domain needs to have a high affinity for a drug-like ligand. Some riboswitches can be found in several different bacteria, which would allow one drug to target multiple bacteria at once. For this, the binding sites would need to be of similar size and polarity.[29] Other riboswitches are only found in specific bacteria, allowing for narrow spectrum antibiotics that would help prevent the spread of antibacterial resistance.

The work reported here focuses on the class I $preQ_1$ riboswitch from *Bacillus Subtilis*, one of the smallest known to date with only 37 nucleotides in its aptamer domain (Fig. 1.2A).[24,30] When the riboswitch binds its ligand, $preQ_1$ (Fig. 1.2B), the aptamer domain folds into an H-type pseudoknot, causing a terminator loop to form in the expression platform which causes gene expression to stop at the transcriptional stage.[24,31] The $preQ_1$ riboswitch is a good model system for studying the interplay between the structure and photophysics of 2-AP, and the structure of the RNA it resides within, due to a string of adenosine residues near the 3' end of the riboswitch ("L3"). This string of A's offers sites that are expected to impact ligand binding (due to

proximity to the ligand binding pocket) and are not expected to impact ligand binding (due to being farther away).

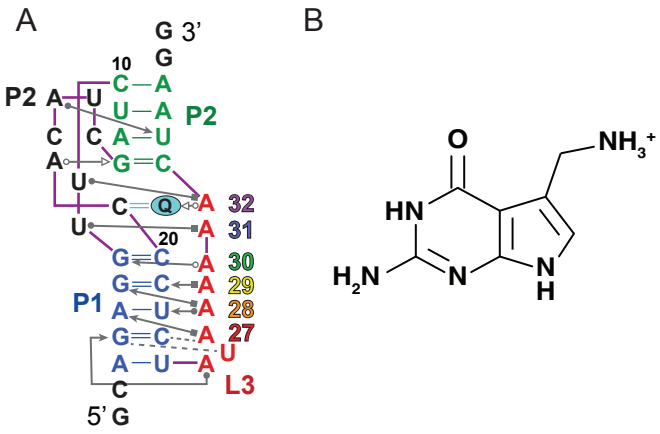

Figure 1.2 A. The structure and sequence of the preQ$_1$ riboswitch from Bacillus subtilis in Leontis-Westof notation. B. Chemical structure of the ligand preQ$_1$. Panel A adapted from ref. 29.

2-AP has been utilized extensively in the preQ$_1$ riboswitch from *Thermoanaerobacter tengcongensis*.[32] 2-AP was substituted into the riboswitch in different areas to probe different areas in the riboswitch, looking at the P1, P2, and L2 regions. Different nucleotides were found to rearrange upon ligand binding at different rates. Nucleotides that were investigated in the P2 and L2 regions had similar folding rates of around 40,000 $M^{-1}s^{-1}$, while the P1 region had a folding rate of around 11,000 $M^{-1}s^{-1}$. In contrast, there had been only minimal usage of 2-AP in the preQ$_1$ riboswitch from *Bacillus subtilis*.[33] Furthermore, the impacts of 2-AP substitution on the structure and function of RNA had not been studied in detail.

The work reported in this thesis provided insight into the ligand binding affects the local structure around adenosine residues in the preQ$_1$ riboswitch, and helps to clarify the perturbations 2-AP can exert when substituted into RNA. It also sheds light on the relationship between 2-AP photophysics and its local base stacking environment. These insights will allow 2-AP to be used productively in a wide range of complex RNA structures, and will allow measurements of its fluorescence to be analyzed more deeply.

CHAPTER II

METHODS

RNA structure is complex and important to its biological function. Due to this, methods to investigate the structure have been developed. Different experimental techniques reveal different information, from the global structure, to local structure, to changes in structures when a system is perturbed.

In the work presented in this thesis, various spectroscopic methods were used to study RNA labeled with 2-AP. Among these is circular dichroism (CD) spectroscopy, which measures the difference in absorbance is measured when a sample is excited with left- or right-handed circularly polarized light, as seen in Figure 2.1.[34–36] A polymer like RNA is made up of smaller subunits (nucleotides in the case of RNA) that combine to form a larger structure. The CD spectrum for a particular RNA strand has contributions from all the smaller subunits; in other words, CD reports on the global structure of the system.[35,37] CD is a useful technique for observing differences in global structure between different molecules or in the same molecule as it undergoes a structural change such as refolding or binding another molecule.[38] The native bases and FBAs contribute to the CD spectrum in different spectral regions. Native bases have absorption maxima around 260 nm and contribute to the CD signal below 300 nm, while FBAs typically have their lowest-energy transitions above 300 nm.[37,38] Due to this, changes in the CD spectrum in the 200-300 nm range indicate changes in the arrangement of the natives bases. Features in the CD spectrum above 300 nm can sometimes be attributed to the FBA and its immediate environment, but in larger systems, such features are obscured by the much larger overlapping signal from the native bases.[19,37,39,40] In addition, CD and overall sample absorbance

(typically measured at 260 nm) can be used to investigate the thermal stability of biological molecules. Upon heating, the CD and absorbance change due to the unfolding of the RNA.[35] As the RNA unfolds, the CD typically decreases due to an increase in conformational disorder, while the absorbance increases due to unstacking of the bases (termed "hyperchromicity"). Depending on the structure of the RNA or protein, different domains can unfold at different temperatures, leading to the observation of multiple transitions. Melting curves, in which CD and absorbance are measured as a function of temperature, can be fit to extract thermodynamic parameters for each transition. This can be particularly useful when studying RNA that has been chemically modified to determine how the modification impacts stability.[19,37]

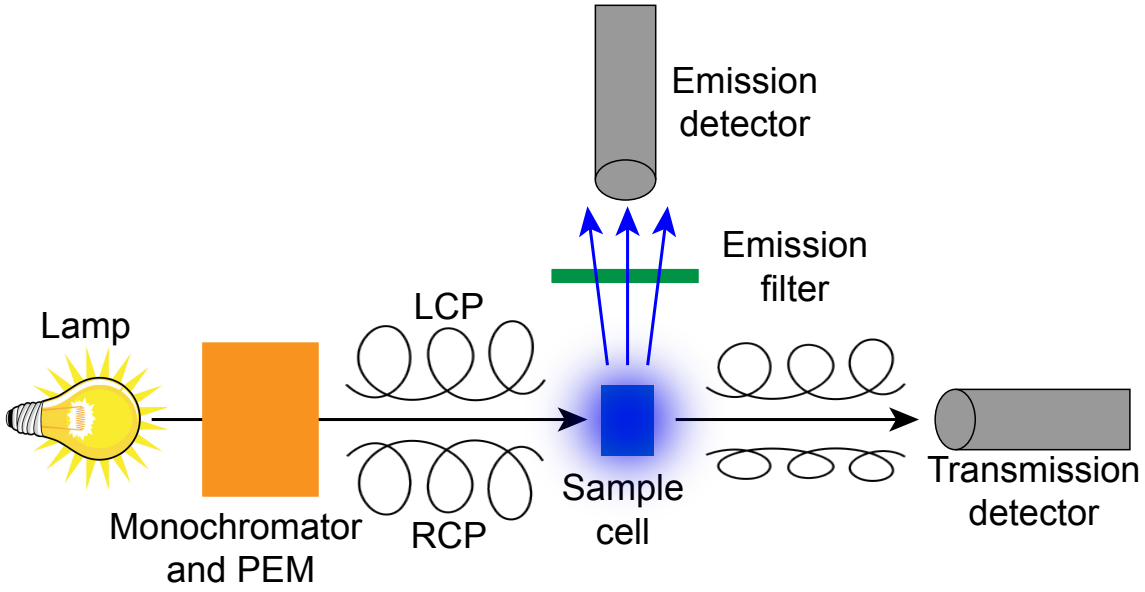

Figure 2.1. CD and FDCD experimental layout. A sample is excited with alternating left- and right-handed circularly polarized light (LCP; RCP). A CD measurements detects light transmitted by a sample (right), while an FDCD measurement detects emission following removal of scattered lamp light by a filter (top).

Fluorescence-detected circular dichroism (FDCD) is a spectroscopic technique that combines CD with fluorescence detection to study samples that are both chiral and fluorescent.[41] The FDCD signal is the difference in fluorescence intensity that results from the sample being

excited with left- and right-handed circularly polarized light (Figure 2.1). While the principles of FDCD are well established, it has not been used frequently in the roughly fifty years since it was first reported.[42,43] In some cases, FDCD can be measured with sample concentrations orders of magnitude lower than used for standard CD, though this depends on the fluorophore being used, so each case needs to be considered separately.[44–47] In addition, due to FDCD relying on fluorescence, the only chromophores that generate signal are those that are fluorescent, unlike in CD. This reveals information about the local structure around the fluorophore. For a nucleic acid labeled with an FBA, this may include whether it is in a stacked or unstacked conformation.[48] Through theory, FDCD data can be converted to a predicted CD spectrum of the fluorescent species in a sample using the following equation:

$$\frac{\Delta\varepsilon_F}{\varepsilon_F} = \left(\frac{\theta}{14323} + \frac{CD}{32980 * A} - \frac{ln10 * CD * 10^{-A}}{32980(1 - 10^{-A})}\right)$$

Here, $\Delta\varepsilon_F = \varepsilon_{F,L} - \varepsilon_{F,R}$ where $\varepsilon_{F,L}$ and $\varepsilon_{F,R}$ are the extinction coefficient of the fluorophore from excitation with left- and right-handed circularly polarized light, θ is the FDCD signal in units of millidegrees per volt, CD is the total CD signal in millidegrees, and A is the total absorbance.

If the system exists with multiple different conformations with different fluorescence quantum yields, theory can also be used to determine the populations of each conformation.[43] If the converted FDCD spectrum and measured standard CD spectrum agree with each other, then the signal in FDCD comes from all species in proportion to how prevalent they are in the sample. A simple example is when only one optically active species is present, as seen for 2-AP riboside (Figure 2.2 A). If the converted FDCD and CD disagree with each other, then multiple species exist with different fluorescence quantum yields (Figure 2.2 B). Each species contributes to the standard CD in proportion to how prevalent it is, and to the FDCD in proportion to how prevalent it is and its fluorescence quantum yield.

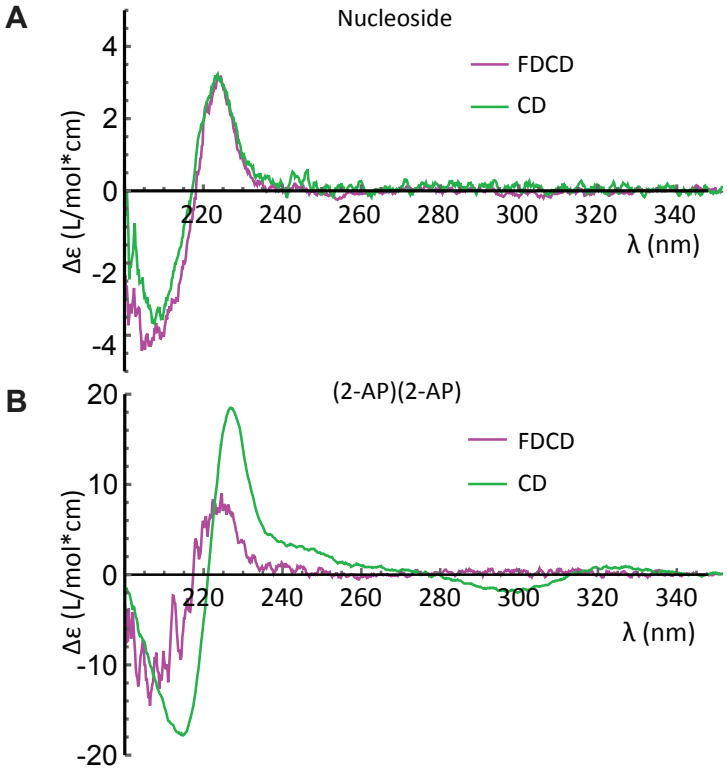

Figure 2.2 CD and converted FDCD for (A) 2-AP nucleoside and (B) 2-AP dinucleotide, adapted from Ref. 19.

A potential problem that can arise with FDCD is that the fluorescence can be polarized if the fluorophore cannot freely rotate on a faster timescale than emission.[49,50] In this situation, the observed FDCD signal depends on the angle between the excitation light and the axis of the detector. Early investigation into this identified a workaround using a cylindrical sample cell and two perpendicular photomultiplier tubes, but this requires having more specialized instrumentation than a standard commercial CD spectrometer.[51] More recently, Nehira et al have developed a cell holder that places the sample cell at a focus of an ellipsoidal mirror, collecting the fluorescence emitted by the sample in all directions. Utilizing this device removed the polarization artifacts seen previously while improving the signal collection efficiency.[49]

In addition to CD and FDCD, the excited state lifetime of the fluorophore can be used to study the structure of RNA. The most common method of collecting information about the

lifetime of the fluorophore is time-correlated single-photon counting (TCSPC).[52] In a TCSPC measurement, the system is excited with a pulsed light source and the time between excitation and the emission of a photon is measured by the instrument. This is done repeatedly to populate a histogram of photon arrival times (Figure 2.3).

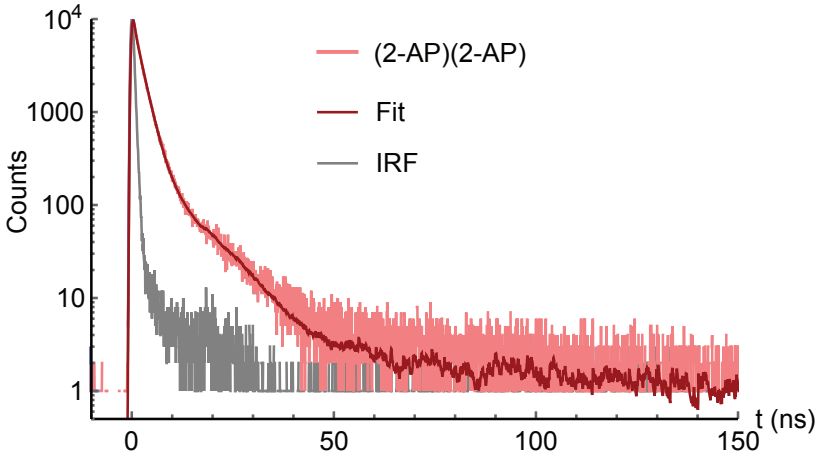

Figure 2.3 TCSPC histogram recorded on a dinucleotide of 2-AP and 2-AP, (2-AP)(2-AP), and associated IRF and fit.

The precision of a TCSPC system is determined by its Instrument Response Function (IRF). In an ideal system, the IRF is infinitely narrow due to an infinitely sharp excitation pulse and infinitely accurate detectors and electronics. In practice, finite duration of the excitation pulse, timing uncertainty of the detector and timing jitters in the electronics lead to a broadening of the IRF. In some cases, the excited state lifetime of the system can be shorter than the duration of the IRF. In some cases, the lifetime can still be extracted through a reconvolution fit that accounts for impact of the finite width of the IRF on the observed fluorescence decay. The photon arrival time histogram is fitted, typically with a single- or multi-exponential decay, and the lifetime of the fluorophore is defined to be the time constant of a given exponential component. The equation for fitting is:

$$I(t) = a_1 e^{\frac{-t}{\tau}} + a_2 e^{\frac{-t}{\tau}} + \cdots$$

Where a_i is the weight and τ_i is the lifetime of component i. Multi-exponential decays are typically interpreted to result from conformational heterogeneity, with the weights representing the prevalence of different conformations, and conformations in which the fluorophore is less quenched exhibiting longer lifetimes. If multiple components are observed, as seen in Figure 2.3, it can be useful to visualize their weights using a pie chart (Figure 2.4). Here, the area of each section of the chart shows the population that exists in the conformation that contributes the lifetime indicated inside or adjacent to the section. If there is a change in the system (e.g. due to a change in solvent polarity or cations present), it can be reflected in a change in weight of each component, allowing a way to visualize shifts in population between different structures.

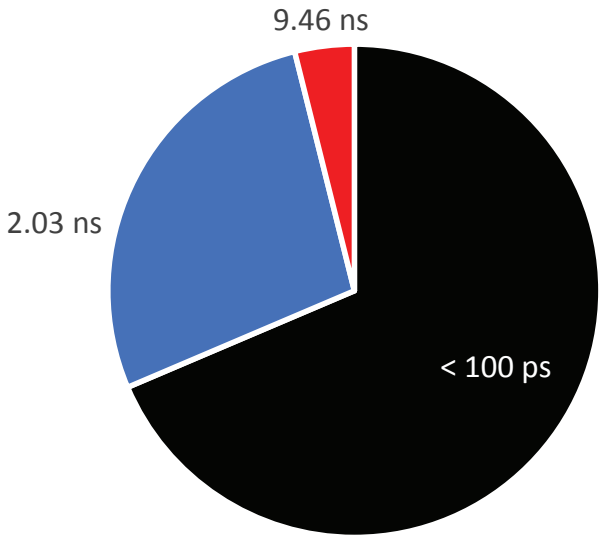

Figure 2.4 Pie chart of 2-AP dinucleotide lifetimes from Figure 2.3 adapted from Ref. 19.

In the case of 2-AP, the fluorescence lifetime has been shown to depend on environmental factors like solvent, base stacking, and temperature.[7,53] The lifetime of a fluorophore will also change if there is a structural change, like with riboswitch refolding due to ligand binding. Short lifetimes caused by quenching are seen in rigid, stacked conformations[54] or nonpolar solvents.[55] The lifetime of free 2-AP in solution is ~10 ns.[56,57] When placed into larger molecules like DNA, it is possible for it to have multiple lifetimes, which is indicative of

multiple conformations.[24,56,57] Longer lifetimes, close to that of free 2-AP, are possible, and are likely due to solvent exposed extra-helical conformations of 2-AP.[56,57] It is also possible for a sample to have a dark population, where the lifetime is faster than what the instrument can measure.[58] In 2-AP-modified nucleic acids, dark populations occupy very stacked structures that undergo rapid nonradiative relaxation. The dark population suppresses the steady state fluorescence intensity without impacting the observed TCSPC data. Thus, the presence of a dark population can be ascertained by taking the ratio of the lifetime observed for a sample of interest to that of a reference sample assumed to have no dark population, and comparing it to the ratio of the steady-state emission intensities of the two samples. For example, the weight of the dark (<100 ps) population shown in Fig. 2.4 was determined using 2-AP nucleoside as the reference.

As demonstrated in the following chapters, CD, FDCD, and fluorescence lifetimes can all be used to study different aspects of RNA structure. Each technique reveals different information that reflects how the RNA folds, both globally and locally.

CHAPTER III

BASE-STACKING HETEROGENEITY IN RNA RESOLVED BY FLUORESCENCE-DETECTED CIRCULAR DICHROISM SPECTROSCOPY

The contents of this chapter have been previously published in whole or in part. The text present here has been modified from the publication below:

Widom, J. R.; Hoeher, J. E. Base-Stacking Heterogeneity in RNA Resolved by Fluorescence-Detected Circular Dichroism Spectroscopy. *J. Phys. Chem. Lett.* **2022**, *13* (34), 8010–8018. https://doi.org/10.1021/acs.jpclett.2c01778.

MAIN TEXT

The functions of biological macromolecules are intimately linked to their structures. Ribonucleic acid (RNA) can fold into a wide variety of 3-dimensional structures that endow it with unique catalytic and regulatory properties. RNA structure is determined by several different types of interactions.[1] Cations such as Na^+ and Mg^{2+} enable RNA to adopt compact conformations by neutralizing the negatively charged sugar-phosphate backbone and, in some cases, binding at specific sites.[2,3] Hydrogen bonding between nucleobases gives rise to the phenomenon of Watson-Crick base pairing, in which adenine (A) residues base-pair with uracil (U), and guanine (G) base-pairs with cytosine (C). Many types of non-Watson-Crick base pairs also occur in RNA.[4] In addition, Van der Waals interactions between the aromatic nucleobases help to stabilize structures in which the bases stack on top of one another.[5] Base stacking contributes significantly to the stability of both RNA and DNA structures,[6] and stacking between nucleobases and aromatic amino acids plays a role in RNA binding by certain proteins.[7,8] Bases fluctuate between stacked and unstacked conformations on a microsecond timescale,[9,10] and these transient structures may provide targets that are kinetically trapped by ligand or protein

binding.[11-13] Base stacking heterogeneity therefore plays a crucial role in nucleic acid structure and function.

A powerful approach to monitoring base stacking is the use of fluorescent base analogues (FBAs). These are variants of the natural bases that are chemically modified in order to render them fluorescent, with the goal of exerting minimal perturbations on the nucleic acid they are used to study. Many FBAs have been developed,[14-20] but the adenine analogue 2-aminopurine (2-AP) is by far the most widely utilized.[21] When free in solution, 2-AP riboside (Figure 3.1A; R=ribose) exhibits redshifted absorption relative to the natural bases and strong fluorescence with a quantum yield of ~0.68 and a lifetime of ~10 ns (Figure 3.1B-C).[21-23] Upon incorporation into nucleic acids, it is quenched up to 100-fold in a sequence- and structure-dependent manner.[21,24,25] This change can be ascribed to alterations in the relative energies of bright π-π^* and dark n-π^* transitions that result from stacking interactions and charge transfer with neighboring bases.[26,27] Incorporation into RNA and DNA also leads to complex decays in time-resolved fluorescence experiments that can be fit with multiple exponential decay components,[28] continuous lifetime distributions,[29] or a combination thereof,[30] indicating the presence of base stacking heterogeneity.

In this work, we use standard (transmission-detected) and fluorescence-detected circular dichroism spectroscopy (CD and FDCD, respectively) and time-correlated single photon counting (TCSPC) to probe base stacking in 2-AP-labeled RNA oligonucleotides. In dinucleotides containing 2-AP, we detect fluorescence only from unstacked conformations with spectra that are nearly identical to isolated 2-AP riboside. In contrast, fluorescence *is* observed

from stacked conformations in a trinucleotide, enabling us to determine the populations and relative fluorescence quantum yields of stacked and unstacked conformational states using a parameter-free model. This work provides a unique window into the distribution of conformations that are present in solution, as well as the effects of oligonucleotide structure on 2-AP photophysics.

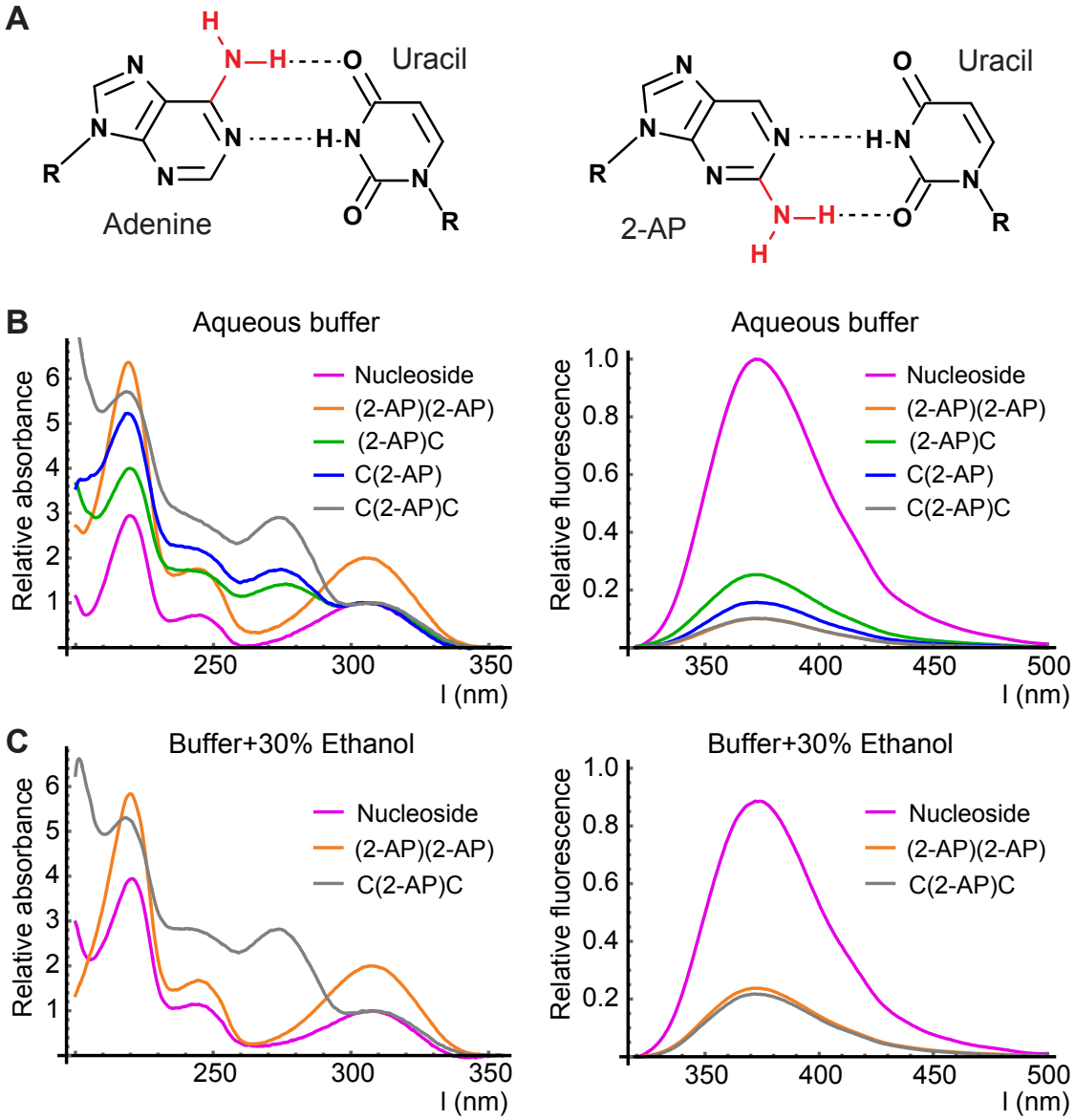

Figure 3.1. (A) Watson-Crick base pairs between adenine and uracil (left), and 2-AP and uracil (right). Chemical modification is indicated in red. (B-C) Absorbance (left) and fluorescence emission (right) spectra of the samples used in this study in aqueous phosphate buffer (B) or phosphate buffer containing 30% ethanol (C). Absorbance

spectra have been scaled so that the longest-wavelength absorbance peak has a value of 2 for 2-AP dinucleotide (orange) and 1 for all other samples. Fluorescence spectra report the intensity per 2-AP residue and have been scaled such that free 2-AP riboside in aqueous buffer has a peak intensity of 1.

We first recorded fluorescence, CD and FDCD spectra of 2-AP riboside and dinucleotide. 2-AP dinucleotide exhibited 9.7-fold fluorescence quenching relative to 2-AP riboside (Figures 3.1B and A1), and significant dark ($\tau < 200$ ps) and partially quenched ($\tau = 2$ ns) populations were observed through TCSPC (Table 3.1 and Figure A2). As previously observed for 2-AP (deoxyribo)dinucleotide,[31] 2-AP (ribo)dinucleotide exhibited a sigmoidal CD spectrum arising from coupling between strong π-π^* transitions on each base,[22,32] with features centered around its electronic transition bands at 220 and 310 nm (Fig. 3.2C). In contrast, 2-AP riboside exhibited a weak CD signal that was nonzero only at wavelengths <240 nm, arising from coupling between high-energy electronic transitions on the ribose sugar and the base (Figure 3.2B).[32] Surprisingly, the FDCD spectra of both samples exhibited extremely similar lineshapes (Figure A3). This led us to hypothesize that fluorescence from 2-AP dinucleotide was produced almost entirely by emitting species that are unstacked (Figure 3.2A). The CD spectra of these conformations would contain only contributions similar to those observed in the nucleoside.

Sample	Solvent	$\langle\tau\rangle_{obs}$	α_0 (%)	α_{1c}	τ_1 (ns)	α_{2c}	τ_2	α_{3c}	τ_3
2-AP riboside	B	9.17	0			2.9	2.58	97.1	9.37
2-AP riboside	B+E	8.40	0			10.9	1.25	89.1	9.28
(2-AP)(2-AP)	B	2.95	68.6			27.5	2.03	3.9	9.46
(2-AP)(2-AP)	B+E	4.16	42.3			47.7	3.55	10.0	7.05
(2-AP)C	B	5.02	54.3	4.0	0.29	28.7	3.65	13.0	9.49
C(2-AP)	B	2.51	42.0	11.5	0.23	41.3	2.43	5.2	8.35
C(2-AP)C	B	4.11	77.0			15.2	2.59	7.8	7.11
C(2-AP)C	B+E	5.14	55.8			15.1	2.77	29.1	6.36

Table 3.1. Observed average lifetime ($\langle\tau\rangle_{obs}$) and populations (α_{ic}) and lifetimes (τ_i) of individual decay components obtained through TCSPC. α_0 is a dark population whose decays are not resolved ($\tau < 200$ ps). The populations α_{ic}

have been corrected to account for the presence of the dark population (see methods for details). "B": Aqueous buffer. "B+E": Buffer containing 30% ethanol.

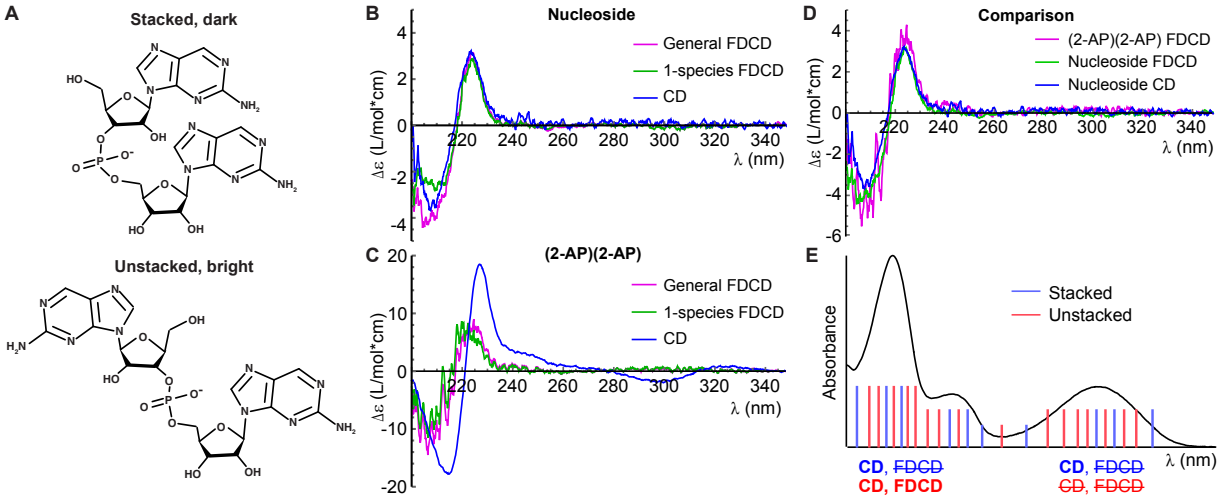

Figure 3.2. (A) Schematic of 2-AP dinucleotide in a stacked conformation (top) in which it is highly quenched, and a brighter unstacked conformation (bottom). (B) Spectra of 2-AP riboside. (C) Spectra of 2-AP dinucleotide. Magenta: FDCD spectra processed with eq 1; Green: FDCD spectra processed with eq 2; Blue: standard CD spectra. (D) Magenta: FDCD spectrum of 2-AP dinucleotide processed using eq 1 under the assumption that all observed fluorescence comes from unstacked "nucleoside-like" structures. This spectrum shows strong agreement with the nucleoside FDCD (green) and CD (blue) spectra. (E) Illustration of how CD and FDCD report on different conformational subpopulations. The inhomogeneously broadened absorbance spectrum of 2-AP dinucleotide contains contributions (sticks) from stacked (blue) and unstacked (red) conformations. Labels below absorption bands indicate whether the stacked and/or unstacked conformations contribute to that band's FDCD and/or CD signal. Nonzero CD is observed when 2-AP has optical activity, while nonzero FDCD is observed when 2-AP is fluorescent AND optically active.

To test this hypothesis quantitatively, we used established theory[33] to convert our FDCD spectra into predicted CD spectra of the fluorescent species in the sample: $\Delta\varepsilon_F = \varepsilon_{F,L} - \varepsilon_{F,R}$, where $\varepsilon_{F,L(R)}$ is the extinction coefficient of the *fluorophore only* under excitation with left (right)-handed circularly polarized light. These predictions will henceforth be called "processed" FDCD spectra. $\Delta\varepsilon_F$ can be predicted using eq 1, termed the "general FDCD equation", where ε_F is the polarization-independent extinction coefficient of the *fluorophore only*, θ is the FDCD signal in units of millidegrees, CD is the total CD signal (including both fluorescent and nonfluorescent species) in units of millidegrees, and A is the total absorbance:

$$\frac{\Delta\varepsilon_F}{\varepsilon_F} = \left(\frac{\theta}{14323} + \frac{CD}{32980 \cdot A} - \frac{\ln 10 \cdot CD \cdot 10^{-A}}{32980\left(1 - 10^{-A}\right)} \right) \quad (1)$$

The right-hand side of eq 2 will henceforth be abbreviated as "$FDCD_{adj}$", as it contains the raw FDCD signal θ adjusted to account for the overall absorbance and CD of the sample. If there are no species present that absorb but are nonfluorescent, then $\Delta\varepsilon_F/\varepsilon_F = \Delta A/A$. Given that $CD = \Delta\varepsilon_F \cdot 32980 \cdot c \cdot l$, where c is the concentration of the fluorophore and l is the pathlength, eq 1 can be modified to eq 2, termed the "1-species FDCD equation":

$$\Delta\varepsilon_F = \frac{\theta \cdot \left(1 - 10^{-A}\right)}{32980 \cdot c \cdot l \cdot 10^{-A}} \quad (2)$$

The measured CD spectrum of 2-AP riboside agrees closely with the processed FDCD spectrum, with both the lineshape and the intensity being accurately predicted (Figure 3.2B). In contrast, the CD and processed FDCD spectra bear little resemblance for 2-AP dinucleotide (Figure 3.2C), indicating the presence of multiple structures that interconvert on a timescale slower than the fluorescence lifetime. If, as hypothesized above, the "fluorophore" in the dinucleotide sample is a "nucleoside-like" unstacked species (Figure 3.2A), then eq 2 must be altered such that ε_F is that of the nucleoside rather than the dinucleotide. When this adjustment is made, the processed FDCD spectra of both samples agree closely with each other and with the nucleoside's measured CD spectrum (Figure 3.2D), indicating that the fluorescent species in the dinucleotide sample has the same CD spectrum as the nucleoside. A similar conclusion was previously drawn in an FDCD study of dinucleotides containing the fluorophore 1,N^6-ethenoadenosine.[34] We confirmed the chemical purity of our samples using thin layer

chromatography, demonstrating that the fluorescence arises from an unstacked conformational subpopulation rather than monomers generated by chemical degradation of 2-AP dinucleotide (Figure A4).

We next investigated a series of dinucleotides and trinucleotides in which 2-AP was placed adjacent to cytosine residues. Cytosine was chosen to avoid the complicating factors of energy transfer from adjacent bases to 2-AP, which is most efficient for adenine,[35] and quenching of 2-AP fluorescence due to charge transfer to neighboring bases, which is most efficient for guanine.[36,37] The dinucleotide (2-AP)C exhibited 4.0-fold fluorescence quenching relative to free 2-AP riboside and a strong CD signal across the UV, including at wavelengths >300 nm where only 2-AP absorbs directly (Figure 3.3A). C(2-AP) exhibited 6.3-fold quenching and minimal CD signal >300 nm (Figure 3.3B). For both dinucleotides, FDCD spectra processed using eq 1 predicted that the CD spectra of the fluorescent species in the sample were nearly identical to that of the free nucleoside (Figure 3.3D). In 2-AP dinucleotide, (2-AP)C and C(2-AP), TCSPC measurements identified populations with lifetimes of 2-4 ns and 8-10 ns, as well as a significant (40-70%) dark population with lifetime <200 ps (Table 3.1). The FDCD spectra suggest that even the partially quenched (τ = 2-4 ns) population is sufficiently unstacked to have a CD spectrum that lacks contributions from base-base coupling. We conclude that in all three dinucleotides, fluorescence comes almost exclusively from an ensemble of nucleoside-like unstacked conformations that includes both unquenched and partially quenched subpopulations.

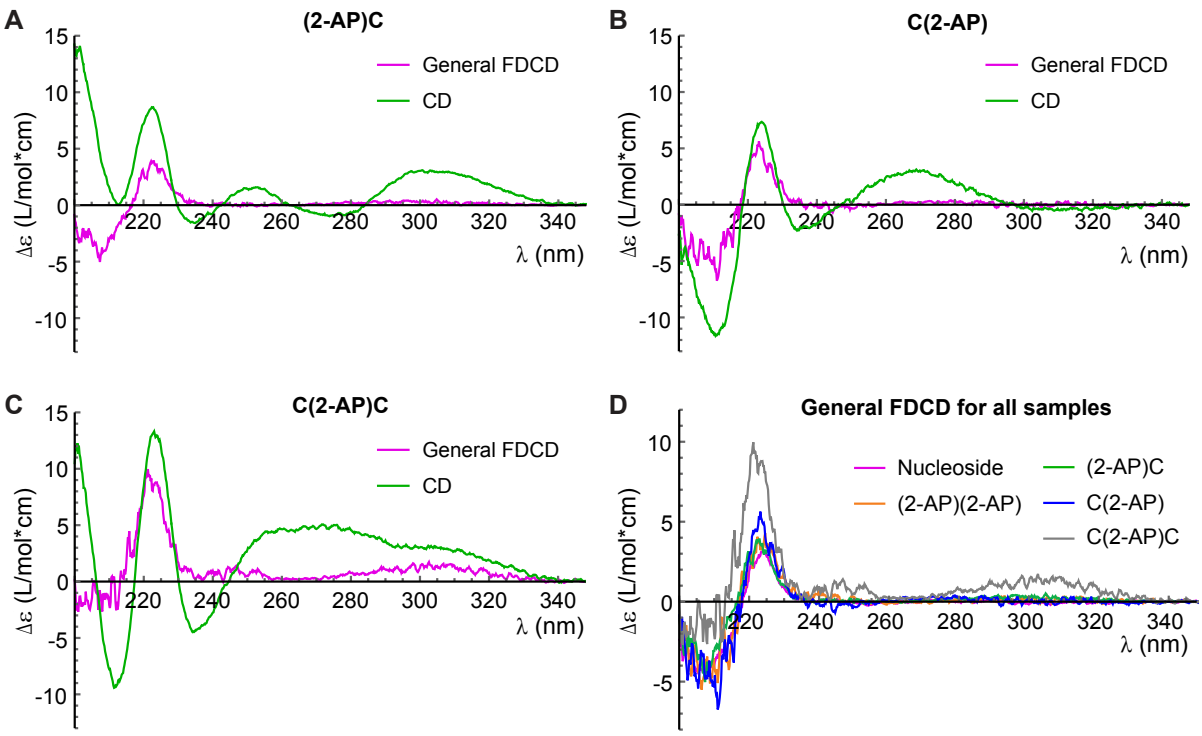

Figure 3.3. FDCD and CD spectra of (2-AP)C (A), C(2-AP) (B) and C(2-AP)C (C). Magenta: FDCD spectra processed with eq 1; Green: standard CD spectra. (D) Overlay of FDCD spectra for all aqueous samples, processed with eq 1.

In the trinucleotide C(2-AP)C, fluorescence was quenched to a greater degree (9.7-fold relative to 2-AP riboside), indicating a shift in the conformational ensemble toward stacked structures. In addition, nonzero FDCD signal was observed in the lowest-energy absorption band of 2-AP around 310 nm, indicating that some fluorescence was originating from conformations with optical activity at that wavelength (Figure 3.3C). However, the FDCD spectrum predicts a CD intensity that is smaller than what is observed experimentally. To determine the implications of the discrepancy between the trinucleotide's CD and FDCD spectra, we assumed that it exists in equilibrium between an ensemble of unstacked conformations with the same fluorescence quantum yield and CD spectrum as 2-AP riboside, and an ensemble of stacked conformations (Figure 3.4A). In aqueous buffer, we observed 9.7-fold fluorescence quenching in the trinucleotide compared to the nucleoside, allowing us to write:

$$\phi_{nuc} c_{nuc} = 9.7\left(\phi_{un} c_{un} + \phi_{st} c_{st} \right)$$

where c_{nuc}, c_{un} and c_{st} are the concentrations of the nucleoside, stacked population, and unstacked population, respectively, and ϕ_{nuc}, ϕ_{un} , and ϕ_{st} are their fluorescence quantum yields. Assuming that the quantum yield of the unstacked population is equal to that of the nucleoside, and accounting for the fact that the sum of the concentrations of stacked and unstacked populations is equal to the total sample concentration, we obtain eq 3:

$$R_{\phi} \cdot c_{tot} = 9.7\left[R_{\phi}\left(c_{tot} - c_{st} \right) + c_{st} \right] \tag{3}$$

where c_{tot} is the total sample concentration and $R_{\phi} = \phi_{nuc}/\phi_{st}$ is the ratio of the quantum yields of the nucleoside and stacked conformation.

At wavelengths longer than ~300 nm, native base absorption is negligible and $\Delta\varepsilon_L/\varepsilon_F = \Delta A/A$ could potentially apply. Indeed, the 1-species and general equations agree with each other at these wavelengths, indicating that the signals are not impacted by direct absorbance by the C residues. 2-AP riboside exhibits no CD signal at these wavelengths (Figure 3.2B), so the CD of the trinucleotide comes entirely from the stacked population (eq 4). This step sorts the continuum of structures potentially adopted by an oligonucleotide into an ensemble of unstacked conformations with zero CD signal at the wavelengths being considered, and an ensemble of stacked conformations that contribute the entire CD signal.

$$c_{st} \cdot \Delta\varepsilon_{st}(\lambda) = \frac{CD(\lambda)\ (\text{mdeg})}{32980} \tag{4}$$

The FDCD spectra of samples containing multiple fluorescence species can be processed using eq 5, where i counts over all fluorescent species, whose contributions are weighted by their quantum yields ϕ_i and concentrations c_i:

$$\frac{\sum_i \phi_i c_i \Delta\varepsilon_i(\lambda)}{\sum_i \phi_i c_i \varepsilon_i(\lambda)} = FDCD_{adj} \tag{5}$$

Plugging in the properties of the stacked and unstacked populations into eq 5 yields eq 6:

$$\frac{\phi_{nuc}\left(c_{tot} - c_{st}\right)\Delta\varepsilon_{nuc}(\lambda) + \phi_{st} c_{st} \Delta\varepsilon_{st}(\lambda)}{\phi_{nuc}\left(c_{tot} - c_{st}\right)\varepsilon_{nuc}(\lambda) + \phi_{st} c_{st} \varepsilon_{st}(\lambda)} = FDCD_{adj}(\lambda) \tag{6}$$

Noting that $\Delta\varepsilon_{nuc}$=0 at the wavelengths being considered and plugging in eq 4 for $c_{st}\Delta\varepsilon_{st}(\lambda)$, we obtain eq 7:

$$\frac{CD(\lambda)/32980}{\varepsilon_{nuc}(\lambda) R_{\phi}\left(c_{tot} - c_{st}\right) + \varepsilon_{st}(\lambda) c_{st}} = FDCD_{adj}(\lambda) \tag{7}$$

One obtains estimates of R_ϕ and c_{st} by solving the system of eqs 3 and 7 at each wavelength based on the experimental measurements of *CD*, *A*, θ and ε (Figure 3.4 and Table 3.2), with no free parameters required. We investigated a model in which the extinction coefficient of the nucleoside was used for both the stacked and unstacked populations ($\varepsilon_{nuc} = \varepsilon_{un} = \varepsilon_{st}$), and one in which they have different extinction coefficients (Figures A5-A6). For the latter, the difference in extinction coefficient between the two states was estimated by measuring absorbance of 2-AP riboside and C(2-AP)C as a function of temperature, which yielded $\varepsilon_{st} = 0.86*\varepsilon_{nuc} = 0.86*\varepsilon_{un}$ (Figure A7; see methods for details). For C(2-AP)C, the resulting values of R_ϕ and c_{st} are stable across the range of wavelengths in which the stated assumptions hold and the sample exhibits appreciable signal (300-320 nm), and are largely independent of whether data smoothing is used

and whether one or two extinction coefficients are used (Table 3.2). For example, with data smoothed using a 5 nm rolling average and ε_{st}=0.86*ε_{un}, we obtain R_ϕ = 23 ± 1 and an unstacked population of 6.3 ± 0.2 % of the total (mean ± standard deviation across all data points from 300 to 320 nm). This indicates that the stacked conformation is quenched to a greater extent than one might assume based on the overall 9.7-fold fluorescence intensity ratio (free nucleoside:trinucleotide), and that a minor unstacked population of only 6.3% of the total gives rise to 61% of the fluorescence emitted by the sample.

	Buffer				30% Ethanol		
Smoothing	ε	R_ϕ	% un.	% fl. un.	R_ϕ	% un.	% fl. un.
None	1	22 ± 4	5.9 ± 0.7	58	6 ± 1	11 ± 4	42
5 nm	1	22 ± 1	6.0 ± 0.3	59	5.7 ± 0.5	11 ± 2	42
None	2	23 ± 4	6.2 ± 0.6	61	6 ± 1	12 ± 3	48
5 nm	2	23 ± 1	6.3 ± 0.2	61	6.2 ± 0.5	12 ± 1	47

Table 3.2. Quenching ratios and unstacked populations for C(2-AP)C. Results are shown for models with and without smoothing by a 5 nm rolling average, and with (ε=2) and without (ε=1) accounting for hypochromicity of 2-AP in the stacked conformation. R_ϕ = quenching ratio (ϕ_{un} / ϕ_{st}); % un. = percent unstacked; % fl. un. = % of total fluorescence that comes from the unstacked population. Mean ± standard deviation of the results obtained at all datapoints in the range of 300 to 320 nm.

We repeated these measurements on 2-AP dinucleotide and C(2-AP)C in phosphate buffer containing 30% v/v ethanol (mole fraction ~0.1), which is thought to shift population away from stacked conformations.[31] Addition of ethanol at this concentration increases the viscosity of pure H_2O from $0.89 \cdot 10^3$ Pa·s to approximately $2 \cdot 10^3$,[38] and decreases its dielectric constant from 78.41 to approximately 66.[39] It has previously been shown that a decrease in dielectric constant of this magnitude impacts the morphology of double-stranded DNA condensates[40] and promotes folding of certain RNA species,[41] potentially by enhancing counterion condensation around the phosphate backbone. This is not expected to be a dominant

factor for our short single-stranded oligonucleotides, which have only 1-2 phosphate groups per molecule.

As expected from the known effects of ethanol on base stacking, the oligonucleotides were quenched to a lesser degree in 30% ethanol (3.5-fold for 2-AP dinucleotide and 3.7-fold for C(2-AP)C relative to 2-AP riboside in the same solvent; Figures 3.1C and A1). In TCSPC measurements, the slowest decay component shortened and increased in amplitude, while the dark population decreased (Table 3.1). The CD spectrum of 2-AP dinucleotide decreased in intensity and its lineshape changed at long wavelengths, whereas the FDCD spectrum remained nearly unchanged (Figure A8). With fluorescence coming almost exclusively from unstacked conformations even in aqueous buffer, it was unsurprising that the same observation held when ethanol was used to shift the stacking equilibrium. The CD spectrum of C(2-AP)C showed more complex changes when ethanol was added (Figures 3.4 and A8). Our model suggested that the quenching ratio R_ϕ decreases significantly to only 6, while the unstacked population doubles to 12% of the total, resulting in 53% of fluorescence being emitted by the unstacked population (Table 3.2). The increase in unstacked population was expected, but the large decrease in the quenching ratio suggests that ethanol alters the structure of the stacked population, mitigating its quenching. An alteration of the stacked structure is consistent with the complex changes in the CD spectrum that are observed upon addition of ethanol to C(2-AP)C.

2-AP-labeled dinucleotides and trinucleotides have previously been investigated by CD and time-resolved fluorescence measurements,[24,30,31,42,43] although the DNA versions of these small model systems have been far more studied than their RNA counterparts. Two decay components (8.1 and 1.1 ns) were resolved using frequency-domain fluorescence lifetime measurements for 2-AP deoxyribodinucleotide [d(2-AP)d(2-AP)]. The slower (8.1 ns) and

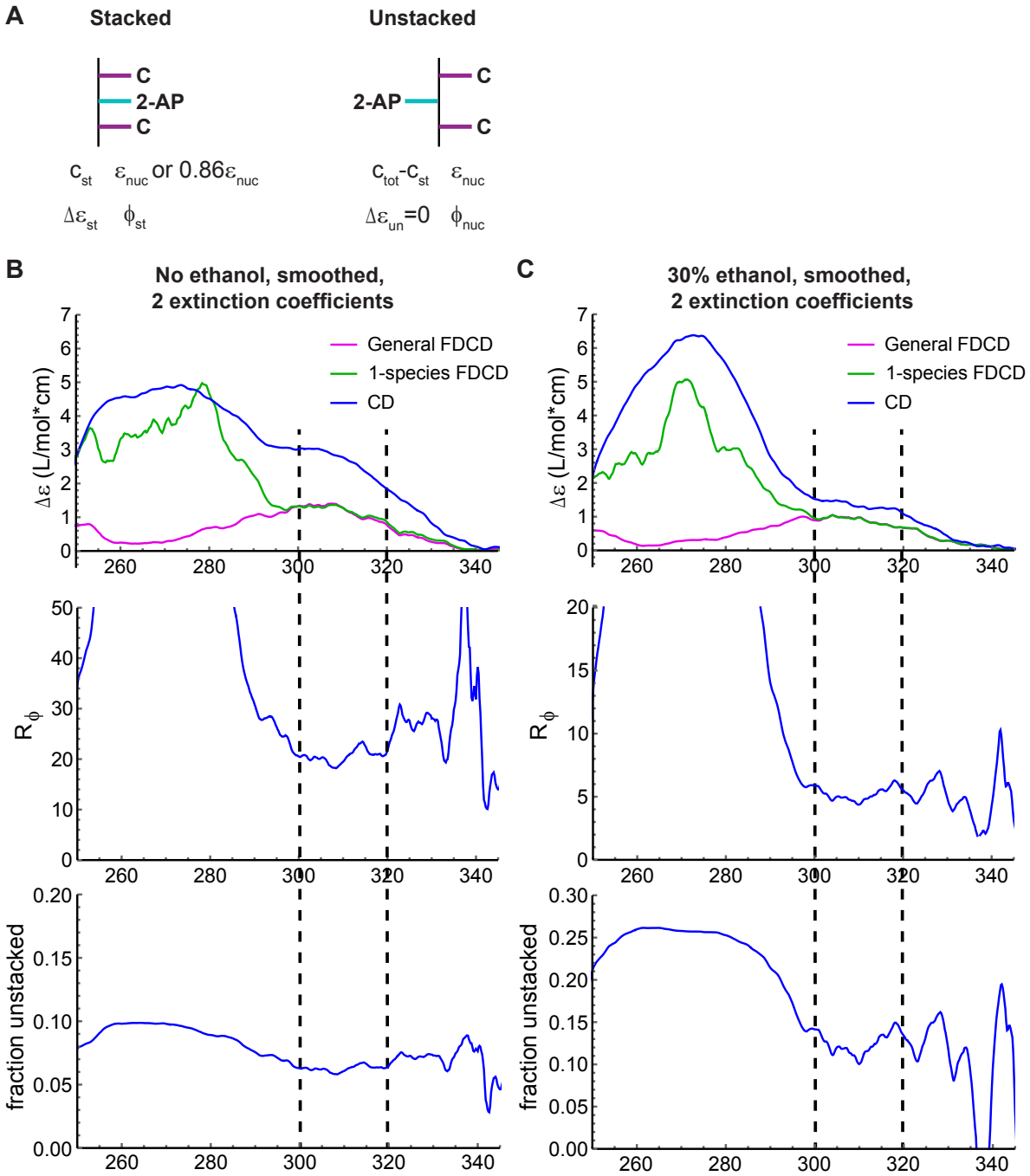

Figure 3.4. Fluorescence quenching and stacking heterogeneity in C(2-AP)C. (A) Model used for data analysis. In the unstacked ("un") conformation, 2-AP has properties characteristic of the free nucleoside "nuc", while the stacked conformation ("st") has a different CD signal and fluorescence quantum yield. c=concentration, ε=extinction coefficient, $\Delta\varepsilon=\varepsilon_L-\varepsilon_R$, ϕ=quantum yield. (B) Results of the "smoothed, 2 extinction coefficient" model for C(2-AP)C in aqueous buffer. Top: Closeup of the long-wavelength region of Fig. 3C. Magenta: FDCD spectra processed with eq 1; Green: FDCD spectra processed with eq 2; Blue: standard CD spectra. Middle: Value of the quenching ratio R_ϕ obtained at each wavelength by solving the system of eqs 3 and 7. Bottom: Value of the fraction unstacked $f_{un} = (c_{tot}-c_{st})/c_{tot}$ obtained at each wavelength. Dashed lines indicate the wavelength range over which parameter values were quantified. (C) Analogous plots for C(2-AP)C in buffer containing 30% v/v ethanol.

predominant (~64%) component approached the 9.0 ns lifetime of free 2-AP determined in that study.[31] We similarly observed decays of 9.5 and 2.0 ns in 2-AP ribodinucleotide, but the shorter (2.0 ns) one was predominant, a pattern that was recapitulated in (2-AP)C and C(2-AP). Similar behavior was previously observed in d(2-AP)dC[43] and dCd(2-AP),[24] each of which exhibits a minor population (~2% at 20 °C) with a lifetime of about 8 ns, a larger population (~36%) with a lifetime of about 2.5 ns, and two sub-nanosecond decay components. These results show that the members of this family of deoxyribo- and ribodinucleotides have minor unquenched conformational states that persist for at least the fluorescence lifetime, in addition to larger partially quenched populations. Significantly, our FDCD results demonstrate that these partially quenched populations are still highly unstacked, with CD spectra that are nearly identical to free 2-AP riboside. Consequently, the ensemble of conformations that gives rise to the CD signal at wavelengths >240 nm has minimal overlap with the ensemble that gives rise to fluorescence.

Three exponential decay components were observed in 2-AP-labeled DNA trinucleotides dXd(2-AP)dX, but the slowest was only ~3.5 ns at 20 °C, significantly shorter than the lifetime of free 2-AP. It was concluded that 2-AP persists in a fully unstacked conformation for less than 10 ns, with fluctuations back to stacked conformations "gating" decay to the ground state.[42] Slower stacking dynamics on the timescale of microseconds have been observed through single-molecule FRET[9] and temperature-jump infrared spectroscopy.[10] Gating appears to be less significant in C(2-AP)C, which exhibits a slowest decay component of 7.1 ns in aqueous buffer. The lifetime of this component decreases to 6.4 ns in 30% ethanol despite an increase in viscosity that would be expected to slow the stacking/unstacking kinetics, suggesting that gating is not responsible for the reduction in lifetime. Furthermore, because FDCD is a fluorescence-detected **excitation** spectroscopy, the spectral intensity and lineshape reflect species that are

present on the timescale of absorption rather than emission (fs rather than ps-ns). Dynamics occurring on timescales faster than the fluorescence lifetime would alter the apparent quantum yields of different conformations but would not alter their excitation spectra. Our results suggest that there is a population present in 2-AP-labeled RNA dinucleotides and trinucleotides that is sufficiently unstacked to lack CD contributions from coupling between 2-AP and the adjacent bases.

The 2-state model presented here sorts intermediate structures into stacked or unstacked ensembles based on whether they contribute to the CD spectrum. In the dinucleotides studied here, the "zero CD" ensemble includes both unquenched and partially quenched subpopulations identified through TCSPC. In contrast, in C(2-AP)C, the prevalence of the least quenched subpopulation alone is comparable to (in buffer) or larger than (in 30% EtOH) the entire "zero CD" population (Tables 3.1 and 3.2). Free energies determined through NMR[44,45] and temperature-dependent UV spectroscopy[46] show that stacking is slightly disfavorable in rArC and rCrA, while molecular dynamics simulations predict it to be slightly favorable.[47] Assuming that 2-AP exhibits similar stacking thermodynamics to A, this is consistent with the assertion above that the ensemble of unstacked conformations encompasses more structures and is more populated than the minor unquenched conformation observed in lifetime measurements. For C(2-AP)C, the free energy change resulting from a transition from the stacked to the unstacked structure depicted in Fig. 3.4A can be very roughly estimated by adding together the enthalpies of unstacking of rArC and rCrA, and averaging their entropies of unstacking and multiplying by 1.5 (because complete trinucleotide unstacking liberates three bases rather than two). Using values from ref. (46), $\Delta G=\Delta H-T\Delta S$ yields a rough estimate of $\Delta G_{unstack} = +2.1$ kcal/mol at 298 K,

corresponding to an unstacked population of 3%. This suggests that our model's estimate of 6% is a reasonable value based on stacking energetics.

Base stacking plays a critical role in determining the structural free energy landscapes of RNA and DNA. The work presented here provides insight into the thermodynamics of base stacking in RNA and the photophysical behavior of the FBAs that are widely used to study it. Future work will include FDCD measurements on more complex RNA systems and FDCD measurements with FBAs other than 2-AP.

EXPERIMENTAL METHODS

Materials

RNA di- and trinucleotides were purchased from Dharmacon (Horizon Discovery) and deprotected and desalted by the manufacturer. 2-AP riboside was purchased from TriLink Biotechnologies and 2-AP nucleobase was purchased from Sigma Aldrich. Except where otherwise noted, all measurements were performed in a buffer containing 20 mM Na_iPO_4 and 100 mM NaCl at pH 7.5.

Spectroscopy

FDCD and CD measurements were performed on a Jasco J1500 circular dichroism spectrometer with the sample in a 1 cm pathlength cylindrical cell inserted into a Jasco FDCD-551 cell holder. This holder envelops the cell in an elliptical mirror,[48] which directs fluorescence into a PMT (Hamamatsu R374) at 90 degrees to the excitation light. A long-pass colored glass filter with a 380 nm cutoff was placed in front of the fluorescence detector to remove scattered light. Scans were performed with an excitation bandwidth of 4 nm, an integration time of 4 s, and a scan speed of 20 nm/minute. The spectra that are shown are the average of 10 scans for FDCD and 5

scans for CD, and samples were measured at a concentration of 5 μM. The measurement channels "FDCD" and "DC" were both recorded, with the former yielding signal proportional to F_L-F_R, and the latter yielding signal proportional to F_L+F_R (essentially, the fluorescence excitation spectrum without correction for lamp intensity at different wavelengths) (Figure A2). FDCD baselines were recorded individually for each sample using the achiral 2-AP nucleobase (Figure 3.1A, R=H) at a concentration that yielded the same brightness as the sample when excited at 305 nm. CD, absorbance and fluorescence baselines were recorded using buffer.

Thermal ramps were carried out at a concentration of 20 μM, ramping from 7 °C to 80 °C at a rate of 1 °C per minute while monitoring absorbance at 308 nm. Fluorescence emission spectra were recorded on a Molecular Devices SpectraMax I3 fluorometer using a plate reader attachment with excitation at 295 nm and the sample at a concentration of 500 nM. Fluorescence lifetime measurements were performed on a Horiba Fluoromax-5 with a TemPro lifetime system using a NanoLED340 pulsed light source and the same long-pass filter used for FDCD. Sample concentrations were 1 μM for 2-AP riboside and 5 μM for all other samples. Instrument response functions were collected using a dilute suspension of Ludox. The full width at half-maximum (FWHM) of the instrument response function (IRF) was approximately 900 ps and the bin width was 55 ps.

Thin-layer chromatography

TLC experiments were performed using silica gel 60G F254 plates and a solvent system consisting of 50:40:3:15 *n*-butanol:acetone:33% ammonia:water, as previously described.[49] 1 nanomole of nucleoside or dinucleotide was spotted and, after development, the plate was imaged on a 302 nm ultraviolet transilluminator.

Data analysis

Most data processing and analysis was performed in Mathematica (Wolfram Alpha). The FDCD spectrum of 2-AP nucleobase was subtracted from the FDCD spectrum of the sample, and the DC spectrum of the solvent was subtracted from the DC spectrum of the sample. θ was then calculated by dividing the FDCD spectrum by the DC spectrum (Figure S3). We utilized the absorption spectra of 2-AP nucleoside in pure H_2O as a proxy for the absorption spectra of the *fluorophore* for all aqueous samples containing a single 2-AP residue. Its spectrum was scaled to a value of 6,000 L/mol·cm at its longest-wavelength absorption peak, generating ε_F, which was then utilized in processing of FDCD spectra.[33] The absorption spectrum of 2-AP dinucleotide in pure H_2O was used to generate its own ε_F spectrum by scaling to a peak value of 12,000 L/mol·cm. Likewise, absorption spectra of 2-AP nucleoside and dinucleotide in 30% ethanol were used to generate ε_F spectra for analysis of the corresponding FDCD spectra.

The relative hypochromicity of the stacked conformation of C(2-AP)C was estimated by calculating the difference in 308 nm absorbance between C(2-AP)C and 2-AP nucleoside at the minimum and maximum temperatures sampled (7 °C and 80 °C, respectively; Figure A7). The difference at 80 °C was then subtracted from the difference at 7 °C, and the resulting value was divided by the absorbance of the trinucleotide at 7 °C. This yielded a value of 0.16, so we concluded that the extinction coefficient of the unstacked conformation was 1.16 times that of the stacked conformation. Taking $\varepsilon_{un} = \varepsilon_{nuc}$, we thus used $\varepsilon_{st} = 0.86\ \varepsilon_{nuc}$ in our 2-extinction coefficient models. The system of eqs 3 and 7 has two solutions when separate extinction coefficients are used for the stacked and unstacked conformations, but only one is physically meaningful (the other has a stacked concentration that exceeds the overall sample concentration).

Fluorescence lifetime data were analyzed in Horiba Decay Analysis Software v6.6. 3-exponential models were used for all samples, and inclusion of additional exponentials yielded negligible improvement in the χ^2 value and residuals (fitting parameters are in Table A1). Due to the 900 ps IRF width, decays with apparent time constants below 200 ps were considered unreliable and were subsumed into the dark population in downstream analysis. With <200 ps components excluded, the average observed lifetime was calculated according to $\langle\tau\rangle_{obs} = \Sigma\alpha_i\tau_i$, where τ_i is the time constant of exponential decay component i and α_i is its amplitude. The dark population of molecules with lifetimes that were too short to resolve, α_0, was calculated according to $\alpha_0 = 1- \langle\tau_{nuc}\rangle/(\langle\tau_{sample}\rangle R)$, where $\langle\tau_{nuc}\rangle$ is the average lifetime of 2-AP riboside, $\langle\tau_{sample}\rangle$ is the average lifetime of the sample, and *R* is the ratio of the steady-state fluorescence intensity of 2-AP riboside to the sample.[50] The amplitudes of the decay components were then corrected to account for the dark population according to $\alpha_{ic} = \alpha_i(1-\alpha_0)$.

ASSOCIATED CONTENT

Supporting Information Available: Quantification of fluorescence intensities of all samples, TCSPC data and fits, unprocessed FDCD spectra, TLC image, plots of R_ϕ and c_{un} under different models, thermal ramp data, comparison of spectra in buffer and 30% ethanol are in Appendix A.

ACKNOWLEDGMENT

This work was funded by NIH R00 GM120457 to J. R. Widom

CHAPTER IV

PROBING AND PERTURBING RIBOSWITCH FOLDING USING A FLUORESCENT BASE ANALOGUE

The contents of this chapter have been previously published in whole or in part. The text present here has been modified from the publication below:

Hoeher, J. E.; Sande, N. E.; Widom, J. R. Probing and Perturbing Riboswitch Folding Using a Fluorescent Base Analogue. *Photochem. Photobiol. n/a* (n/a). https://doi.org/10.1111/php.13896.

BRIDGE

While FDCD is a powerful tool for studying RNA, it has been underutilized in the years since it was first used. Due to this, experiments were needed on smaller systems to properly understand what was happening. With CD and fluorescence spectroscopy being more well-established techniques, more complicated systems could be investigated to understand how perturbations in RNA structure impact its function. Work was done on the smaller system, and then moving to the more complex system.

INTRODUCTION

Riboswitches are mRNA segments that regulate gene expression in response to environmental cues, and are most commonly found in bacteria.[1] A riboswitch contains an aptamer domain, which binds to a ligand, and an expression platform, which re-folds in response to ligand binding to regulate downstream genes in *cis*. Riboswitches typically control the transcription or translation step of gene expression, although other mechanisms have also been observed.[2-4] Since their discovery, riboswitches have been the subjects of intensive study due to their utility as molecular sensors[5,6] and antibiotic targets.[7,8]

The structures and dynamics of riboswitches are intimately linked to their biological functions. As a result, many techniques have been used to probe riboswitch structure and dynamics, including x-ray crystallography,[9] NMR,[10,11] single-molecule Förster resonance energy transfer (smFRET)[12-15] and bulk fluorescence spectroscopy.[4,16] For studies utilizing bulk fluorescence spectroscopy, a powerful approach is to replace a base within the riboswitch with a fluorescent base analogue (FBA), with the most commonly used FBA being the adenine (A) analogue 2-aminopurine (2-AP; Fig. 4.1).[17] Fluorescence from 2-AP is modulated by its structural context, with stacking on neighboring bases typically inducing quenching,[18] and changes in polarity additionally inducing spectral shifts.[19] While FBAs are designed to preserve the Watson-Crick base pairing properties of the corresponding native bases, 2-AP has been shown to alter the structure and dynamics even of double-stranded DNA.[20] FBAs may impact structural features that rely on non-Watson-Crick interactions to an even greater degree, and such interactions are common in the complex 3-dimensional structures that riboswitches and other RNAs can adopt.[21] Some FBAs have been reported that preserve both the Watson-Crick and Hoogsteen faces of adenine, providing effective surrogates in a wide range of structural and enzymatic contexts,[22-24] but lack of commercial availability has significantly limited their uptake. Due to this factor and its decades-long record as a useful probe, 2-AP remains by far the most widely used FBA despite having suboptimal structural and photophysical properties.

To minimize structural perturbations, 2-AP is ideally placed at locations containing non-conserved nucleotides whose hydrogen bonding interactions are not altered by 2-AP substitution. It has been noted that these criteria are satisfied by as many as 10-15% of nucleotides in various

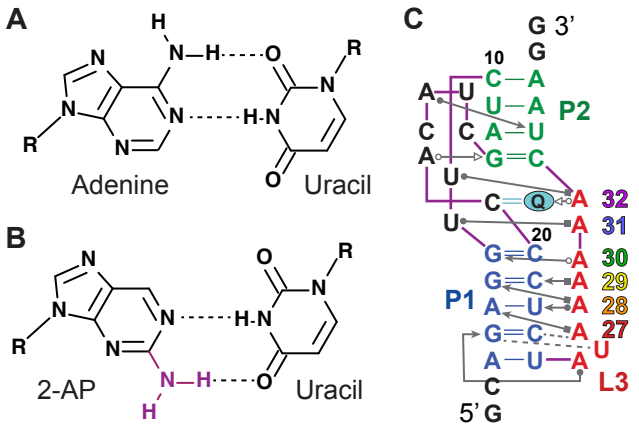

Figure 4.1 2-Aminopurine and the preQ$_1$ riboswitch. (A) Chemical structure of a Watson-Crick base pair between adenine and uracil. (B) Chemical structure of a Watson-Crick base pair between 2-AP and uracil. The re-positioned amine group is shown in purple. (C) The preQ$_1$ riboswitch in its docked pseudoknot conformation, shown in Leontis Westof notation.[25] The P1, P2 and L3 domains are indicated in blue, green and red, respectively, and preQ$_1$ is shown in cyan. Adenosine residues in L3 are numbered according to the color scheme used in subsequent figures.

riboswitches.[25,26] However, certain sites may be of interest precisely because of their high degree of conservation and non-canonical hydrogen bonding interactions. In these circumstances, 2-AP substitution may act as a perturbing "mutation" that serves concurrently as a spectroscopic probe. If its structural impacts are accounted for, 2-AP can be a useful tool even at highly conserved or structurally complex sites. The approach of using an FBA as a concurrent probe and mutation would be particularly valuable for the study of riboswitches for which high-resolution structures are not available. For such riboswitches, the significance of particular residues is typically inferred through mutagenesis and biochemical methods such as chemical secondary structure probing. FBAs such as 2-AP offer a chemical library of potential "mutations" that expands the 3-member library of native base substitutions, and, like the varied reagents used for secondary structure probing,[27] different FBAs are sensitive to different aspects of RNA structure (for example, see ref. (28) for a comparison of 2-AP and the cytosine analogue pyrrolocytosine). Combining biochemical and spectroscopic approaches thus offers the potential to expand the level of insight that can be gained in the absence of high-resolution structures.

We utilized 2-AP as a concurrent probe and mutation to study the significance of tertiary interactions involving highly conserved adenosine residues in the Class 1 $preQ_1$ riboswitch from *Bacillus subtilis* (*Bsu*; Fig. 4.1c), which is responsible for regulating genes involved in synthesis of the hypermodified nucleobase queuosine.[29] This riboswitch binds to the metabolic intermediate $preQ_1$, causing a conformational change that suppresses expression of genes involved in the production of queuosine by enhancing transcription termination.[12] Its aptamer domain contains a stem-loop structure (P1) followed by an A-rich tail (L3), and $preQ_1$ binding stabilizes a pseudoknot-structured "docked" conformation containing a second helix, P2.[9] The L3 domain of this riboswitch contains a stretch of 6 highly conserved A residues that participate in a complex network of hydrogen bonding with the minor groove of the P1 helix and the ligand-binding pocket (Fig. 4.1c).[9-11] 2-AP has been utilized extensively in Class I $preQ_1$ riboswitches, particularly those from *Thermoanaerobacter tengcongensis* (*Tte*)[30,31] and *Fusobacterium nucleatum* (*Fnu*),[4] with some prior work in *Bsu*,[16] but L3 residues have gone mostly uninvestigated. The kinetics of structural rearrangements of residue A24 in the *Tte* $preQ_1$ riboswitch (most closely analogous to A28 in *Bsu*; Fig. 4.1c) were investigated using 2-AP, revealing almost no change in fluorescence in response to Mg^{2+} and a moderate decrease in response to $preQ_1$.[30] However, that base resides in a different sequence context, A(2-AP)C, than the corresponding residue A28 in the *Bsu* riboswitch, A(2-AP)A, and the L3 domain is one nucleotide longer in *Tte*.

We investigated riboswitch variants in which 2-AP replaced subsets of the six consecutive A residues in the L3 domain. Rather than pursuing structurally neutral FBA labeling sites, this work uses 2-AP to introduce site-specific disruptions in the structure. We used fluorescence spectroscopy to investigate how ligand binding affects the local environment at

each labeling site, and to determine the affinity of each variant for $preQ_1$. These measurements revealed a rich variety of photophysical impacts on 2-AP, which can be attributed to changes in both base stacking and local polarity that occur upon ligand binding.[19] Fluorescence lifetime measurements on a subset of variants revealed that 2-AP samples multiple local environments and that ligand binding changes their relative prevalence. We additionally performed absorbance-based measurements that allowed us to directly compare the native riboswitch to the 2-AP-modified variants, which is not possible using fluorescence spectroscopy. Specifically, we used circular dichroism (CD) spectroscopy and thermal denaturation experiments to study the effects of 2-AP and $preQ_1$ on the structure and stability of the riboswitch. We found that at every labeling site tested, 2-AP decreases the affinity of the riboswitch for $preQ_1$, but the riboswitch still undergoes a global conformational change of a similar nature at sufficiently high ligand concentrations. Placing 2-AP distal to the ligand binding pocket makes the riboswitch more susceptible to thermal denaturation in the absence of $preQ_1$, whereas the largest decreases in affinity were observed with 2-AP proximal to the binding pocket. Our results reveal that interactions involving the 6-amino groups of the A residues in L3 are critical for efficient ligand binding by the $preQ_1$ riboswitch, and that the formation of these interactions is coupled to changes in base stacking and polarity.

MATERIALS AND METHODS

RNA oligonucleotides were purchased from Dharmacon (Horizon Discovery) and DNA oligonucleotides were purchased from Integrated DNA Technologies (sequences in Table B1).

All modified oligonucleotides were HPLC-purified by the manufacturer, and the 3' segments were purchased with a 5' phosphate. Riboswitch samples were prepared by splinted ligation using T4 RNA ligase 2 (New England Biolabs M0239S). 5 nanomoles each of the 5' and 3' segments of the riboswitch and the DNA splint were combined and heated to 90 °C for 2 minutes and then allowed to cool to RT over 10 minutes. The manufacturer-provided RNA ligase 2 reaction buffer was added 30 seconds into cooling. After cooling, the mixture was diluted in reaction buffer to a total volume of 150 µL and 60 units of T4 RNA ligase 2 were added. The reactions were incubated at room temperature for 3 hours, then resolved on a 15% polyacrylamide-urea gel. The product band was recovered from the gel by electroelution using a BioRad model 422 electro-eluter followed by ethanol precipitation in the presence of 300 mM NaOAc, pH 5.3. 2-AP riboside was purchased from Tri-Link Biotechnologies.

All spectra were recorded at 20 °C with the sample in a buffer consisting of 20 mM Na_iPO_4 at pH 7.5 and 100 mM NaCl. Samples were heated to 90 °C for 2 minutes and then crash-cooled in ice water for 10 minutes before measurement in order to allow the RNA to fold without dimerizing. Where noted, $MgCl_2$ was added after cooling to a final concentration of 1 mM. CD spectra and melting curves were recorded on a Jasco J-1500 spectrometer. Melting curves were recorded with the riboswitch at a concentration of 2 µM or AA(2-AP)AC at a concentration of 16 µM. The sample was heated at a rate of 0.75 °C per minute in a 1 cm path-length, low head-space cuvette (Starna 26.160/LHS) while monitoring CD and absorbance at a wavelength of 258 nm. CD spectra were recorded in a 1 cm path-length cuvette (Starna 16.160-10) with the riboswitch at a concentration of 2 µM. Scans were performed from 200 to 350 nm at a rate of 10 nm per minute with an integration time of 4 seconds and an excitation bandwidth of 2 nm, and four sequential scans were averaged together. CD titrations were performed with the

riboswitch at a concentration of 50 nM in a 2 cm path-length cuvette. Spectra and melting curves were background-corrected by subtracting off a buffer scan (including $preQ_1$ where appropriate). CD spectra were converted from units of millidegrees to extinction coefficient (L/mol*cm) using the following equation, where *CD* is the signal in millidegrees, *C* is the concentration in mol/L and *L* is the path length in cm:

$$\Delta\varepsilon = \frac{CD}{32980 \cdot C \cdot L}$$

Finally, they were converted to Δε per nucleotide by dividing by the number of nucleotides in the riboswitch, 38.

A fitting procedure was performed in Mathematica (Wolfram Research) to extract melting temperatures (T_m) and transition widths (ΔT) from melting curves.[33] First, a linear fit was performed to the segment of the melting curve recorded between 75 and 80 °C, and was extrapolated to lower temperature. The absorbance vs. temperature curve was then converted to a proxy for the "fraction folded" at temperature *T*, θ(*T*), using the following equation:

$$\theta(T) = \frac{L(T) - A(T)}{L(T) - A(T_{min})}$$

where $L(T)$ is the value of the linear fit at temperature *T*, $A(T)$ is the recorded absorbance at temperature *T*, and $A(T_{min})$ is the recorded absorbance at the lowest temperature. $\theta(T)$ was then fit using the following equation:

$$\theta(T) = \frac{a}{1 + e^{(T - T_{M1})/\Delta T_1}} + \frac{b}{1 + e^{(T - T_{M2})/\Delta T_2}}$$

where *a* and *b* are the weights, T_{M1} and T_{M2} are the melting temperatures, and ΔT_1 and ΔT_2 are the widths of unfolding transitions 1 and 2, respectively. Each experimental replicate was fit

individually, then the average and standard deviation of the resulting parameter values were determined.

Fluorescence spectra were recorded on an Edinburgh FS5 fluorometer with the RNA at a concentration of 500 nM. After each addition of ligand, the sample was briefly pipette mixed, stirred in the sample holder of the fluorometer for 4 minutes, then allowed to rest for 1 minute before scanning. Scans were performed from 325 to 500 nm with an excitation bandwidth of 5 nm at 305 nm, an emission bandwidth of 2 nm, and an integration time of 1 s. To account for the minor effect of dilution of the RNA due to ligand addition, spectra were corrected according to the following equation:

$$I_{cor} = I_L \cdot \frac{V_0 + V_L}{V_0}$$

where I_{cor} is the concentration-corrected intensity, I_L is the uncorrected intensity at ligand concentration L, V_0 is the initial volume of sample before any ligand was added, and V_L is the cumulative volume of ligand that had been added before I_L was measured.

The absorption spectrum of a 50 μM solution of $preQ_1$ was recorded and used to correct fluorescence spectra for the inner filter effect using the following equation:

$$I_{cor2} = I_{cor} \frac{2.303 \cdot A_{305}}{1 - 10^{-A_{305}}}$$

where I_{cor2} is the concentration- and inner filter effect-corrected intensity and I_{cor} is the concentration-corrected intensity. A_{305} is the total absorbance of the sample at the excitation wavelength of 305 nm, calculated according to:

$$A_{305} = [RNA] \cdot 6000 + [preQ_1] \cdot 2166$$

where 6000 L/mol*cm is the extinction coefficient of 2-AP, and 2166 L/mol*cm is the extinction coefficient of $preQ_1$ at 305 nm determined from its absorbance spectrum. λ_{max} was extracted by performing a Gaussian fit to the region of the spectrum between 350 and 380 nm.

3 replicates were performed for each fluorescence titration, the corrected fluorescence intensities or λ_{max} values were averaged together, then the resulting curve was converted into fractional saturation (FS; scaled to run between 0 and 1). It was then fit with the following equation to extract an apparent K_D, where R is the RNA concentration, L is the ligand concentration, and a is a scaling factor:

$$FS = a \cdot \left(\left(K_D + R + L \right) - \left(\frac{\left(\left(K_D + R + L \right)^2 - 4RL \right)^{1/2}}{2R} \right) \right)$$

Fluorescence lifetime measurements were performed via time-correlated single photon counting on the Edinburgh FS5 in reverse mode using a 320 nm pulsed LED for excitation. Three replicates were performed for each sample, and a reconvolution fit was performed on each replicate in Edinburgh's Fluoracle software. A 4-exponential model was required to achieve adequate fits for all riboswitch measurements (Table B2), whereas 2-AP riboside required only a single exponential. Average observed lifetimes $\langle \tau \rangle_{obs}$, dark populations α_0 and corrected amplitudes of decay components α_c were computed from the resulting fitting parameters as previously described.[18,34] One of the four exponential components had a lifetime of <100 ps for all samples tested. Its population and lifetime were considered unreliable due to the ~1 ns full width at half maximum of the instrument response function, so it was subsumed into the dark population in downstream analysis.

RESULTS AND DISCUSSION

The *Bsu* $preQ_1$ riboswitch contains six consecutive A residues in its L3 domain, making it a natural system in which to employ 2-AP substitution. We prepared an unmodified riboswitch that lacked 2-AP, singly-labeled variants that contained 2-AP in position 27, 28, 29, 30, 31, *or* 32, as well as doubly-labeled variants containing 2-AP at positions 27 *and* 28, 30 *and* 31, or 31 *and* 32 (Fig. 4.1c). The bases in L3 are highly conserved,[29] suggesting that alteration of them through 2-AP substitution could have detrimental impacts on riboswitch structure and function. Perhaps as a consequence of this, 2-AP labeling sites have been almost entirely limited to other locations in the $preQ_1$ riboswitches from both *Bsu*[16] and other organisms.[4,30,31] To account for this fact, we employed absorbance-based measurements that allowed us to directly compare modified and unmodified riboswitch variants, in addition to fluorescence measurements that exploited the sensitivity of 2-AP to local RNA structure.

Fluorescence spectroscopy: ligand affinity and comparison of modified variants

2-AP fluorescence exhibited a variety of behaviors at different labeling sites within L3. All riboswitch variants were quenched at least 4-fold compared to free 2-AP riboside, which is unsurprising given that 2-AP fluorescence is quenched as a result of base-stacking.[18,19,35] Variants in which 2-AP is flanked by two A residues all exhibited similar fluorescence intensities in the absence of Mg^{2+} and $preQ_1$, with a 20% difference in intensity between the brightest of them (position 30) and the darkest (position 29) (Fig. 4.2). Variants with 2-AP flanked by U and A (position 27) or A and C (position 32) both exhibited fluorescence only about half as intense as the other four. A short oligonucleotide containing 2-AP in the same sequence context as A31, AA(2-AP)AC, exhibited a very similar intensity and peak wavelength (λ_{max}) to the position 28-31 variants, suggesting that these spectra are characteristic of 2-AP in a generic oligo(A) context

rather than being altered significantly by the structure of the riboswitch. This is consistent with previous NMR measurements, which showed that in the absence of divalent cations (like most of our measurements), the sequence of L3 adopts a single-stranded A-form conformation both in the riboswitch and as an isolated 12-mer.[36] In contrast, in the presence of Mg^{2+}, preorganization of L3 has been observed by MD simulations[37] and smFRET.[12,14] To investigate this further, we recorded spectra of the position 29 and 31 variants in the presence of 1 mM $MgCl_2$. While the fluorescence intensity of each variant was nearly unchanged by addition of Mg^{2+}, a small (0.7 nm) but resolvable blueshift was observed for position 31 and a larger one for position 29 (2.5 nm), suggesting that 2-AP is in a more nonpolar environment in the presence of Mg^{2+}.[19]

Ligand titrations were performed using fluorescence emission spectroscopy to assess the structural changes induced by $preQ_1$ binding and to estimate the affinities of 2-AP-modified variants for $preQ_1$ (Figs. 4.2, B1 and B2, Table 4.1). A CD titration was performed on the unmodified riboswitch for comparison (Fig. B3). While binding affinities (K_D) can be obtained more directly by methods that detect thermodynamic changes that occur upon binding, such as microscale thermophoresis[38] and isothermal titration calorimetry,[39] 2-AP fluorescence has the benefit of simultaneously reporting on changes in the local environment at the labeling site. In the absence of Mg^{2+}, the apparent K_D values (K_{app}) of 2-AP-labeled variants ranged from 360 nM with 2-AP at position 29 to over 20,000 nM for positions 31 and 32, in stark contrast to the value of 28 nM determined for the unmodified riboswitch via CD. Placing 2-AP at position 28 was quite detrimental (K_{app} = 12,800 nM), which is surprising given that that site is the least conserved of the six.[29] The fluorescence intensity and spectrum of each variant responded to $preQ_1$ in a distinct manner, though the functional significance of these changes must be considered in light of the dramatic weakening of ligand binding in certain variants. Nevertheless,

there was no obvious correlation between the affinity of a variant for $preQ_1$ and the magnitude of the changes in its fluorescence intensity or λ_{max}, showing that even if 2-AP substitution at a particular site decreases affinity, that residue may still undergo significant structural rearrangements at ligand concentrations sufficiently high for binding. Furthermore, our CD and thermal denaturation measurements (detailed below) indicate that the impacts of $preQ_1$ on the global structure and stability of the riboswitch are similar for unmodified and modified variants. These observations suggest that 2-AP fluorescence provides meaningful information about how the local environments of L3 residues differ between the pre-docked and ligand-stabilized docked conformations.

Variant	ΔI (cts)	$\Delta I/I_0$	$\Delta\lambda_{max}$ (nm)[1]	K_{app} (nM)
27	+1,800	+8%	-2.8	7,900 (3,700)[2]
28	+19,600	+36%	-1.6	12,800 (9,100)[2]
29	-19,400	-40%	-4.3	360 (730)[2]
29+1 mM Mg^{2+}	-13,600	-27%	-2.2	35 (82)[2]
30	-41,400	-68%	+0.3	4,800
31	-7,200	-12%	+0.1	24,900
31+1 mM Mg^{2+}	+10,700	+19%	+0.7	19,000
32	-7,100	-25%	+0.4	28,400

Table 4.1 Fluorescence titrations results. ΔI: change in maximum intensity from 0 nM $preQ_1$ to the highest concentration measured. $\Delta I/I_0$: change in intensity relative to intensity in the absence of ligand. $\Delta\lambda_{max}$: change in maximum wavelength from starting to ending point. K_{app}: apparent K_D determined by fitting titration curve.

[1]Typical standard deviations in λ_{max} were ± 0.2–0.5 nm.

[2]Based on λ_{max}. All other values are based on I_{max}.

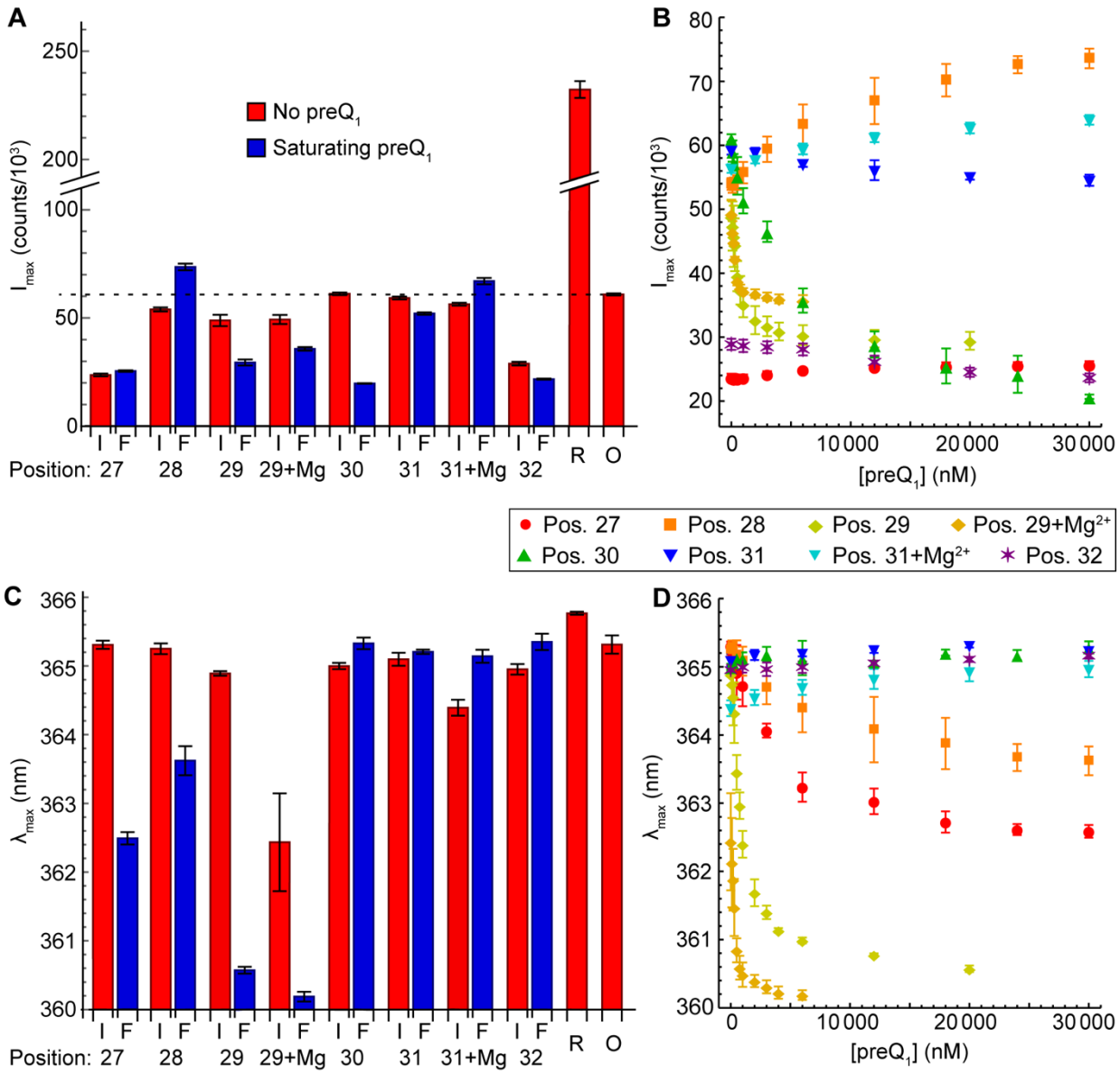

Figure 4.2 Fluorescence measurements. "+Mg" indicates that the measurement was performed in 1 mM $MgCl_2$. (A) Peak fluorescence intensity of each 2-AP-modified riboswitch variant (positions 27–32) at the initial concentration of 0 nM $preQ_1$ (I, red) or the final (highest) concentration measured (F, blue). R = 2-AP riboside. O = oligonucleotide AA(2-AP)AC. The dashed line indicates the fluorescence intensity of AA(2-AP)AC. (B) I_{max} versus [$preQ_1$] for each variant over the range of 0–30,000 nM $preQ_1$ (full ranges shown in Figures S1 and S2). (C) Initial and final peak fluorescence wavelengths of riboswitch variants, 2-AP riboside and AA(2-AP)AC. (D) λ_{max} versus [$preQ_1$] for each riboswitch variant. In panels b and d, red: position 27; orange: position 28; yellow: position 29; green: position 30; blue: position 31; purple: position 32. Error bars show the standard deviation across measurements on three samples.

In addition to having the lowest fluorescence intensities in the absence of $preQ_1$, the position 27 and position 32 variants also exhibited the smallest absolute changes in 2-AP fluorescence intensity upon ligand addition, with position 27 exhibiting an increase of only ~1,800 counts (8%). This slight change in intensity was non-monotonic as a function of $preQ_1$ concentration (Fig. B4), leading to a titration curve fit that was significantly poorer (R^2=0.982) than all other variants (R^2=0.996-0.999). This variant exhibited the second-largest change in λ_{max} upon addition of $preQ_1$, and the concentration-dependence of λ_{max} was much better fit (R2=0.998) than I_{max}. This yielded a K_{app} of 3,700 nM, which is likely to be more reflective of this variant's ligand binding behavior than the I_{max}-based value of 7,900 nM. The most significant changes in fluorescence intensity were observed with 2-AP at positions 28 (+36%), 29 (-40%) and 30 (-68%). Interestingly, the equivalents of our positions 29 and 30 are the only sites in L3 that exhibit reduced scission in the presence of $preQ_1$ in in-line probing measurements, indicating an increase in the structural rigidity of the backbone.[29] These variants were strongly quenched upon addition of $preQ_1$, indicating that this increase in rigidity is accompanied by more extensive stacking on neighboring bases.

The *Tte* $preQ_1$ riboswitch was found to tolerate 2-AP substitution at a variety of sites in the presence of 2 mM $MgCl_2$ with only modest changes in K_D, though K_D was not determined for any A-to-2-AP substitutions in L3.[30] It is possible that the riboswitch is more tolerant of 2-AP substitution in the presence of Mg^{2+}, so we investigated its impact on one strongly binding (position 29) and one weakly binding (position 31) variant. While addition of 1 mM Mg^{2+} to the position 31 variant only modestly improved its K_{app} (from 24,900 to 19,000 nM), it changed the response of 2-AP to $preQ_1$ from a slight decrease in intensity and no spectral shift to a slight redshift and increase in intensity. In contrast, position 29 retained the blueshift and quenching

that it had exhibited in the absence of Mg^{2+}, but with a significant improvement of K_{app} from 390 nM to <100 nM.

As noted above, spectral shifts upon ligand addition were observed with 2-AP certain sites. Blueshifts in the emission spectrum occurred upon ligand addition with 2-AP at positions 27 (-2.8 nm), 28 (-1.5 nm) and 29 (-4.3 nm in the absence of Mg^{2+}, -2.2 nm in the presence of 1 mM Mg^{2+}) (Fig. 4.2 and Table 4.1). The other sites showed shifts no greater than 0.7 nm. Position 29 showed the largest blueshift, in keeping with its large change in fluorescence intensity. In stark contrast, position 30, which showed the largest absolute and relative change in intensity, showed no blueshift. It has been shown previously using deoxynucleosides that changes in base-stacking alone do not lead to spectral shifts in 2-AP fluorescence, while a decrease in solvent polarity causes both blueshifts and quenching.[19] In the $preQ_1$ riboswitch, NMR and x-ray crystal structures show that in the presence of ligand, the bases in L3 stack in sets of 2.[9,11] A27 and 28 form a parallel stack with one another, as do A29 and 30, as do A31 and 32, with changes in angle existing between each set of stacked bases. A29-32 are nearly co-planar with distal bases, including base pairs in P1 in the case of A29 and A30, and U8 and U9 in the case of A31 and A32 (Fig. 4.1c). A28 is notably displaced and tilted relative to A29, breaking the chain of stacking and potentially explaining the increase in 2-AP fluorescence upon addition of ligand when it is at position 28. A pattern emerges when these stacking partners are considered as units. In the absence of Mg^{2+}, 2-AP fluorescence increases upon addition of ligand in the 27-28 stack, decreases strongly in the 29-30 stack, and decreases slightly in the 31-32 stack. Superimposed on this pattern of fluorescence intensity changes, the three bases distal to the ligand binding pocket[27-29] exhibit blueshifts upon ligand addition while the three proximal bases do not.

The combination of blueshift and de-quenching observed with 2-AP at positions 27 and 28 is surprising, given that increased stacking would appear most likely to accompany a more nonpolar environment, while position 29 exhibits the more intuitive combination of blueshifting and quenching. It is important to note that the $preQ_1$ riboswitch is known to sample multiple conformations under the experimental conditions utilized here,[12-14] and steady-state emission spectra provide a population- and intensity-weighted average across this ensemble of structures. To investigate the distribution of structures present in solution, we performed fluorescence lifetime measurements using time-correlated single photon counting (TCSPC), focusing on the two variants that showed the largest spectral shifts upon ligand addition, positions 27 and 29 (Table 4.2 and Fig. B5). Both variants were investigated in the absence and presence of saturating $preQ_1$, and the position 29 variant was additionally investigated in the presence of 1 mM $MgCl_2$.

Sample	Mg^{2+}	$preQ_1$	$\langle\tau\rangle_{obs}$ (ns)	α_0 (%)	α_{1c}	τ_1	α_{2c}	τ_2	α_{3c}	τ_3
2-AP riboside	0 mM	0 mM	8.85	0					100	8.85
Position 27	0 mM	0 uM	3.4	74	17	2.1	8	5.2	1	10.4
Position 27	0 mM	42 uM	2.4	60	26	1.1	13	4.3	1	10.8
Position 29	0 mM	0 uM	3.6	49	24	1.9	21	4.3	5	9.0
Position 29	0 mM	20 uM	2.3	50	37	1.6	10	3.5	2	8.9
Position 29	1 mM	0 uM	3.4	45	29	1.8	20	4.1	6	8.9
Position 29	1 mM	20 uM	2.6	49	39	1.9	11	4.7	1	12.8

Table 4.2 Observed average lifetime ($\langle\tau\rangle_{obs}$), and populations (α_{ic}) and lifetimes (τ_i) of individual decay components obtained through TCSPC. Note: α_0 is a dark population whose decay timescale is not resolved ($\tau < 100$ ps). The populations α_{ic} have been corrected to account for the presence of the dark population. Percentages may not add up to 100 due to rounding.

Four exponential components were required to adequately fit the resulting fluorescence decays, which was unsurprising considering the complex decays observed even for systems as

small as di- and trinucleotides.[18,40-42] Under all conditions tested, the decay time constants of both variants fell within the ranges of 10.9±2, 4.5±1, and 1.6±0.5 ns, along with a significant dark population with decay timescales too fast to resolve accurately with our instrumentation (Table 4.2). In all three cases (position 27 without Mg^{2+}, and position 29 with and without Mg^{2+}), addition of $preQ_1$ increased the weight of the 1.6±0.5 ns component (Table 4.2). The conformation that exhibits this decay may therefore be responsible for the blueshift in fluorescence that occurs upon ligand addition in all three cases. Supporting this interpretation, the increase in weight of the ~1.6 ns component is most significant for the condition that exhibits the largest blueshift: position 29 in the absence of Mg^{2+}. It has been previously shown that solvent effects alone are sufficient to shorten the fluorescence lifetime of 2-AP free base from >10 ns in neat H_2O to ~1.5 ns in neat dioxane.[19] The latter value is very similar to the 1.6±0.5 ns lifetime that we attribute to the "bluest" (most nonpolar) of the "bright" conformations that contribute significantly to the fluorescence of 2-AP at positions 27 and 29 in the $preQ_1$ riboswitch (the local polarity of the dark population is not reflected in the steady-state emission spectrum due to its small contribution to the overall fluorescence). Furthermore, the longest decay component of >8 ns is consistent with the lifetimes observed for free 2-AP base and nucleosides in aqueous solution.[18,19,42,43] Hence, this low-prevalence component likely originates from an extra-helical conformation of 2-AP,[42,43] which would be the most solvent-exposed and thus the "reddest".

With 2-AP at position 27, the increase in the weight of the ~1.6 ns component occurs through a shift of population away from the dark conformation, explaining this variant's increase in fluorescence intensity in the presence of $preQ_1$. This increase in the prevalence of the bluest bright conformation occurs without a concomitant increase in the extra-helical conformation,

explaining the observed blueshift upon ligand addition. With 2-AP at position 29, the increase in the ~1.6 ns component occurs through a shift away from the ~4.5 and ~10.9 ns decays in both the presence and absence of Mg^{2+}, explaining this variant's decrease in fluorescence intensity. The depletion of the extra-helical conformation contributes to the blueshift exhibited by this variant. We conclude that at positions 27 and 29, 2-AP can access a conformation that is protected from solvent but only moderately base-stacked (and thus bright enough to impact the steady-state emission spectrum). This conformation is enhanced upon ligand binding, and the accompanying changes in the emission intensity and spectrum are dictated by which alternative conformations are depleted.

CD spectroscopy and thermal denaturation: comparison of unmodified and modified variants

Absorbance-based measurements provided further insight into the behavior of L3, and into how 2-AP substitution alters the properties of the riboswitch. We recorded CD spectra and melting curves for each variant in the absence and presence of $preQ_1$. While it can be challenging to extract quantitative structural information from the ultraviolet CD spectra of structured RNAs, they allowed us to determine whether different variants adopted similar global structures to one another, and whether their global structures changed in a similar manner upon $preQ_1$ binding. Melting curves, which were recorded by monitoring CD and absorbance at 258 nm during heating, were used to assess the impacts of 2-AP and $preQ_1$ on the structural stability of the riboswitch. Unfolding is typically indicated by an increase in the absorbance signal and a decrease in the CD signal.

CD spectroscopy. We found that in the absence of $preQ_1$, the unmodified riboswitch exhibits a CD spectrum that is similar to those reported for other RNAs that adopt a pseudoknot structure.[45] When $preQ_1$ was added, the CD spectrum exhibited a pronounced shift to more negative values

(Fig. 4.3a), reflecting the shifting of equilibrium from the pre-docked (P2 not intact) to the docked (P2 intact) conformation.[12,13] In the absence of $preQ_1$, the spectra of the modified variants are quite similar to one another and slightly less intense than the spectrum of the unmodified riboswitch (Fig. B.6a). This difference indicates that 2-AP substitution causes a change in the electronic coupling between nearby bases that gives rise to the CD signal.[46,47] A decrease in the CD intensity upon 2-AP substitution is expected because of the differences in the electronic transitions of A and 2-AP, and should be most apparent when an AAA segment is replaced with an A(2-AP)A segment. Placing 2-AP at position 27 had the smallest impact on the lineshape and intensity of the CD spectrum, consistent with its position in a UAA context rather than an AAA context. These results suggest that all variants adopt similar global structures in the absence of $preQ_1$. In the longest-wavelength absorption band of 2-AP (centered at 305 nm), the CD spectra of modified and unmodified variants could not be distinguished from one another, so no attempt was made to extract structural information specific to the 2-AP labeling site.

Most absorbance-based experiments in the presence of ligand were done with $preQ_1$ at a concentration of 5 μM, which based on our K_{app} measurements is saturating for the unmodified riboswitch and nearly saturating for the position 29 variant. The absorption peak of $preQ_1$ lies at 260 nm, so for most variants, saturating concentrations of $preQ_1$ would have very significant impacts on overall sample absorbance in the UV. For example, for a moderate affinity variant like position 30, a 2 μM RNA sample containing a saturating concentration of 50 μM $preQ_1$ would have a total A260 of >1, half coming from $preQ_1$. Hence, for most variants, we did not

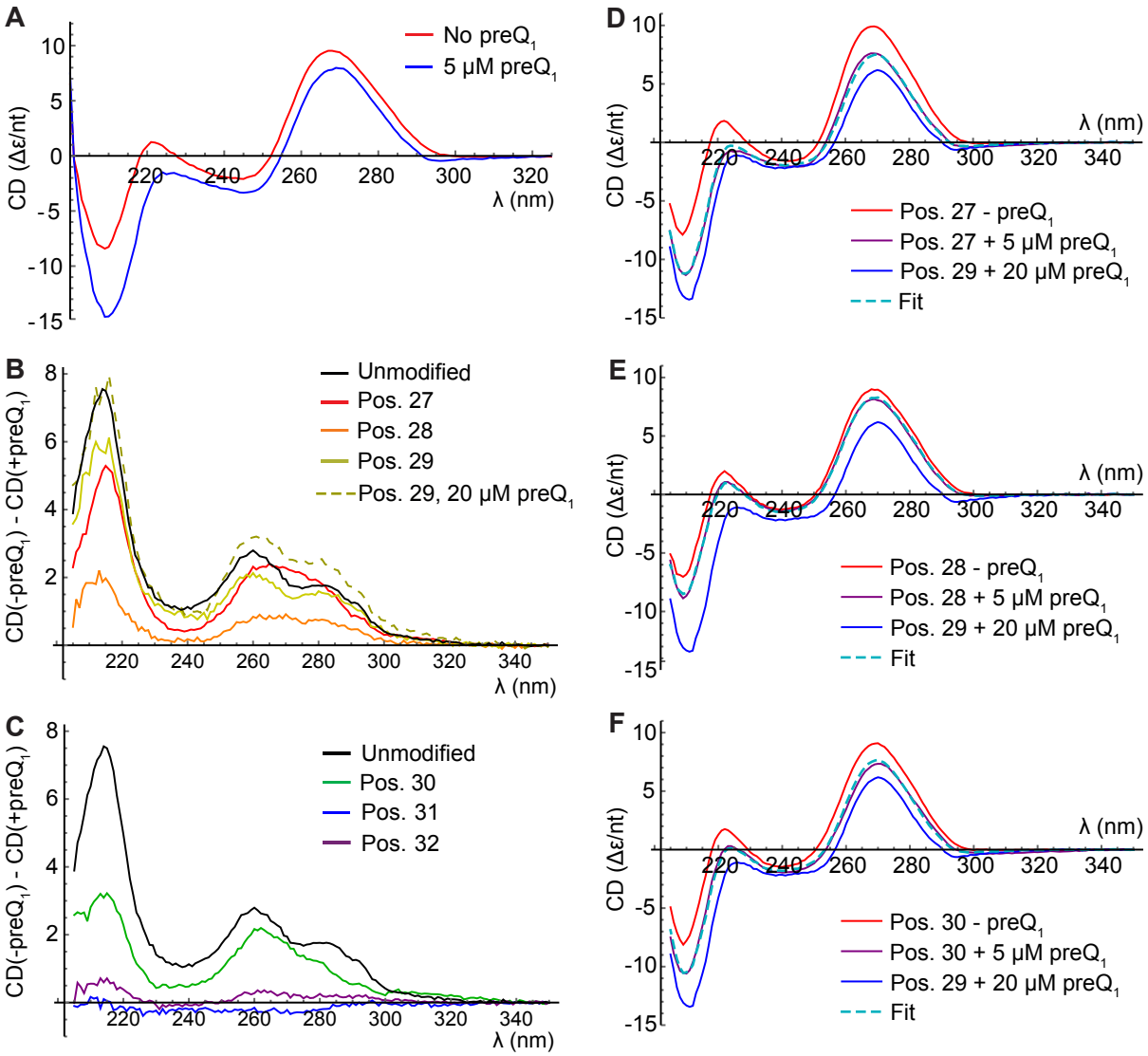

Figure 4.3 CD analysis of riboswitch variants in the absence of $MgCl_2$. (A) Spectra of unmodified riboswitch in the absence (red) or presence (blue) of 5 µM preQ1. (B, C) Difference spectra where the CD spectrum recorded in the presence of ligand has been subtracted from the CD spectrum recorded in the absence of ligand. (B) Difference spectra for unmodified riboswitch and variants with 2-AP at positions 27, 28 and 29 using 5 µM $preQ_1$, and position 29 using 20 µM $preQ_1$. (C) Difference spectra for unmodified riboswitch and variants with 2-AP at positions 30, 31 and 32, all using 5 µM $preQ_1$. (D–F) CD spectra fit with linear combinations of −$preQ_1$ and Position 29 + 20 µM $preQ_1$ spectra. (D) Position 27 + 5 µM $preQ_1$ (purple) fit as a linear combination (dashed cyan) of position 27 – $preQ_1$ (red) and position 29 + 20 µM $preQ_1$ (blue). (E) Corresponding plots for position 28. (F) Corresponding plots for position 30.

attempt to reach saturation in absorbance-based experiments, but instead considered the trends between the absence of $preQ_1$ and partial saturation.

Upon addition of $preQ_1$, the spectra of different variants became more distinct, with most exhibiting a general negative shift that was smaller than that exhibited by the unmodified riboswitch (Figs. 4.3 and B6). The position 29 variant was additionally measured at a saturating $preQ_1$ concentration of 20 μM, which induced a shift comparable in magnitude to that exhibited by the unmodified riboswitch (Fig. 4.3b). If this spectrum is characteristic of a fully $preQ_1$-bound riboswitch with a single 2-AP modification, partially saturated riboswitch spectra should be well fit with a linear combination of their respective -$preQ_1$ spectra and the saturated position 29 spectrum. This is indeed what was found for the variants with moderate responses to 5 μM ligand (positions 27, 28 and 30; Fig. 4.3d-f). The fits predict that positions 27, 28 and 30 are 63%, 24% and 49% bound, respectively, in the presence of 5 μM $preQ_1$, consistent with the trend in their K_{app} values (Table 4.1). Even the weakest binder based on K_{app}, the position 32 variant, exhibited negative shifts in the CD upon ligand addition at the same wavelengths as the unmodified riboswitch (Fig. 4.3c). This suggests that much of the variation in +$preQ_1$ CD spectra is due to incomplete saturation, and that these variants are capable of undergoing conformational changes of a similar nature to the unmodified riboswitch at sufficiently high ligand concentrations. 2-AP modification at positions 27-30 and 32 thus alters the affinity of the riboswitch for $preQ_1$ without altering the fundamental global structures it is capable of adopting.

In contrast, the CD spectrum of the second-weakest binder (position 31) exhibited a small *positive* shift upon ligand addition (Fig. 4.3c), suggesting that this variant does not undergo the same global conformational change as the others. We investigated this further by recording CD

spectra and fluorescence titrations on this variant in the presence of 1 mM $MgCl_2$, which was expected to counteract the disruptive 2-AP substitution. Indeed, in the presence of 1 mM Mg^{2+}, $preQ_1$ addition induced a small negative shift in the CD spectrum at the same wavelengths as observed in the absence of Mg^{2+} for all other variants (Fig. 4.4c). The fluorescence data reported above show that restoration of this “native" global conformational change significantly alters how the local environment of 2-AP at position 31 changes upon ligand binding, while only modestly improving the K_{app} value (from 24,900 to 19,000 nM). This indicates that while 1 mM Mg^{2+} alters the global (based on CD) and local (based on fluorescence) conformations adopted by this variant, it is unable to compensate for the decrease in affinity induced by 2-AP substitution. In contrast, the position 29 variant maintains the same pattern of fluorescence quenching, blueshift in emission spectrum, and negative shift in CD spectrum (Fig. 4.4b) upon ligand addition regardless of whether 1 mM Mg^{2+} is present, but with a significant improvement in K_{app} in the presence of Mg^{2+}.

CD and fluorescence both indicate that 2-AP substitution at positions 31 and 32 is particularly detrimental, while substitution at position 28 is surprisingly detrimental given its distance from the ligand-binding pocket. NMR (Fig. 4.5) and x-ray crystallography structures indicate that A31 normally forms a Hoogsteen base pair with U8, which in turn makes a hydrogen bond with $preQ_1$.[9-11] Relocation of the 6-amino group of A31 through 2-AP substitution removes one of the two hydrogen bonds in this Hoogsteen base pair, destabilizing this network of interactions (Fig. 4.5b). Relocation of the 6-amino group of A32 is expected to break a hydrogen bond with $preQ_1$ (Fig. 4.5c). In the crystal structure, A32 additionally makes a Hoogsteen base pair with U9,[9] but this interaction is not observed in the NMR structure which, like our data on this variant, was recorded in the absence of divalent cations.[11]

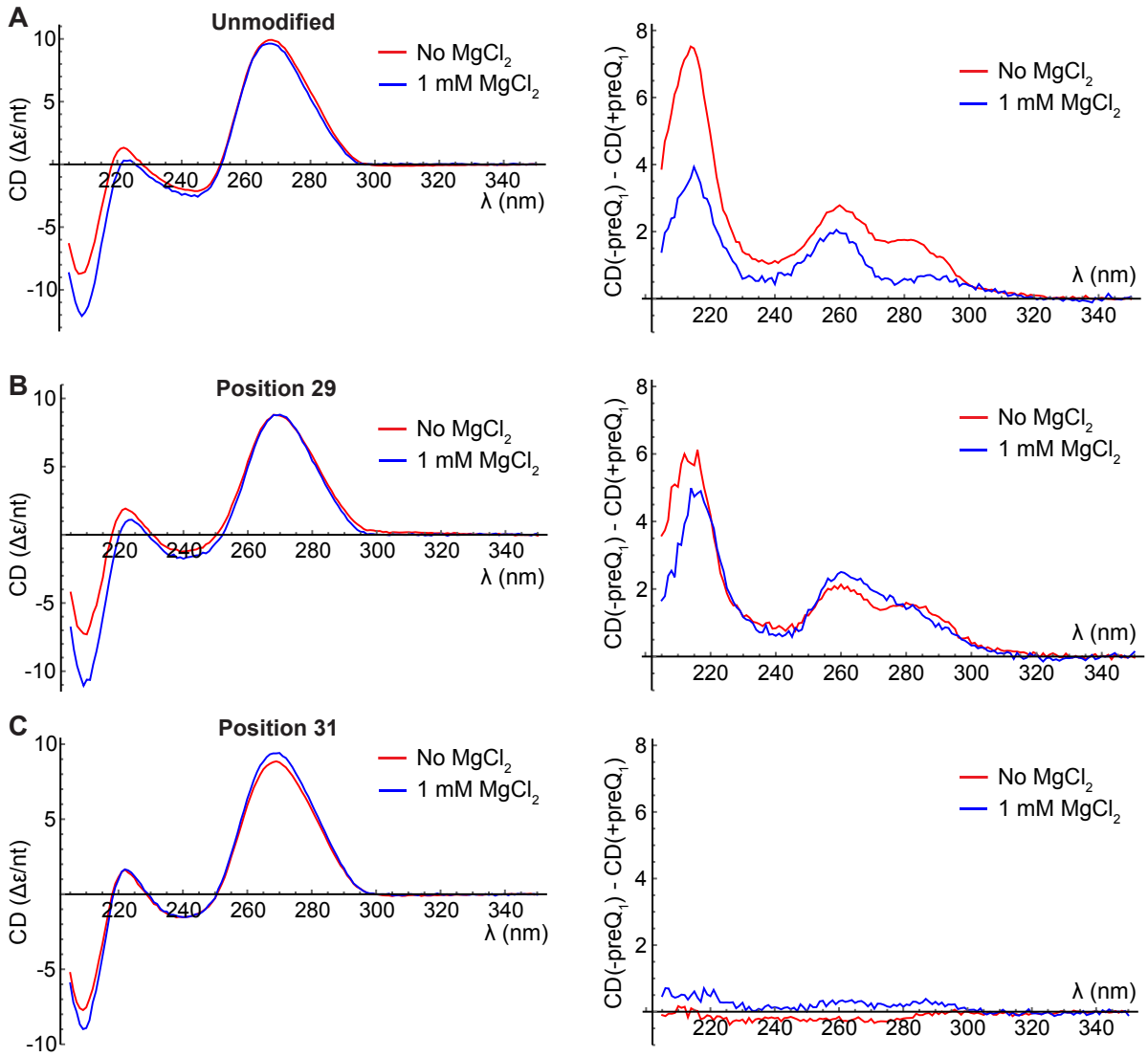

Figure 4.4 Effects of $MgCl_2$ on unmodified, position 29 and position 31 variants. Red curves are reproduced from Figure 4.3 for ease of comparison. (A) Left: CD spectra of unmodified riboswitch in the absence of $preQ_1$ and the absence (red) or presence (blue) of 1 mM $MgCl_2$. Right: CD difference spectra using 5 μM $preQ_1$ for unmodified riboswitch in the absence (red) or presence (blue) of 1 mM $MgCl_2$. (B) Corresponding plots for position 29 variant. (C) Corresponding plots for position 31 variant.

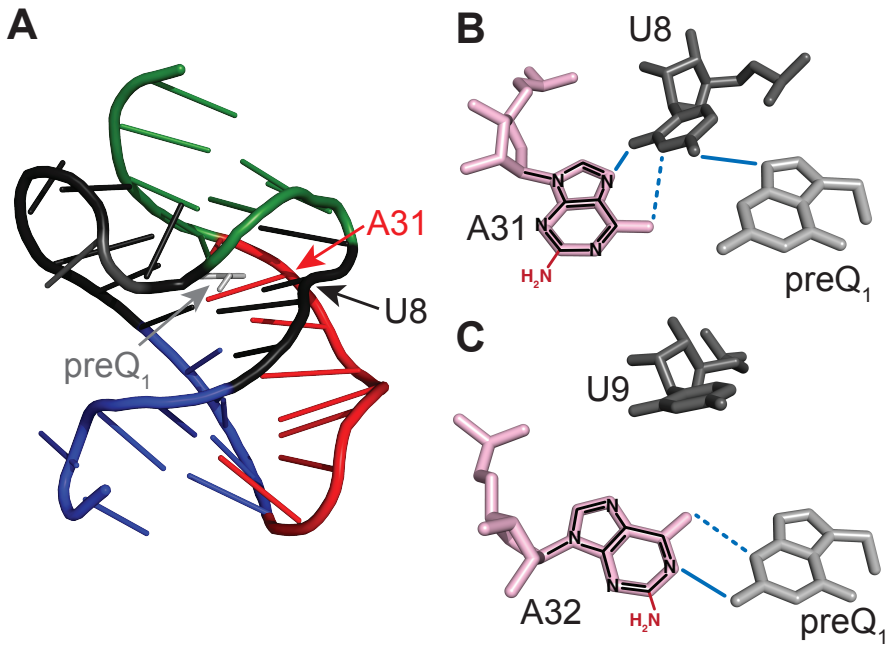

Figure 4.5 2-AP disrupts key hydrogen bonds when placed at position 31 or 32. (A) NMR structure of the riboswitch (PDB ID 2L1V) with the locations of $preQ_1$, U8 and A31 indicated. (B) Closeup of the ligand-binding pocket showing interactions between U8, A31 and $preQ_1$. Hydrogen bonds are indicated by blue lines, with dashed lines indicating bonds that are broken when A is replaced by 2-AP. (C) Closeup of the ligand binding pocket viewed from the same perspective showing interactions between A32 and $preQ_1$.

Among the labeling sites that are not immediately adjacent to the ligand-binding pocket (positions 27-30), placing 2-AP at position 28 is particularly detrimental to ligand recognition. NMR and crystal structures indicate that each A residue within L3 makes tertiary interactions with residues in P1.[9-11] However, only in A28 does the 6-amino group make hydrogen bonds with members of two different base pairs in P1: U22, which base-pairs with A5, and G6, which base-pairs with C21. Replacing A28 with 2-AP would break these bridging hydrogen bonds, whereas replacing A27, A29 or A30 with 2-AP breaks hydrogen bonds that do not bridge multiple base pairs in P1. This may explain why substitution at position 28 is more detrimental to the affinity of the riboswitch for $preQ_1$ than might be expected given its position.

Thermal denaturation experiments. To assess the effects of 2-AP substitution on the stability of the riboswitch structure, thermal denaturation measurements were performed by monitoring CD

and absorbance signals at 258 nm as the sample was heated. The melting curves of the riboswitch exhibit two transitions (Fig. 4.6). Based on its breadth and low temperature of onset, we attribute the first to the helix-to-coil transition within L3 (as observed in ref. (36) for a model oligonucleotide mimicking L3), and the higher-temperature transition to unfolding of the P1 helix. A mutant in which the P2 helix is destabilized, G13U, still exhibits two transitions, indicating that transition 1 is not related to unfolding of P2 (Fig. 4.6a). Furthermore, the oligonucleotide AA(2-AP)AC (described previously in the context of fluorescence measurements) shows a non-cooperative increase in A258 at low temperatures with a steeper slope than the unmodified or mutant riboswitches, but with a shallower slope than certain 2-AP-modified variants (Fig. 4.6b). This suggests that 2-AP substitution at certain sites destabilizes the single-stranded helical structure of L3.

In the absence of $preQ_1$, clear differences between the variants are noticeable at low temperatures and apparent when the curves are fit (Fig. 4.7 and Fig. B.7). Transition 1 occurs at $T_m = 24 \pm 2°C$ in the unmodified riboswitch and at a lower temperature in the 2-AP-modified variants, having a value of $T_m = 10.2 \pm 0.1°C$ with 2-AP at position 27. T_m 1 increases gradually as 2-AP is moved toward the ligand binding pocket to $22.3 \pm 0.4°C$ with 2-AP at position 32.

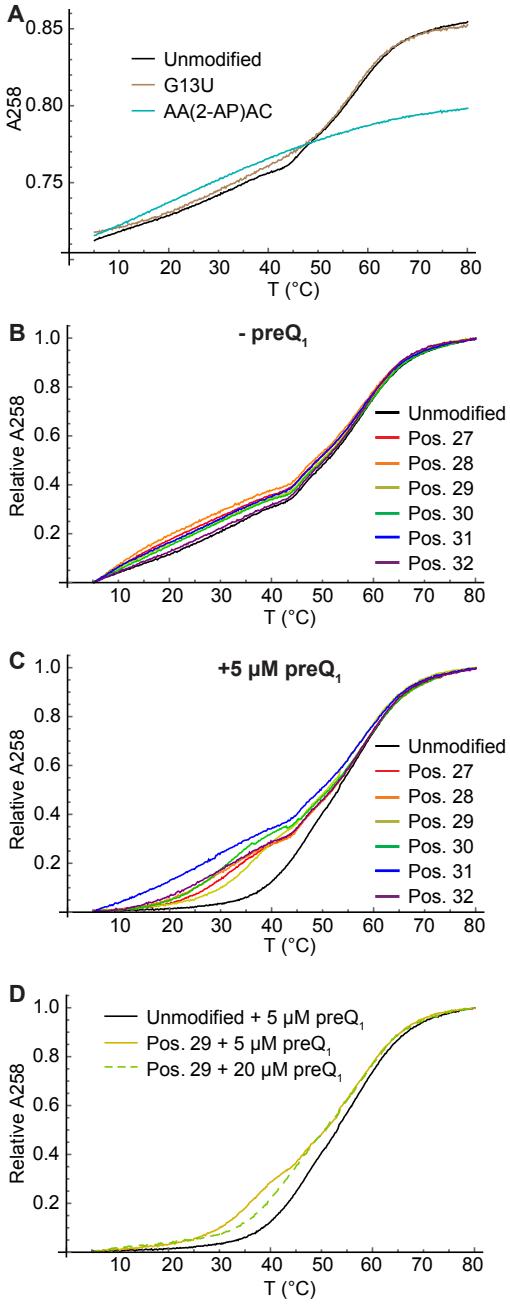

Figure 4.6 Thermal denaturation measurements. (A) Raw absorbance melting curves of unmodified riboswitch (black) and controls (G13U mutant in brown, AA(2-AP)AC in cyan). (B, C) Absorbance melting curves of unmodified and 2-AP-modified variants recorded at 258 nm in the absence (B) or presence (C) of 5 µM $preQ_1$. For ease of comparison, the curves were shifted and normalized to run from a minimum of 0 to a maximum of 1. (D) Rescaled melting curves of unmodified riboswitch (black) and position 29 variant (yellow solid) in the presence of 5 µM preQ1, and position 29 variant in the presence of 20 µM $preQ_1$ (yellow dashed).

This indicates that 2-AP disrupts L3 most significantly when it is placed near the "hinge" where the two domains adjoin, and less significantly when it is near the ligand-binding pocket. 2-AP

has little effect on T_m 2 (Fig. 4.7c), which is expected because L3 is already in a random coil conformation at that temperature.

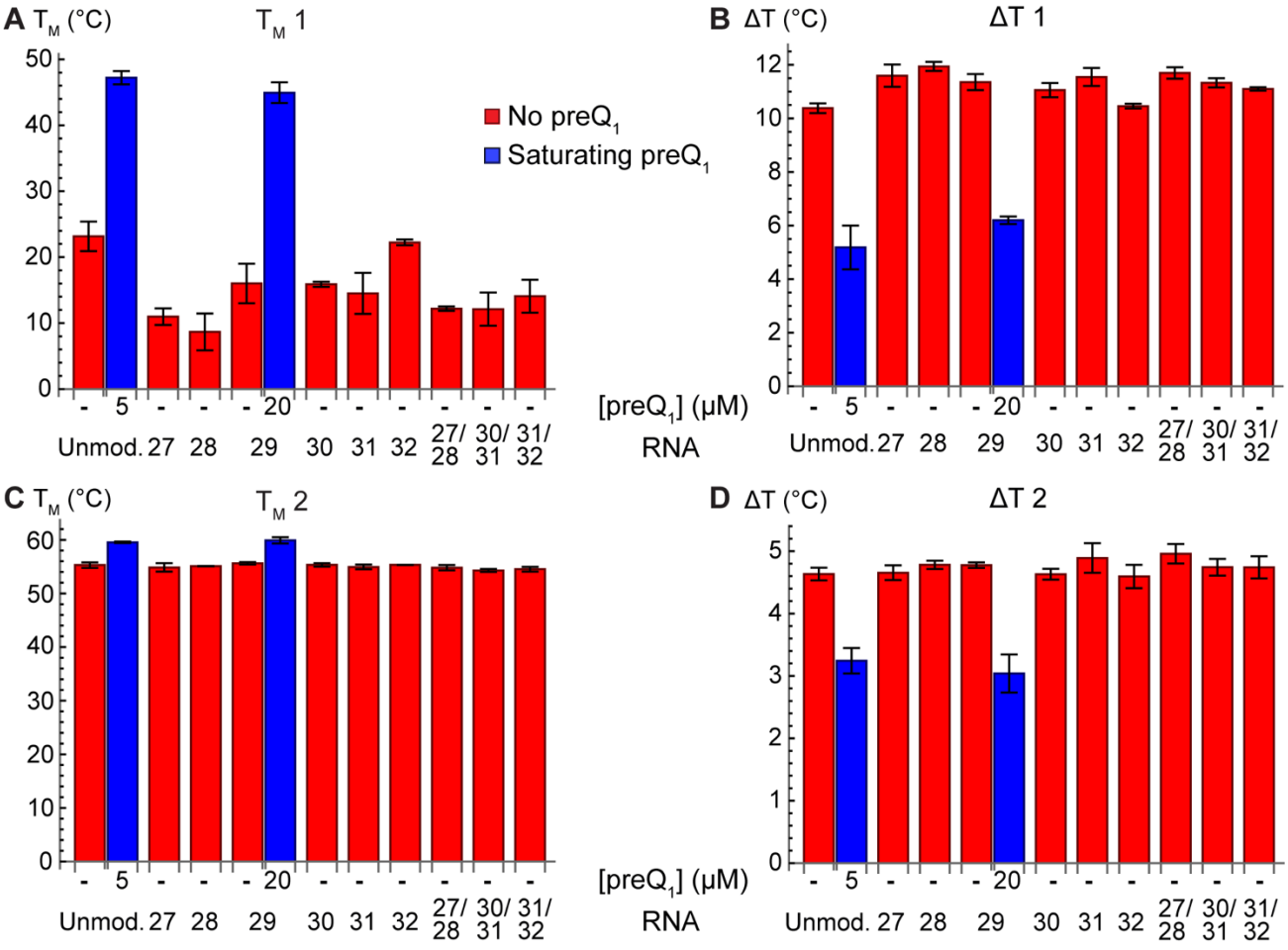

Figure 4.7 Fitting parameters extracted from absorbance melting curves. Three experimental replicates were fit individually, and the average and standard deviation of each parameter value are plotted. (A) Melting temperature of transition 1 for the unmodified riboswitch ("Unmod."), singly-labeled variants (27–32), and doubly-labeled variants (27/28, 30/31, and 31/32). Values in the presence of saturating $preQ_1$ are shown for unmodified (5 μM) and position 29 (20 μM) variants. (B) Width of transition 1. (C) Melting temperature of transition 2. (D) Width of transition 2.

When $preQ_1$ is added to the unmodified riboswitch, transition 1 shifts to a significantly higher temperature, from $T_m = 24 \pm 2°C$ to $48 \pm 1°C$; Fig. 4.6c and Fig. 4.7) and narrows from $\Delta T = 10.4 \pm 0.2°C$ to $5.6 \pm 0.6°C$. This suggests that the L3-P1 interactions that exist in the ligand-bound structure suppress the low-temperature helix-to-coil transition. The melting temperature of transition 2 changes only slightly (from $55.4 \pm 0.6°C$ to $59 \pm 1.2°C$, while its

width decreases to a smaller extent than seen for transition 1 (from 4.7 ± 0.1°C to 3.5 ± 0.1°C; Fig. 4.6c-d). Addition of saturating (20 μM) $preQ_1$ to the position 29 variant induces nearly identical changes in the fitting parameters, though transition 1 remains very slightly lower and broader than in the unmodified riboswitch (Fig. 4.6d). All other variants exhibit intermediate effects of $preQ_1$ that are consistent in magnitude with the effects seen by CD, with 5 μM $preQ_1$ inducing almost no change in the melting curves of the position 31 and 32 variants and moderate changes in the melting curves of the position 27, 28 and 30 variants. As with the CD spectra, this is due at least in part to the fact that these variants are not saturated at 5 μM $preQ_1$.

When the CD signal is monitored at 258 nm in the absence of $preQ_1$, all variants exhibit a monotonic decrease in intensity as the temperature is increased, as expected. In the presence of $preQ_1$, all variants except for position 31 exhibit an increase in CD intensity, followed by a decrease starting around 45 °C (Fig. B8). To investigate this surprising observation, we recorded CD spectra at different temperatures during thermal ramping. We observed that in the presence of $preQ_1$, the lineshape of the CD spectrum changes with temperature in a manner that leads to a transient increase in CD intensity at 258 nm, while the overall intensity of the spectrum decreases monotonically. As a result, the CD signal at 258 nm is not a simple reflection of the fraction of RNA still folded. Above a temperature of 40 °C, the spectra recorded in the absence and presence of $preQ_1$ no longer differ from one another, suggesting that ligand dissociation happens around this temperature.

Multiple 2-AP labeling sites. We next investigated whether replacement of multiple A residues with 2-AP would have an additive or cooperative effect on riboswitch folding. We recorded CD spectra and melting curves on variants with 2-AP placed at positions 27 *and* 28, or positions 30 *and* 31, or positions 31 *and* 32 (Fig. B9). In general, a second 2-AP substitution had little impact

beyond the more influential of the two single substitutions. For example, the CD spectrum of the position 27 variant exhibits a strong response to 5 μM $preQ_1$, while the position 28 variant exhibits a moderate response. When 2-AP is placed at both positions, the response is nearly identical to what is observed in the position 28 variant (Fig. B9a). The same observation is noted when comparing melting curves of singly- and doubly-labeled variants. In the absence of $preQ_1$, the absorbance melting curve of each doubly-labeled variant is indistinguishable by eye from that of the more influential singly-labeled variant (Fig. B9d-f), and fitting of the melting curves supports this observation (Fig. 4.6). A slight additional impact of the second 2-AP residue is observed in melting curves recorded in the presence of 5 μM $preQ_1$ (Fig. B9g-i).

Conclusions

The work presented here comprises a systematic study of the structural changes in the A-rich tail of the $preQ_1$ riboswitch that occur upon ligand binding, and how chemical modifications within this domain impact the structure and stability of the riboswitch. The significant impairment of ligand affinity by 2-AP substitution shows that strong ligand binding is dependent on interactions involving the 6-amino group of every A residue in L3. While L3 behaves essentially as a single-stranded RNA in the absence of $preQ_1$, ligand binding redistributes the A residues within it between local environments with variable base-stacking and polarity. This work shows that the interactions between L3 and P1 observed in structural studies are critical to high-affinity ligand binding, and that valuable information can be obtained by using FBAs to simultaneously probe and perturb RNA structure.

ACKNOWLEDGMENTS*:* This work has been supported in part by NIH R00 GM120457.

CHAPTER V

CONCLUSIONS

CD, FDCD and fluorescence spectroscopy are useful techniques to study RNA structure and function. Using these methods, the work reported in this thesis uncovered nuances of the structure-photophysics relationships of the widely used fluorescent adenine analogue 2-AP, and utilized it as a probe to study the structural factors underlying ligand binding by the $preQ_1$ riboswitch. 2-AP, while a useful tool to study RNA structure, can act as a mutation that impacts the structure. For example, inserting 2-AP into the $preQ_1$ riboswitch greatly weakened its affinity for its ligand. While most studies have used 2-AP in locations chosen to not disrupt the structure, moving forward it can be placed in locations specifically chosen to disrupt the structure. A small difference in structure can impact function and ligand binding, particularly at locations with high sequence conservation. A FBA's ability to disrupt the structure and function should be kept in mind when utilizing them in all forms of RNA. Whether or not they impact the structure of a given RNA of interest, 2-AP and other FBAs are useful in studying RNA structure. As seen in the $preQ_1$ riboswitch, nucleotides separated by one or two positions from each other can respond to ligand binding in distinct ways.

FBAs that are analogues of other bases besides adenine can help to understand folding in other sequence contexts, and adenine analogues besides 2-AP can be used to report on different aspects of local RNA structure. Different FBAs could behave differently due to their different structures, acting as different mutations than 2-AP to selectively disrupt structure or function to varying extents. While intentionally disrupting the structure of RNA can be useful, having a

FBA that doesn't disrupt the structure would also be of interest. Analogues of native bases other than adenine would also allow for the study of different locations in RNA.

The FDCD results presented here help to develop our understanding on the impact of 2-AP stacking on its fluorescence properties. This work adds important structural context to the base-stacking heterogeneity that in the past has primarily been analyzed through fluorescence lifetime measurements. While the ~9-10 ns lifetime observed in dinucleotides and in the $preQ_1$ riboswitch is coming from an extra helical conformation of 2-AP, our work showed that lifetime components of 1-4 ns come from populations that are likely significantly unstacked as well. For example, in the dinucleotide C(2-AP), the subpopulation with a ~2 ns lifetime contributes ~75% of the fluorescence and is thus the most prominent contributor to the FDCD spectrum. With the converted FDCD spectrum looking like that of a nucleoside, this means that this population's structure may have more in common with the solvent-exposed extrahelical conformation than with the stacked structures that are typically considered to give rise to short lifetimes. The work described here helped to uncover the photophysics of the most common FBA and helps lay a path for determining the structure-photophysics relationships of other FBAs as well.

In the future, the work reported here will form the foundation for application of FDCD to more complex systems than trinucleotides. In particular, it could be useful in studying how the conformations of specific nucleotides change when a riboswitch binds to its ligand. In addition, knowing how 2-AP impacts the structure of a small 38-nucleotide RNA will help to interpret data obtained with it in more complex, larger RNA systems such as other riboswitches. Using 2-AP as a mutation could help with identifying functionally significant regions in riboswitches to target with antibacterial drugs. In conclusion, the work reported in this thesis lays the foundation

for future experiments that use information-rich spectroscopic techniques to probe the structures a broad range of RNA systems using a broad range of fluorescent probes.

APPENDIX A

SUPPLEMENTAL INFORMATION FOR BASE-STACKING HETEROGENEITY

The contents of this chapter have been previously published in whole or in part. The text present here has been modified from the publication below:

Widom, J. R.; Hoeher, J. E. Base-Stacking Heterogeneity in RNA Resolved by Fluorescence-Detected Circular Dichroism Spectroscopy. *J. Phys. Chem. Lett.* **2022**, *13* (34), 8010–8018. https://doi.org/10.1021/acs.jpclett.2c01778.

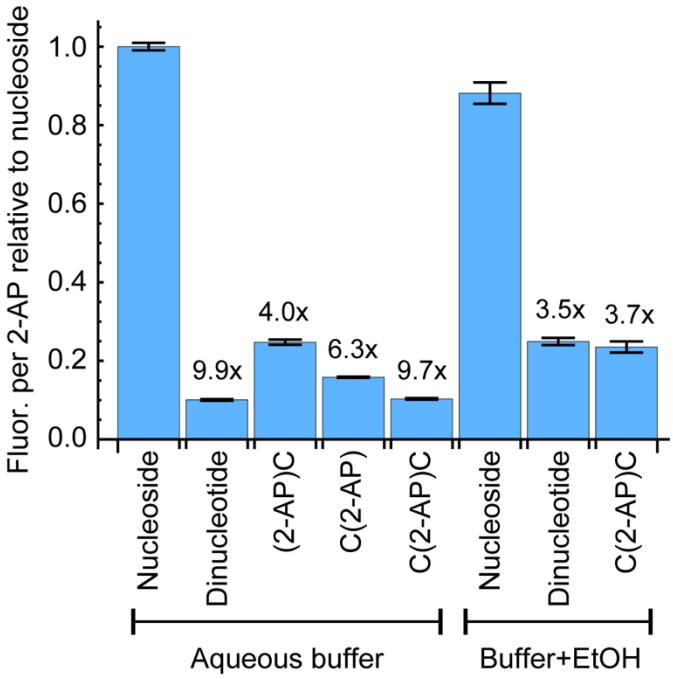

Figure A1. Fluorescence intensities of all samples used in this study, determined from emission spectra recorded under excitation at 295 nm. Intensities per unit 2-AP absorbance were determined and then normalized to the intensity of free 2-AP riboside in aqueous buffer. Error bars are the standard deviation of measurements on three independently prepared samples. Numbers above the bars are the factors by which 2-AP fluorescence is quenched relative to the free nucleoside in the same solvent.

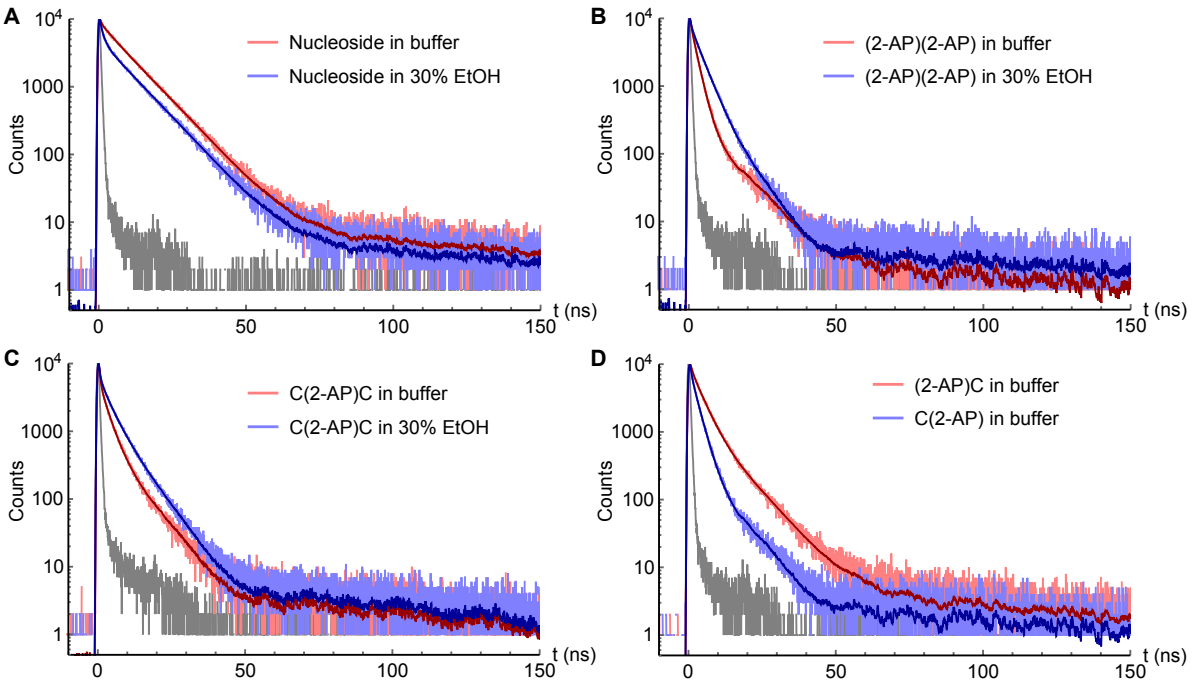

Figure A2. TCSPC data and fits. Gray: instrument response function; Light red and blue: data; Dark red and blue: fits. (A) 2-AP riboside in buffer (red) and buffer containing 30% v/v ethanol (blue). (B) 2-AP dinucleotide in buffer (red) and buffer containing 30% ethanol (blue). (C) C(2-AP)C in buffer (red) and buffer containing 30% ethanol (blue). (D) (2-AP)C in buffer (red) and C(2-AP) in buffer (blue).

Sample	Solvent	α_1 (%)	τ_1 (ns)	α_2	τ_2	α_3	τ_3
Nucleoside	B	7.3	0.08	2.6	2.58	90.1	9.37
Nucleoside	B+E	13.1	0.08	9.5	1.25	77.4	9.28
(2-AP)(2-AP)	B	19.9	0.16	70.2	2.03	9.9	9.46
(2-AP)(2-AP)	B+E	19.2	0.08	66.8	3.55	14.0	7.05
(2-AP)C	B	8.8	0.29	62.9	3.65	28.3	9.49
C(2-AP)	B	19.9	0.23	71.2	2.43	8.9	8.35
C(2-AP)C	B	30.2	0.16	46.2	2.59	23.6	7.11
C(2-AP)C	B+E	21.8	0.10	26.7	2.77	51.5	6.36

Table A1. Fitting parameter values obtained from TCSPC data. Lifetimes highlighted in red are shorter than the FWHM of the IRF by a factor of 5 or more. These components were thus considered unreliable and were subsumed into the "dark" population α_0 in Table 1. "B": Aqueous buffer. "B+E": Buffer containing 30% ethanol.

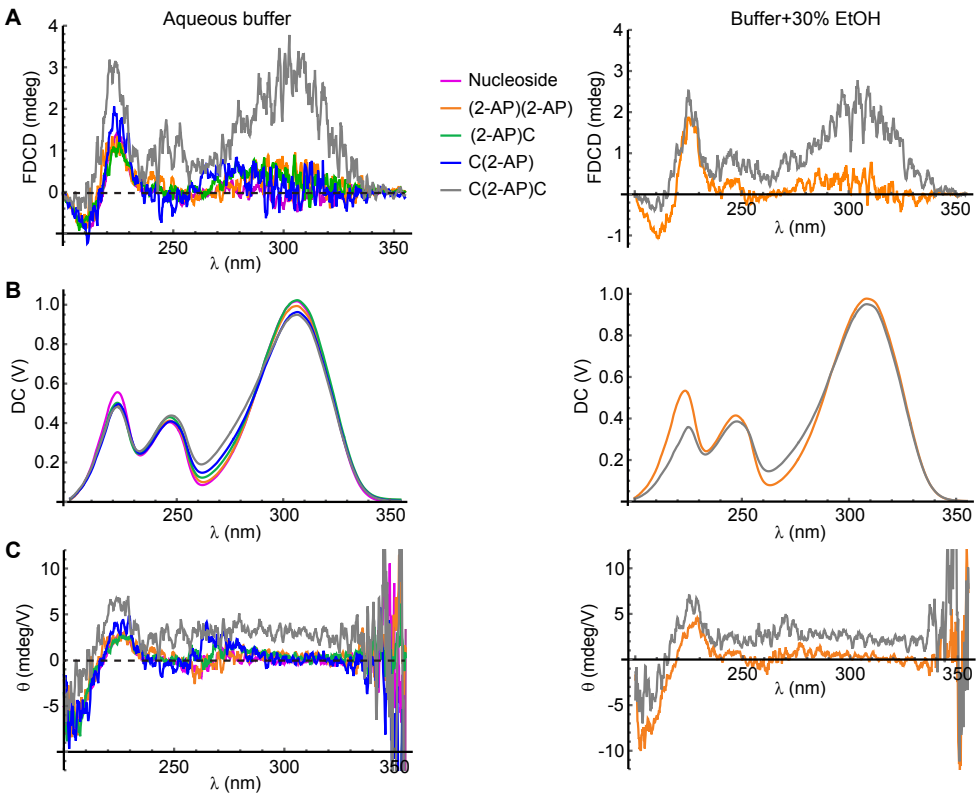

Figure A3. Unprocessed FDCD data. Spectra on the left were recorded in aqueous phosphate buffer and spectra on the right were recorded in buffer containing 30% v/v ethanol. (A) The "FDCD" readout from the instrument after baseline correction using 2-AP nucleobase. This signal is proportional to the difference in fluorescence intensity observed under excitation with left- and right-handed circularly polarized light. (B) The "DC" readout from the instrument after baseline correction using solvent. This signal is proportional to the sum of the intensities observed under excitation with left- and right-handed circularly polarized light. (C) θ = FDCD/DC is the input for processing the FDCD data using the equations in the main text.

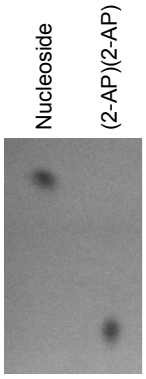

Figure A4. Thin-layer chromatography shows that the 2-AP nucleoside and (2-AP)(2-AP) samples are chemically pure.

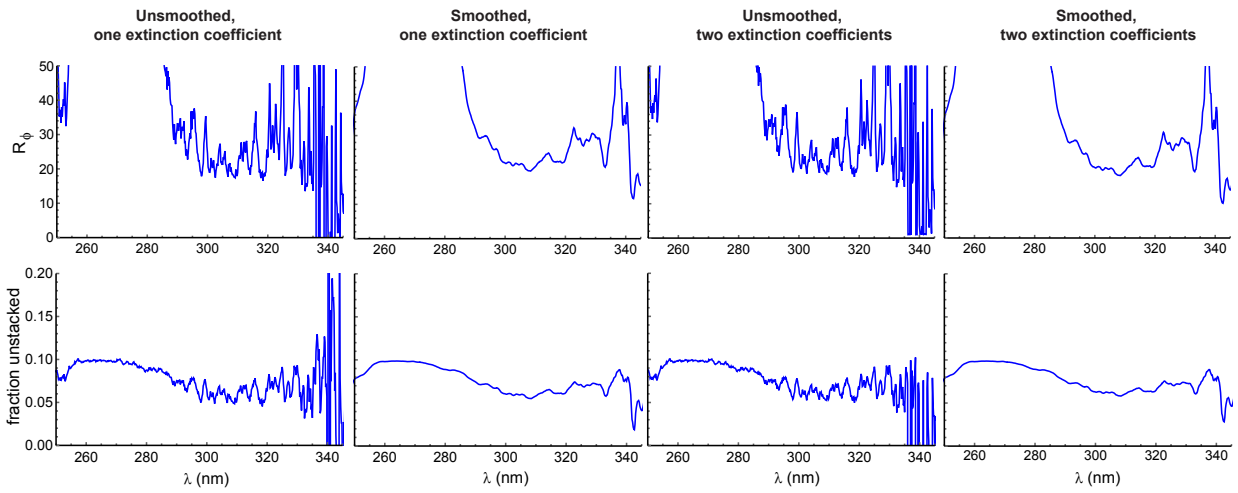

Figure A5. Plots of the quenching ratio R_ϕ (top) and fraction unstacked f_{un} (bottom) obtained for C(2-AP)C samples in aqueous buffer under different model parameters. Results are quantified in Table 3.2.

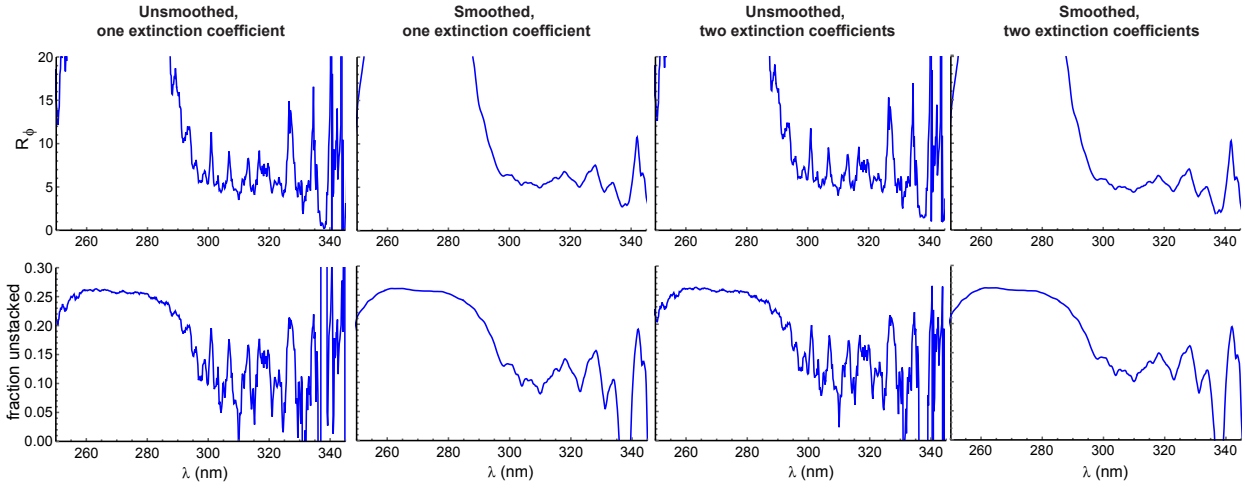

Figure A6. Plots of the quenching ratio R_ϕ (top) and fraction unstacked f_{un} (bottom) obtained for C(2-AP)C samples in buffer containing 30% ethanol under different model parameters. Results are quantified in Table 2.

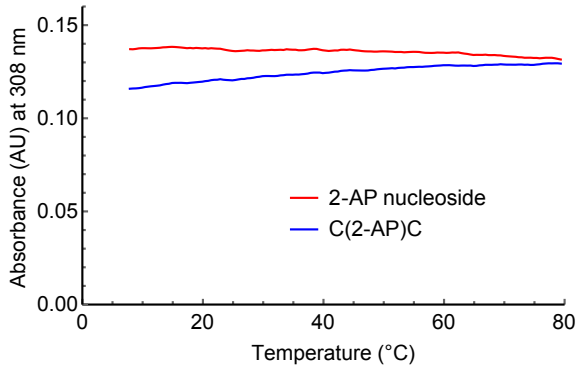

Figure A7. Thermal ramp monitoring absorbance by 2-AP nucleoside and C(2-AP)C at 308 nm.

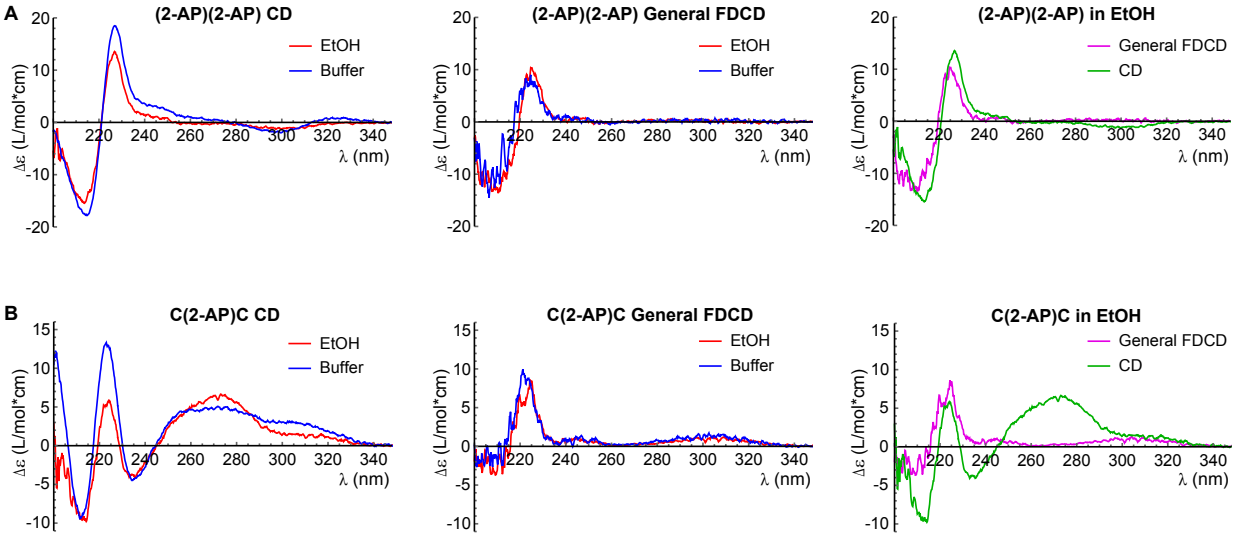

Figure A8. Comparison of spectra recorded in buffer (blue) and buffer+30% ethanol (red) for (A) (2-AP)(2-AP) and (B) C(2-AP)C. Left: Standard CD spectra. Middle: FDCD spectra processed with equation 2. Right: Comparison of FDCD (magenta) and CD (green) spectra for samples in 30% ethanol.

APPENDIX B

SUPPLEMENTAL INFORMATION FOR PROBING AND PERTURBING

The contents of this chapter have been previously published in whole or in part. The text present here has been modified from the publication below:

Hoeher, J. E.; Sande, N. E.; Widom, J. R. Probing and Perturbing Riboswitch Folding Using a Fluorescent Base Analogue. *Photochem. Photobiol. n/a* (n/a). https://doi.org/10.1111/php.13896.

Unmodified	5’ GCA GAG GUU CUA GCU ACA | CCC UCU AUA AAA AAC UAA GG
Position 27	5’ GCA GAG GUU CUA GCU ACA | CCC UCU AU**(2-AP)** AAA AAC UAA GG
Position 28	5’ GCA GAG GUU CUA GCU ACA | CCC UCU AUA **(2-AP)**AA AAC UAA GG
Position 29	5’ GCA GAG GUU CUA GCU ACA | CCC UCU AUA A**(2-AP)**A AAC UAA GG
Position 30	5’ GCA GAG GUU CUA GCU ACA | CCC UCU AUA AA**(2-AP)** AAC UAA GG
Position 31	5’ GCA GAG GUU CUA GCU ACA | CCC UCU AUA AAA **(2-AP)**AC UAA GG
Position 32	5’ GCA GAG GUU CUA GCU ACA | CCC UCU AUA AAA A**(2-AP)**C UAA GG
Position 27/28	5’ GCA GAG GUU CUA GCU ACA | CCC UCU AU**(2-AP) (2-AP)**AA AAC UAA GG
Position 30/31	5’ GCA GAG GUU CUA GCU ACA | CCC UCU AUA AA**(2-AP) (2-AP)**AC UAA GG
Position 31/32	5’ GCA GAG GUU CUA GCU ACA | CCC UCU AUA AAA **(2-AP)(2-AP)**C UAA GG
G13U	5’ GCA GAG GUU CUA **U**CU ACA | CCC UCU AUA AAA AAC UAA GG
Control oligo	5’ AA**(2-AP)**AC
DNA splint	5’ GTT TTT TAT AGA GGG TGT AGC TAG AAC C

Table B1. Sequences of oligonucleotides used in this work. Bold text highlights the positions of 2-AP substitutions or mutations. Vertical lines indicate the division between the 5’ and 3’ segments that were ligated together. Each 3’ segment was purchased with a phosphate group at its 5’ end to enable ligation.

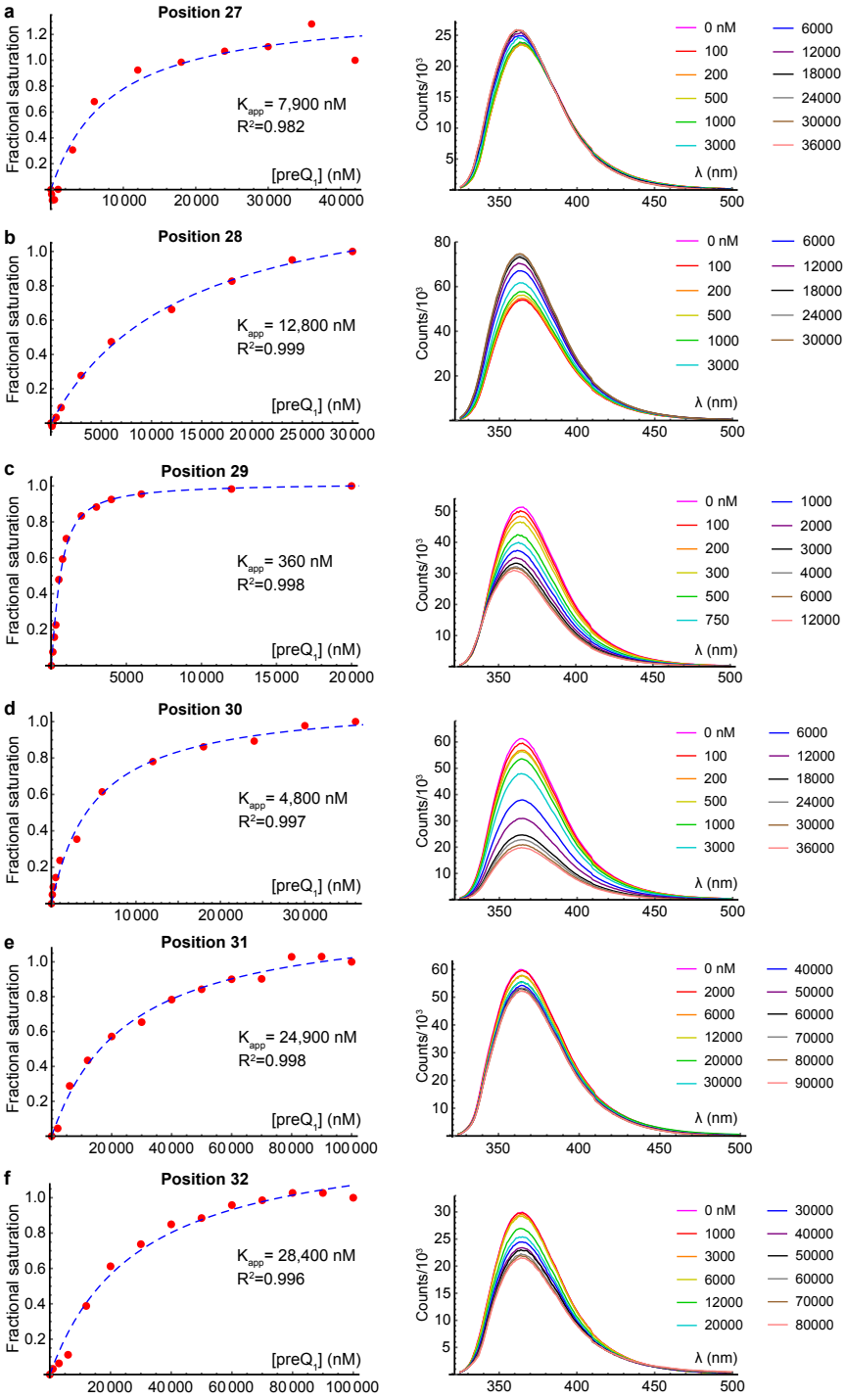

Figure B1. Fluorescence titrations on 2-AP-modified variants recorded in the absence of $MgCl_2$. (a) Position 27. (b) Position 28. (c) Position 29. (d) Position 30. (e) Position 31. (f) Position 32. Left: fractional saturation based on peak intensity (red markers), and fit (dashed blue line). The apparent K_D and R^2 for the fit are indicated in each plot. Fractional saturation datapoints were computed using the average of three replicates performed on separately prepared samples. Right: Example titration for each variant. A maximum of 12 spectra are shown.

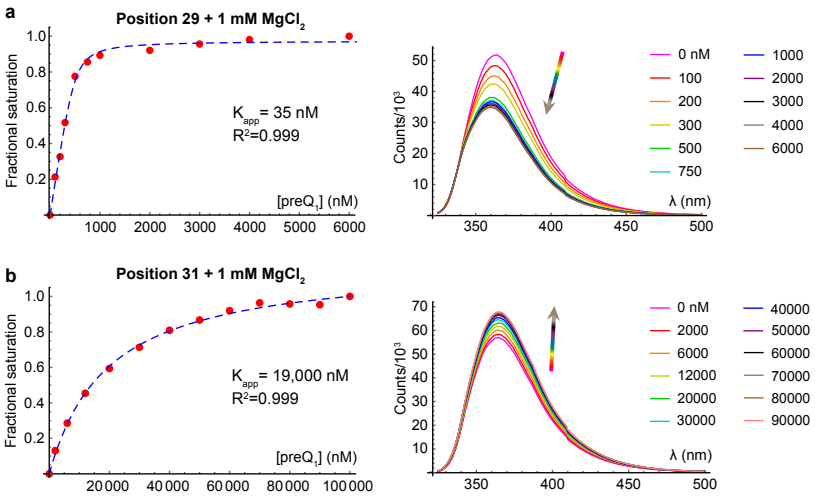

Figure B2. Fluorescence titrations on select 2-AP-modified variants recorded in the presence of 1 mM $MgCl_2$. (a) Position 29. (b) Position 31. Left: fractional saturation based on peak intensity (red markers), and fit (dashed blue line). The apparent K_D and R^2 for the fit are indicated in each plot. Fractional saturation datapoints were computed using the average of three replicates performed on separately prepared samples. Right: Example titration for each variant. A maximum of 12 spectra are shown.

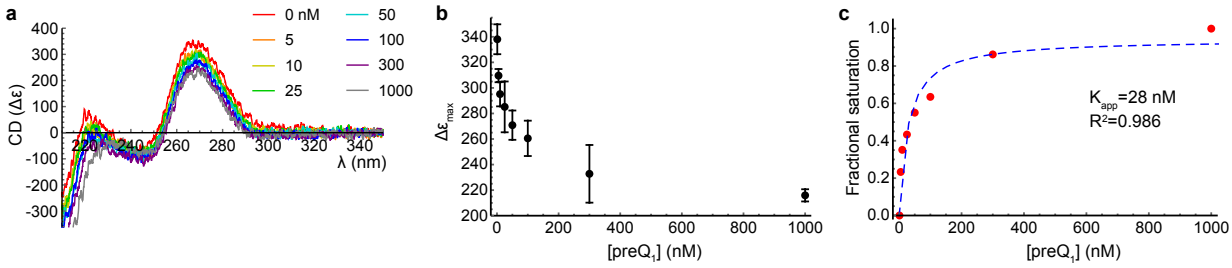

Figure B3. CD titration on unmodified riboswitch. (a) CD spectra of 50 nM unmodified riboswitch at varying $preQ_1$ concentrations. (b) Quantification of maximum CD signal at each $preQ_1$ concentration. The average and standard deviation of measurements on three separately prepared samples are shown. (c) Fractional saturation (red markers) and fit (blue dashed line) determined from the data in panel b.

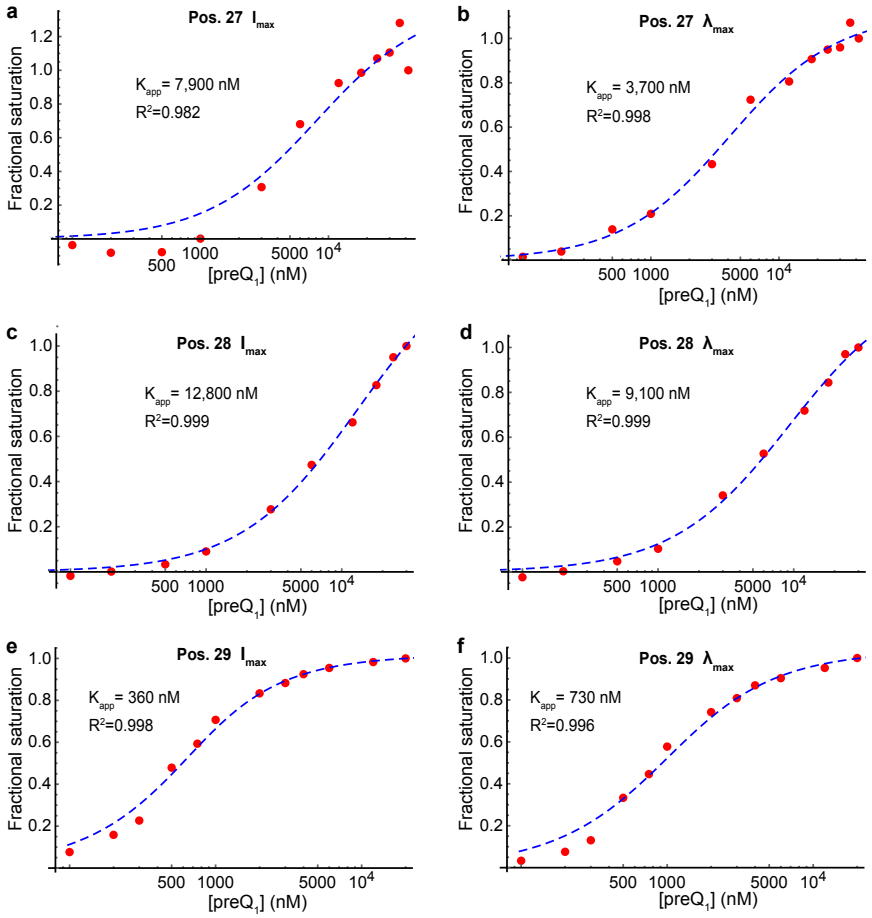

Figure B4. Comparison of fluorescence titrations based on peak intensity and peak wavelength. All plots have the x-axis on a log scale to better visualize low-concentration datapoints. (a-b) Fractional saturation vs. [preQ$_1$] (red markers) based on peak intensity (a) or peak wavelength (b), and associated fits (blue dashed lines) for position 27 variant. Apparent K_D and R^2 for the fits are shown. Note the drastically improved fit in panel b. (c-d) Fractional saturation vs. [preQ$_1$] based on peak intensity (c) or peak wavelength (d) and associated fits for position 28. (e-f) Fractional saturation vs. [preQ$_1$] based on peak intensity (e) or peak wavelength (f) and associated fits for position 29.

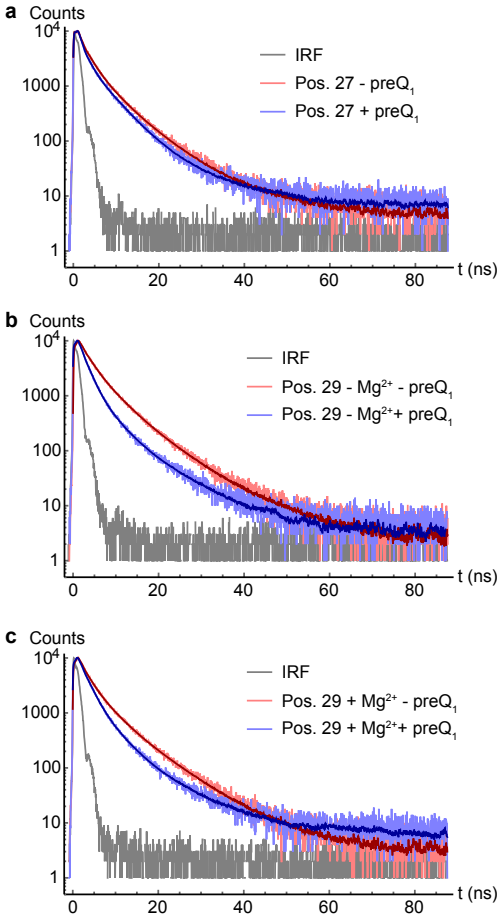

Figure B5. TCSPC measurements. (a) Position 27 variant with and without 42 µM $preQ_1$. (b) Position 29 variant with and without 20 µM $preQ_1$. (c) Position 29 variant with 1 mM $MgCl_2$ with and without 20 µM $preQ_1$. In all panels, gray: instrument response function; red: no $preQ_1$; blue: saturating $preQ_1$.

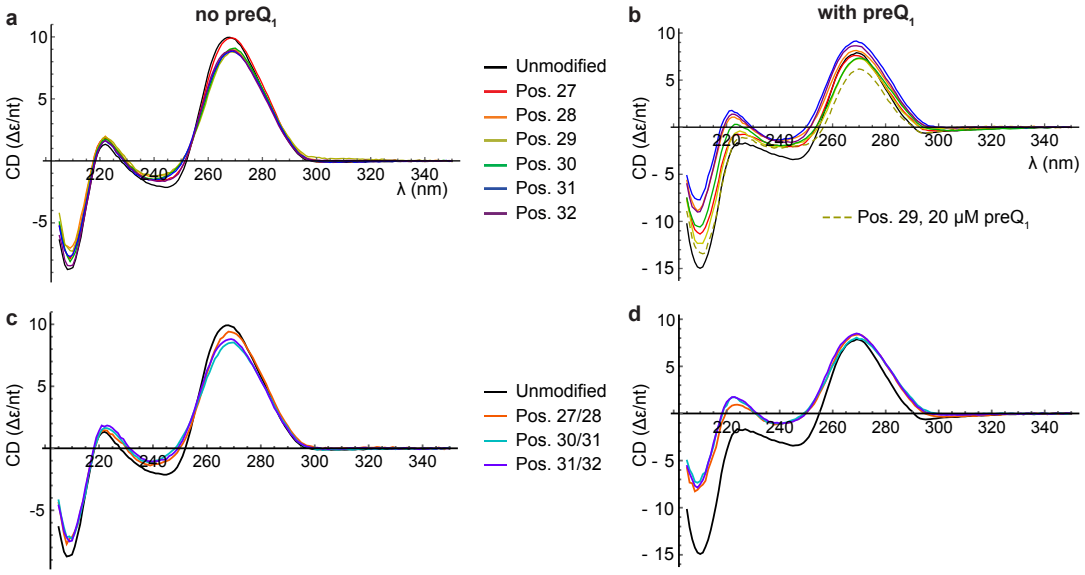

Figure B6. (a-b) CD spectra of unmodified and singly-labeled variants in the absence (a) or presence (b) of 5 μM $preQ_1$. Panel b additionally shows the spectrum of the position 29 variant in the presence of 20 μM $preQ_1$. (c-d): CD spectra of unmodified and doubly-labeled variants in the absence (c) or presence (d) of 5 μM $preQ_1$. These spectra were used to construct the difference spectra shown in Fig. 4.3 and Fig. B7.

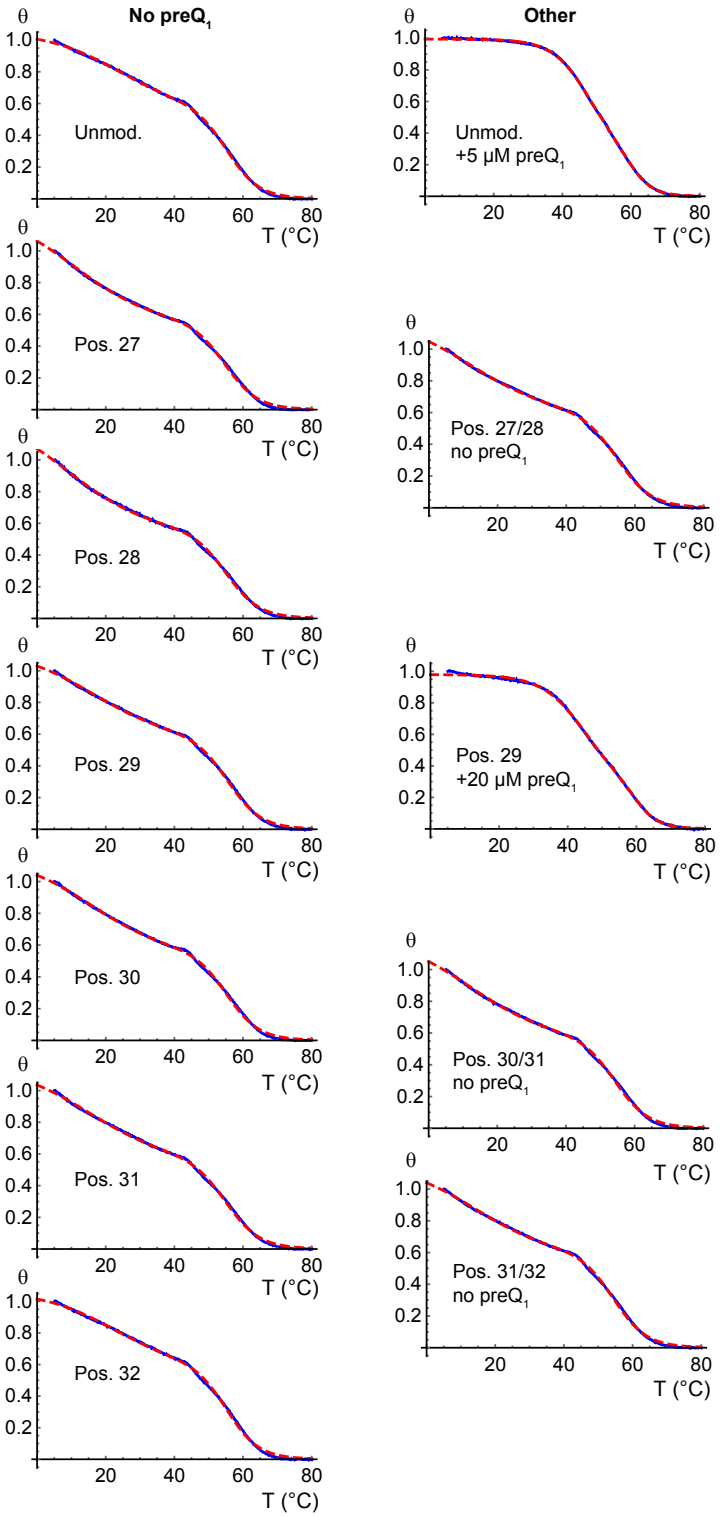

Figure B7. Processed melting curves (blue) and fits (dashed red) for one replicate plotted as θ (see methods) vs. T. The left column contains curves recorded on unmodified and singly-labeled riboswitch variants in the absence of $preQ_1$, and the right column contains other variants and $preQ_1$ concentrations as indicated on the plots.

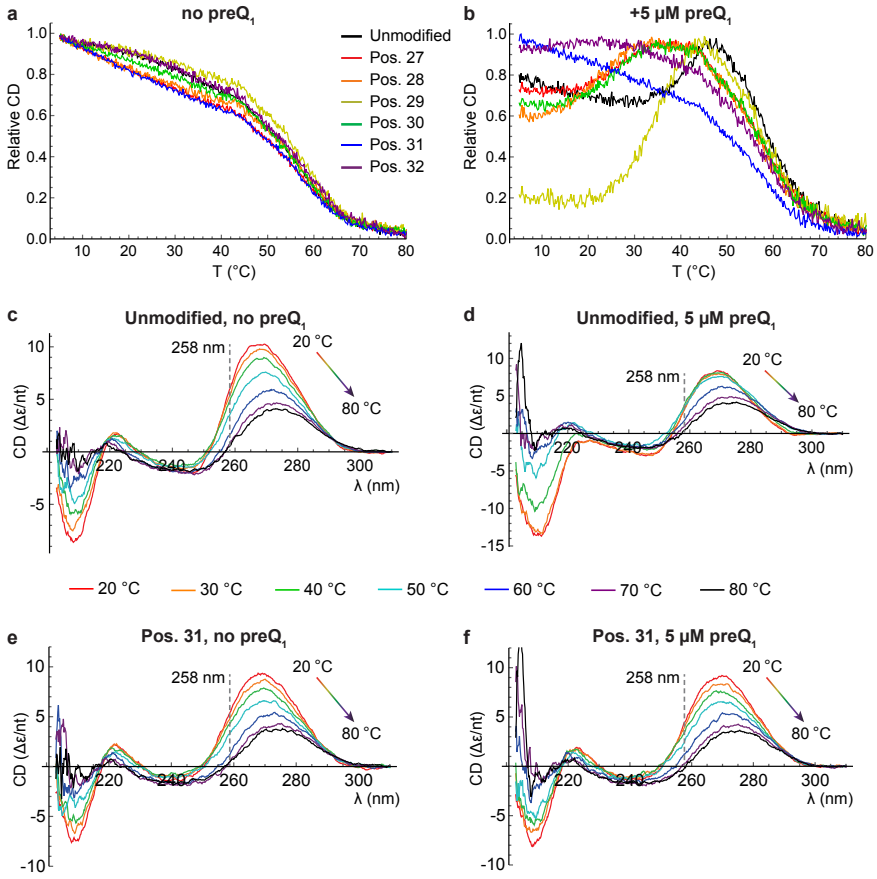

Figure B8. CD melting curves of unmodified and singly-labeled variants recorded at 258 nm in the absence (a) or presence (b) of 5 µM preQ1. For ease of comparison, the curves were shifted and normalized to run from a minimum of 0 to a maximum of 1. (c-f) CD spectra recorded during thermal ramping at 20 (red), 30 (orange), 40 (green), 50 (cyan), 60 (blue), 70 (purple) and 80 (black) °C. The wavelength at which the CD was monitored while recording melting curves is indicated by a dashed line. (c) Unmodified riboswitch in the absence of preQ1. (d) Unmodified riboswitch in the presence of 5 µM preQ1. (e) Position 31 variant in the absence of preQ1. (f) Position 31 variant in the presence of 5 µM preQ1.

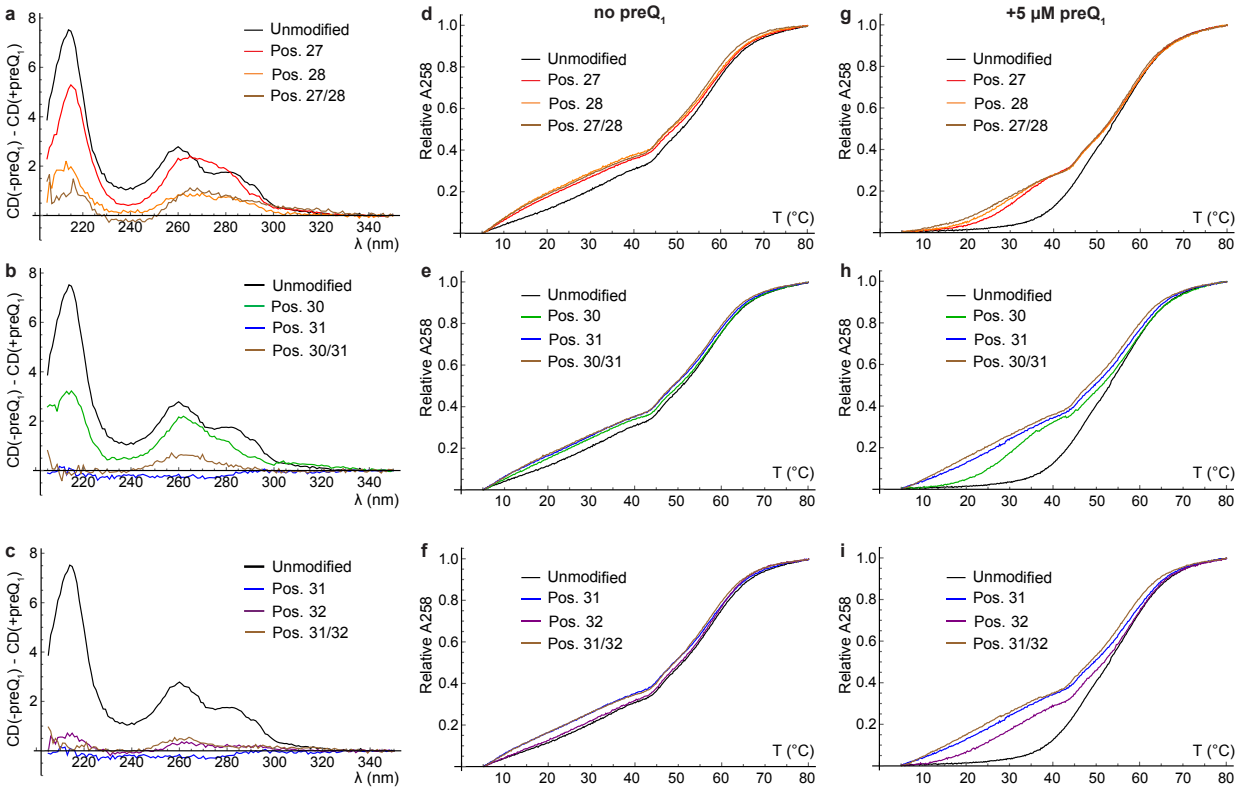

Figure B9. CD and thermal denaturation analysis of doubly-labeled variants. (a) CD difference spectra for unmodified, position 27, position 28, and position 27/28 variants. (b) Corresponding plots for positions 30 and 31. (c) Corresponding plots for positions 31 and 32. (d-f) Melting curves for unmodified, singly-labeled and doubly-labeled variants in the absence of $preQ_1$ (d) Positions 27 and 28. (e) Positions 30 and 31. (f) Positions 31 and 32. (g-i) Corresponding melting curves in the presence of 5 µM $preQ_1$. For ease of comparison, the melting curves were shifted and normalized to run from a minimum of 0 to a maximum of 1.

REFERENCES CITED

CHAPTER I-II: Introduction and Methods

(1) Cech, T. R.; Steitz, J. A. The Noncoding RNA Revolution—Trashing Old Rules to Forge New Ones. *Cell* **2014**, *157* (1), 77–94. https://doi.org/10.1016/j.cell.2014.03.008.

(2) Pitchiaya, S.; Heinicke, L. A.; Custer, T. C.; Walter, N. G. Single Molecule Fluorescence Approaches Shed Light on Intracellular RNAs. *Chem. Rev.* **2014**, *114* (6), 3224–3265. https://doi.org/10.1021/cr400496q.

(3) *Thoughts on how to think (and talk) about RNA structure*. https://doi.org/10.1073/pnas.2112677119.

(4) Assmann, S. M.; Chou, H.-L.; Bevilacqua, P. C. Rock, Scissors, Paper: How RNA Structure Informs Function. *Plant Cell* **2023**, *35* (6), 1671–1707. https://doi.org/10.1093/plcell/koad026.

(5) Misra, V. K.; Draper, D. E. On the Role of Magnesium Ions in RNA Stability. *Biopolymers* **1998**, *48* (2–3), 113–135. https://doi.org/10.1002/(SICI)1097-0282(1998)48:2<113::AID-BIP3>3.0.CO;2-Y.

(6) Saito, Y.; Hudson, R. H. E. Base-Modified Fluorescent Purine Nucleosides and Nucleotides for Use in Oligonucleotide Probes. *J. Photochem. Photobiol. C Photochem. Rev.* **2018**, *36*, 48–73. https://doi.org/10.1016/j.jphotochemrev.2018.07.001.

(7) Michel, B. Y.; Dziuba, D.; Benhida, R.; Demchenko, A. P.; Burger, A. Probing of Nucleic Acid Structures, Dynamics, and Interactions With Environment-Sensitive Fluorescent Labels. *Front. Chem.* **2020**, *8*.

(8) Ali, Z.; Goyal, A.; Jhunjhunwala, A.; Mitra, A.; Trant, J. F.; Sharma, P. Structural and Energetic Features of Base–Base Stacking Contacts in RNA. *J. Chem. Inf. Model.* **2023**, *63* (2), 655–669. https://doi.org/10.1021/acs.jcim.2c01116.

(9) Holz, B.; Klimasauskas, S.; Serva, S.; Weinhold, E. 2-Aminopurine as a Fluorescent Probe for DNA Base Flipping by Methyltransferases. *Nucleic Acids Res.* **1998**, *26* (4), 1076–1083.

(10) Somsen, O. J. G.; Hoek, van A.; Amerongen, van H. Fluorescence Quenching of 2-Aminopurine in Dinucleotides. *Chem. Phys. Lett.* **2005**, *402* (1), 61–65. https://doi.org/10.1016/j.cplett.2004.11.122.

(11) *Adenine and 2-aminopurine: Paradigms of modern theoretical photochemistry*. https://doi.org/10.1073/pnas.0602991103.

(12) Jean, J. M.; Hall, K. B. 2-Aminopurine Fluorescence Quenching and Lifetimes: Role of Base Stacking. *Proc. Natl. Acad. Sci.* **2001**, *98* (1), 37–41. https://doi.org/10.1073/pnas.98.1.37.

(13) Rachofsky, E. L.; Osman, R.; Ross, J. B. A. Probing Structure and Dynamics of DNA with 2-Aminopurine: Effects of Local Environment on Fluorescence. *Biochemistry* **2001**, *40*, 946–956. https://doi.org/10.1021/bi001664o.

(14) Frederiksen, S. Effect of 2-Aminopurine and 2-Aminopurine 2′-Deoxyriboside on Nucleic Acid Synthesis in Ehrlich Ascites Cells in Vitro. *Biochem. Pharmacol.* **1965**, *14* (5), 651–660. https://doi.org/10.1016/0006-2952(65)90083-3.

(15) A. Larsen, O. F.; Stokkum, I. H. M. van; Weerd, F. L. de; Vengris, M.; T. Aravindakumar, C.; Grondelle, R. van; E. Geacintov, N.; Amerongen, H. van. Ultrafast Transient-Absorption and Steady-State Fluorescence Measurements on 2-Aminopurine Substituted Dinucleotides and 2-Aminopurine Substituted DNA Duplexes. *Phys. Chem. Chem. Phys.* **2004**, *6* (1), 154–160. https://doi.org/10.1039/B308992D.

(16) Paterson, K. A.; Arlt, J.; Jones, A. C. Dynamic and Static Quenching of 2-Aminopurine Fluorescence by the Natural DNA Nucleotides in Solution. *Methods Appl. Fluoresc.* **2020**, *8* (2), 025002. https://doi.org/10.1088/2050-6120/ab71c3.

(17) Widom, J. R.; Hoeher, J. E. Base-Stacking Heterogeneity in RNA Resolved by Fluorescence-Detected Circular Dichroism Spectroscopy. *J. Phys. Chem. Lett.* **2022**, *13* (34), 8010–8018. https://doi.org/10.1021/acs.jpclett.2c01778.

(18) Jahnke, K.; Grubmüller, H.; Igaev, M.; Göpfrich, K. Choice of Fluorophore Affects Dynamic DNA Nanostructures. *Nucleic Acids Res.* **2021**, *49* (7), 4186–4195. https://doi.org/10.1093/nar/gkab201.

(19) Hoeher, J. E.; Sande, N. E.; Widom, J. R. Probing and Perturbing Riboswitch Folding Using a Fluorescent Base Analogue. *Photochem. Photobiol. n/a* (n/a). https://doi.org/10.1111/php.13896.

(20) Soulière, M. F.; Haller, A.; Rieder, R.; Micura, R. A Powerful Approach for the Selection of 2-Aminopurine Substitution Sites to Investigate RNA Folding. *J. Am. Chem. Soc.* **2011**, *133* (40), 16161–16167. https://doi.org/10.1021/ja2063583.

(21) Dallmann, A.; Dehmel, L.; Peters, T.; Mügge, C.; Griesinger, C.; Tuma, J.; Ernsting, N. P. 2-Aminopurine Incorporation Perturbs the Dynamics and Structure of DNA. *Angew. Chem. Int. Ed.* **2010**, *49* (34), 5989–5992. https://doi.org/10.1002/anie.201001312.

(22) Mahendran, G.; Jayasinghe, O. T.; Thavakumaran, D.; Arachchilage, G. M.; Silva, G. N. Key Players in Regulatory RNA Realm of Bacteria. *Biochem. Biophys. Rep.* **2022**, *30*, 101276. https://doi.org/10.1016/j.bbrep.2022.101276.

(23) Serganov, A.; Patel, D. J. Molecular Recognition and Function of Riboswitches. *Curr. Opin. Struct. Biol.* **2012**, *22* (3), 279–286. https://doi.org/10.1016/j.sbi.2012.04.005.

(24) Sarkar, B.; Ishii, K.; Tahara, T. Microsecond Folding of preQ1 Riboswitch and Its Biological Significance Revealed by Two-Dimensional Fluorescence Lifetime Correlation Spectroscopy. *J. Am. Chem. Soc.* **2021**, *143* (21), 7968–7978. https://doi.org/10.1021/jacs.1c01077.

(25) Ariza-Mateos, A.; Nuthanakanti, A.; Serganov, A. Riboswitch Mechanisms: New Tricks for an Old Dog. *Biochem. 00062979* **2021**, *86* (8), 962–975. https://doi.org/10.1134/S0006297921080071.

(26) Kallert, E.; Fischer, T. R.; Schneider, S.; Grimm, M.; Helm, M.; Kersten, C. Protein-Based Virtual Screening Tools Applied for RNA–Ligand Docking Identify New Binders of the preQ1-Riboswitch. *J. Chem. Inf. Model.* **2022**, *62* (17), 4134–4148. https://doi.org/10.1021/acs.jcim.2c00751.

(27) Blount, K. F.; Breaker, R. R. Riboswitches as Antibacterial Drug Targets. *Nat. Biotechnol.* **2006**, *24* (12), 1558–1564. https://doi.org/10.1038/nbt1268.

(28) Giarimoglou, N.; Kouvela, A.; Maniatis, A.; Papakyriakou, A.; Zhang, J.; Stamatopoulou, V.; Stathopoulos, C. A Riboswitch-Driven Era of New Antibacterials. *Antibiotics* **2022**, *11* (9), 1243. https://doi.org/10.3390/antibiotics11091243.

(29) Panchal, V.; Brenk, R. Riboswitches as Drug Targets for Antibiotics. *Antibiotics* **2021**, *10* (1), 45. https://doi.org/10.3390/antibiotics10010045.

(30) Leontis, N. B.; Westhof, E. Analysis of RNA Motifs. *Curr. Opin. Struct. Biol.* **2003**, *13* (3), 300–308. https://doi.org/10.1016/S0959-440X(03)00076-9.

(31) Connelly, C. M.; Numata, T.; Boer, R. E.; Moon, M. H.; Sinniah, R. S.; Barchi, J. J.; Ferré-D'Amaré, A. R.; Schneekloth, J. S. Synthetic Ligands for PreQ1 Riboswitches Provide Structural and Mechanistic Insights into Targeting RNA Tertiary Structure. *Nat. Commun.* **2019**, *10* (1), 1501. https://doi.org/10.1038/s41467-019-09493-3.

(32) Frener, M.; Micura, R. Conformational Rearrangements of Individual Nucleotides during RNA-Ligand Binding Are Rate-Differentiated. *J. Am. Chem. Soc.* **2016**, *138* (11), 3627–3630. https://doi.org/10.1021/jacs.5b11876.

(33) Petrone, P. M.; Dewhurst, J.; Tommasi, R.; Whitehead, L.; Pomerantz, A. K. Atomic-Scale Characterization of Conformational Changes in the preQ1 Riboswitch Aptamer upon Ligand Binding. *J. Mol. Graph. Model.* **2011**, *30*, 179–185. https://doi.org/10.1016/j.jmgm.2011.07.006.

(34) Rodger, A. Circular Dichroism and Linear Dichroism. In *Encyclopedia of Analytical Chemistry*; John Wiley & Sons, Ltd, 2014; pp 1–34. https://doi.org/10.1002/9780470027318.a5402.pub2.

(35) Ranjbar, B.; Gill, P. Circular Dichroism Techniques: Biomolecular and Nanostructural Analyses- A Review. *Chem. Biol. Drug Des.* **2009**, *74* (2), 101–120. https://doi.org/10.1111/j.1747-0285.2009.00847.x.

(36) Reich, C.; Maestre, M. F.; Edmondson, S.; Gray, D. M. Circular Dichroism and Fluorescence-Detected Circular Dichroism of Deoxyribonucleic Acid and Poly[d(A-C).Cntdot.d(G-T)] in Ethanolic Solutions: A New Method for Estimating Circular Intensity Differential Scattering. *Biochemistry* **1980**, *19* (23), 5208–5213. https://doi.org/10.1021/bi00564a009.

(37) Johnson, N. P.; Baase, W. A.; von Hippel, P. H. Low-Energy Circular Dichroism of 2-Aminopurine Dinucleotide as a Probe of Local Conformation of DNA and RNA. *P Natl Acad Sci USA* **2004**, *101* (10), 3426–3431.

(38) Kypr, J.; Kejnovska, I.; Renciuk, D.; Vorlickova, M. Circular Dichroism and Conformational Polymorphism of DNA. *Nucleic Acids Res.* **2009**, *37* (6), 1713–1725. https://doi.org/10.1529/biophysj.107.120501.

(39) Johnson, N. P.; Baase, W. A.; von Hippel, P. H. Investigating Local Conformations of Double-Stranded DNA by Low-Energy Circular Dichroism of Pyrrolo-Cytosine. *Proc. Natl. Acad. Sci.* **2005**, *102* (20), 7169–7173. https://doi.org/10.1073/pnas.0502359102.

(40) Datta, K.; Johnson, N. P.; Villani, G.; Marcus, A. H.; von Hippel, P. H. Characterization of the 6-Methyl Isoxanthopterin (6-MI) Base Analog Dimer, a Spectroscopic Probe for Monitoring Guanine Base Conformations at Specific Sites in Nucleic Acids. *Nucleic Acids Res.* **2012**, *40* (3), 1191–1202. https://doi.org/10.1093/nar/gkr858.

(41) Nehira, T.; Ishihara, K.; Matsuo, K.; Izumi, S.; Yamazaki, T.; Ishida, A. A Sensitive Method Based on Fluorescence-Detected Circular Dichroism for Protein Local Structure Analysis. *Anal. Biochem.* **2012**, *430* (2), 179–184. https://doi.org/10.1016/j.ab.2012.08.020.

(42) Turner, D. H.; Tinoco, I. Jr.; Maestre, M. Fluorescence Detected Circular Dichroism. *J. Am. Chem. Soc.* **1974**, *96* (13), 4340–4342. https://doi.org/10.1021/ja00820a057.

(43) Tinoco, I.; Turner, D. H. Fluorescence Detected Circular Dichroism. Theory. *J. Am. Chem. Soc.* **1976**, *98* (21), 6453–6456. https://doi.org/10.1021/ja00437a003.

(44) Castiglioni, E.; Abbate, S.; Lebon, F.; Longhi, G. Chiroptical Spectroscopic Techniques Based on Fluorescence. *Methods Appl. Fluoresc.* **2014**, *2* (2), 024006. https://doi.org/10.1088/2050-6120/2/2/024006.

(45) Christensen, P. L.; Yeung, E. S. Fluorescence-Detected Circular Dichroism for on-Column Detection in Capillary Electrophoresis. *Anal. Chem.* **1989**, *61* (13), 1344–1347. https://doi.org/10.1021/ac00188a009.

(46) Thomas, M.; Patonay, G.; Warner, I. Novel Instrument for Measurement of Multidimensional Fluorescence Detected Circular Dichroism. *Rev. Sci. Instrum.* **1986**, *57* (7), 1308–1313. https://doi.org/10.1063/1.1138594.

(47) Thomas, M. P.; Patonay, G.; Warner, I. M. Fluorescence-Detected Circular Dichroism Studies of Serum Albumins. *Anal. Biochem.* **1987**, *164* (2), 466–473. https://doi.org/10.1016/0003-2697(87)90520-3.

(48) Reich, C.; Tinoco Jr., I. Fluorescence-Detected Circular Dichroism of Dinucleoside Phosphates. A Study of Solution Conformations and the Two-State Model. *Biopolymers* **1980**, *19* (4), 833–848. https://doi.org/10.1002/bip.1980.360190409.

(49) Nehira, T.; Tanaka, K.; Takakuwa, T.; Ohshima, C.; Masago, H.; Pescitelli, G.; Wada, A.; Berova, N. Development of a Universal Ellipsoidal Mirror Device for Fluorescence Detected Circular Dichroism: Elimination of Polarization Artifacts. *Appl. Spectrosc.* **2005**, *59* (1), 121–125.

(50) Ehrenberg, B.; Steinberg, I. Z. Effect of Photoselection on Fluorescence-Detected Circular Dichroism. *J. Am. Chem. Soc.* **1976**, *98* (5), 1293–1295. https://doi.org/10.1021/ja00421a057.

(51) Lobenstine, E. W.; Schaefer, W. C.; Turner, D. H. Fluorescence Detected Circular Dichroism of Proteins with Single Fluorescent Tryptophans. *J. Am. Chem. Soc.* **1981**, *103* (16), 4936–4940. https://doi.org/10.1021/ja00406a044.

(52) Wahl, M.; GmbH, P. Time-Correlated Single Photon Counting. **2009**, *2*.

(53) Hirvonen, L. M.; Nedbal, J.; Almutairi, N.; Phillips, T. A.; Becker, W.; Conneely, T.; Milnes, J.; Cox, S.; Stürzenbaum, S.; Suhling, K. Lightsheet Fluorescence Lifetime Imaging Microscopy with Wide-Field Time-Correlated Single Photon Counting. *J. Biophotonics* **2020**, *13* (2), e201960099. https://doi.org/10.1002/jbio.201960099.

(54) Gelot, T.; Tourón-Touceda, P.; Crégut, O.; Léonard, J.; Haacke, S. Ultrafast Site-Specific Fluorescence Quenching of 2-Aminopurine in a DNA Hairpin Studied by Femtosecond Down-Conversion. *J. Phys. Chem. A* **2012**, *116* (11), 2819–2825. https://doi.org/10.1021/jp212187m.

(55) Rachofsky, E. L.; Osman, R.; Ross, J. B. A. Probing Structure and Dynamics of DNA with 2-Aminopurine: Effects of Local Environment on Fluorescence. *Biochemistry* **2001**, *40* (4), 946–956. https://doi.org/10.1021/bi001664o.

(56) Xu, D.; Evans, K. O.; Nordlund, T. M. Melting and Premelting Transitions of an Oligomer Measured by DNA Base Fluorescence and Absorption. *Biochemistry* **1994**, *33* (32), 9592–9599. https://doi.org/10.1021/bi00198a027.

(57) Guest, C. R.; Hochstrasser, R. A.; Sowers, L. C.; Millar, D. P. Dynamics of Mismatched Base Pairs in DNA. *Biochemistry* **1991**, *30* (13), 3271–3279. https://doi.org/10.1021/bi00227a015.

(58) Cao, S.; Zhou, Z.; Li, H.; Jia, M.; Liu, Y.; Wang, M.; Zhang, M.; Zhang, S.; Chen, J.; Xu, J.; Knutson, J. R. A Fraction of NADH in Solution Is "Dark": Implications for Metabolic Sensing via Fluorescence Lifetime. *Chem. Phys. Lett.* **2019**, *726*, 18–21. https://doi.org/10.1016/j.cplett.2019.04.014.

CHAPTER III: Base-Stacking Heterogeneity

(1) Butcher, S. E.; Pyle, A. M. The Molecular Interactions That Stabilize RNA Tertiary Structure: RNA Motifs, Patterns, and Networks. *Acc. Chem. Res.* **2011**, *44*, 1302–1311. https://doi.org/10.1021/ar200098t.

(2) Lipfert, J.; Doniach, S.; Das, R.; Herschlag, D. Understanding Nucleic Acid–Ion Interactions. *Annu. Rev. Biochem.* **2014**, *83*, 813–841. https://doi.org/10.1146/annurev-biochem-060409-092720.

(3) Draper, D. E. A Guide to Ions and RNA Structure. *RNA* **2004**, *10*, 335–343. https://doi.org/10.1261/rna.5205404.

(4) Olson, W. K.; Li, S.; Kaukonen, T.; Colasanti, A. V.; Xin, Y.; Lu, X.-J. Effects of Noncanonical Base Pairing on RNA Folding: Structural Context and Spatial Arrangements of G·A Pairs. *Biochemistry* **2019**, *58*, 2474–2487. https://doi.org/10.1021/acs.biochem.9b00122.

(5) Jhunjhunwala, A.; Ali, Z.; Bhattacharya, S.; Halder, A.; Mitra, A.; Sharma, P. On the Nature of Nucleobase Stacking in RNA: A Comprehensive Survey of Its Structural Variability and a Systematic Classification of Associated Interactions. *J. Chem. Inf. Model.* **2021**, *61*, 1470–1480. https://doi.org/10.1021/acs.jcim.0c01225.

(6) Yakovchuk, P.; Protozanova, E.; Frank-Kamenetskii, M. D. Base-Stacking and Base-Pairing Contributions into Thermal Stability of the DNA Double Helix. *Nucleic Acids Res.* **2006**, *34*, 564–574. https://doi.org/10.1093/nar/gkj454.

(7) Morozova, N.; Allers, J.; Myers, J.; Shamoo, Y. Protein–RNA Interactions: Exploring Binding Patterns with a Three-Dimensional Superposition Analysis of High Resolution Structures. *Bioinformatics* **2006**, *22*, 2746–2752. https://doi.org/10.1093/bioinformatics/btl470.

(8) Koh, Y. Y.; Wang, Y.; Qiu, C.; Opperman, L.; Gross, L.; Hall, T. M. T.; Wickens, M. Stacking Interactions in PUF–RNA Complexes. *RNA* **2011**, *17*, 718–727. https://doi.org/10.1261/rna.2540311.

(9) Israels, B.; Albrecht, C. S.; Dang, A.; Barney, M.; von Hippel, P. H.; Marcus, A. H. Submillisecond Conformational Transitions of Short Single-Stranded DNA Lattices by Photon Correlation Single-Molecule Förster Resonance Energy Transfer. *J. Phys. Chem. B* **2021**, *125*, 9426–9440. https://doi.org/10.1021/acs.jpcb.1c04119.

(10) Stancik, A. L.; Brauns, E. B. Rearrangement of Partially Ordered Stacked Conformations Contributes to the Rugged Energy Landscape of a Small RNA Hairpin. *Biochemistry* **2008**, *47*, 10834–10840. https://doi.org/10.1021/bi801170c.

(11) Krishnan, R.; Blanco, M. R.; Kahlscheuer, M. L.; Abelson, J.; Guthrie, C.; Walter, N. G. Biased Brownian Ratcheting Leads to Pre-mRNA Remodeling and Capture Prior to First-Step Splicing. *Nat. Struct. Mol. Biol.* **2013**, *20*, 1450–1457. https://doi.org/10.1038/nsmb.2704.

(12) Suddala, K. C.; Wang, J.; Hou, Q.; Walter, N. G. Mg^{2+} Shifts Ligand-Mediated Folding of a Riboswitch from Induced-Fit to Conformational Selection. *J. Am. Chem. Soc.* **2015**, *137*, 14075–14083. https://doi.org/10.1021/jacs.5b09740.

(13) Zhu, J. Y. A.; Meyer, I. M. Four RNA Families with Functional Transient Structures. *RNA Biol.* **2015**, *12*, 5–20. https://doi.org/10.1080/15476286.2015.1008373.

(14) Bood, M.; Füchtbauer, A. F.; Wranne, M. S.; Ro, J. J.; Sarangamath, S.; El-Sagheer, A. H.; Rupert, D. L. M.; Fisher, R. S.; Magennis, S. W.; Jones, A. C. et al., M. Pentacyclic Adenine: A Versatile and Exceptionally Bright Fluorescent DNA Base Analogue. *Chem. Biol.* **2018**, *9*, 3494–3502. https://doi.org/10.1021/ja048514b.

(15) Sandin, P.; Börjesson, K.; Li, H.; Maartensson, J.; Brown, T.; Wilhelmsson, L. M.; Albinsson, B. Characterization and Use of an Unprecedentedly Bright and Structurally Non-Perturbing Fluorescent DNA Base Analogue. *Nucleic Acids Res.* **2007**, *36*, 157–167. https://doi.org/10.1093/nar/gkm1006.

(16) Wilhelmsson, L. M.; Sandin, P.; Holmén, A.; Albinsson, B.; Lincoln, P.; Nordén, B. Photophysical Characterization of Fluorescent DNA Base Analogue, tC. *J. Phys. Chem. B* **2003**, *107*, 9094–9101. https://doi.org/10.1021/jp034930r.

(17) Wilhelmsson, L. M.; Holmén, A.; Lincoln, P.; Nielsen, P. E.; Nordén, B. A Highly Fluorescent DNA Base Analogue That Forms Watson−Crick Base Pairs with Guanine. *J. Am. Chem. Soc.* **2001**, *123*, 2434–2435. https://doi.org/10.1021/ja0025797.

(18) Hawkins, M. E. Fluorescent Pteridine Nucleoside Analogs. *Cell. Biochem. Biophys.* **2001**, *34*, 257–281.

(19) Shin, D.; Sinkeldam, R. W.; Tor, Y. Emissive RNA Alphabet. *J. Am. Chem. Soc.* **2011**, *133*, 14912–14915. https://doi.org/10.1021/ja206095a.

(20) Rovira, A. R.; Fin, A.; Tor, Y. Chemical Mutagenesis of an Emissive RNA Alphabet. *J. Am. Chem. Soc.* **2015**, *137*, 14602–14605. https://doi.org/10.1021/jacs.5b10420.

(21) Ward, D. C.; Reich, E. Fluorescence Studies of Nucleotides and Polynucleotides. *J. Biol. Chem.* **1969**, *244*, 1228–1237. https://doi.org/10.1016/S0021-9258(18)91833-8.

(22) Holmén, A.; Nordén, B.; Albinsson, B. Electronic Transition Moments of 2-Aminopurine. *J. Am. Chem. Soc.* **1997**, *119*, 3114–3121. https://doi.org/10.1021/ja9635600.

(23) Neely, R. K.; Magennis, S. W.; Dryden, D. T. F.; Jones, A. C. Evidence of Tautomerism in 2-Aminopurine from Fluorescence Lifetime Measurements. *J. Phys. Chem. B* **2004**, *108*, 17606–17610. https://doi.org/10.1021/jp0490857.

(24) Somsen, O. J. G.; Hoek, van A.; Amerongen, van H. Fluorescence Quenching of 2-Aminopurine in Dinucleotides. *Chem. Phys. Lett.* **2005**, *402*, 61–65. https://doi.org/10.1016/j.cplett.2004.11.122.

(25) Jones, A. C.; Neely, R. K. 2-Aminopurine as a Fluorescent Probe of DNA Conformation and the DNA-Enzyme Interface. *Q. Rev. Biophys.* **2015**, *48*, 244–279. https://doi.org/10.1017/S0033583514000158.

(26) Jean, J. M.; Hall, K. B. 2-Aminopurine Fluorescence Quenching and Lifetimes: Role of Base Stacking. *Proc. Natl. Acad. Sci.* **2001**, *98*, 37–41. https://doi.org/10.1073/pnas.98.1.37.

(27) Jean, J. M.; Hall, K. B. 2-Aminopurine Electronic Structure and Fluorescence Properties in DNA. *Biochemistry* **2002**, *41*, 13152–13161. https://doi.org/10.1021/bi020308y.

(28) Gelot, T.; Tourón-Touceda, P.; Crégut, O.; Léonard, J.; Haacke, S. Ultrafast Site-Specific Fluorescence Quenching of 2-Aminopurine Studied by Femtosecond Down-Conversion. *J. Phys. Chem. A* **2012**, *116*, 2819–2825. https://doi.org/10.1021/jp212187m.

(29) Bharill, S.; Sarkar, P.; Ballin, J. D.; Gryczynski, I.; Wilson, G. M.; Gryczynski, Z. Fluorescence Intensity Decays of 2-Aminopurine Solutions: Lifetime Distribution Approach. *Anal. Biochem.* **2008**, *377* (2), 141–149. https://doi.org/10.1016/j.ab.2008.03.034.

(30) Fogarty, A. C.; Jones, A. C.; Camp, P. J. Extraction of Lifetime Distributions from Fluorescence Decays with Application to DNA-Base Analogues. *Phys. Chem. Chem. Phys.* **2011**, *13*, 3819–3830. https://doi.org/10.1039/C0CP01779E.

(31) Johnson, N. P.; Baase, W. A.; von Hippel, P. H. Low-Energy Circular Dichroism of 2-Aminopurine Dinucleotide as a Probe of Local Conformation of DNA and RNA. *Proc. Natl. Acad. Sci. USA* **2004**, *101*, 3426–3431.

(32) van Holde, K. E.; Johnson, W. C.; Ho, P. S. *Principles of Physical Biochemistry*, 2nd ed.; Prentice Hall, 2006.

(33) Tinoco, I., Jr; Turner, D. H. Fluorescence Detected Circular Dichroism. Theory. *J. Am. Chem. Soc.* **1976**, *98*, 6453–6456. https://doi.org/10.1021/ja00437a003.

(34) Reich, C.; Tinoco, I. Fluorescence-Detected Circular Dichroism of Dinucleoside Phosphates. A Study of Solution Conformations and the Two-State Model. *Biopolymers* **1980**, *19*, 833–848. https://doi.org/10.1002/bip.1980.360190409.

(35) Xu, D.-G.; Nordlund, T. M. Sequence Dependence of Energy Transfer in DNA Oligonucleotides. *Biophys. J.* **2000**, *78*, 1042–1058. https://doi.org/10.1016/S0006-3495(00)76663-X.

(36) O'Neill, M. A.; Dohno, C.; Barton, J. K. Direct Chemical Evidence for Charge Transfer between Photoexcited 2-Aminopurine and Guanine in Duplex DNA. *J. Am. Chem. Soc.* **2004**, *126*, 1316–1317. https://doi.org/10.1021/ja037802p.

(37) Wan, C.; Fiebig, T.; Schiemann, O.; Barton, J. K.; Zewail, A. H. Femtosecond Direct Observation of Charge Transfer between Bases in DNA. *Proc. Natl. Acad. Sci.* **2000**, *97*, 14052–14055. https://doi.org/10.1073/pnas.250483297.

(38) Khattab, I. S.; Bandarkar, F.; Fakhree, M. A. A.; Jouyban, A. Density, Viscosity, and Surface Tension of Water + Ethanol Mixtures from 293 to 323K. *Korean J. Chem. Eng.* **2012**, *29*, 812–817. https://doi.org/10.1007/s11814-011-0239-6.

(39) Moriyoshi, T.; Ishii, T.; Tamai, Y.; Tado, M. Static Dielectric Constants of Water + Ethanol and Water + 2-Methyl-2-Propanol Mixtures from 0.1 to 300 MPa at 298.15 K. *J. Chem. Eng. Data* **1990**, *35*, 17–20. https://doi.org/10.1021/je00059a005.

(40) Arscott, P. G.; Ma, C.; Wenner, J. R.; Bloomfield, V. A. DNA Condensation by Cobalt Hexaammine(III) in Alcohol–Water Mixtures: Dielectric Constant and Other Solvent Effects. *Biopolymers* **1995**, *36*, 345–364. https://doi.org/10.1002/bip.360360309.

(41) Gunawardhana, S. M.; Holmstrom, E. D. Apolar Chemical Environments Compact Unfolded RNAs and Can Promote Folding. *Biophys. Rep.* **2021**, *1*, 100004. https://doi.org/10.1016/j.bpr.2021.100004.

(42) Jean, J. M.; Hall, K. B. Stacking−Unstacking Dynamics of Oligodeoxynucleotide Trimers. *Biochemistry* **2004**, *43*, 10277–10284. https://doi.org/10.1021/bi049701p.

(43) Somsen, O. J. G.; Keukens, L. B.; de Keijzer, M. N.; van Hoek, A.; van Amerongen, H. Structural Heterogeneity in DNA: Temperature Dependence of 2-Aminopurine Fluorescence in Dinucleotides. *Chem. Phys. Chem.* **2005**, *6*, 1622–1627. https://doi.org/10.1002/cphc.200400648.

(44) Ezra, F. S.; Lee, C.-H.; Kondo, N. S.; Danyluk, S. S.; Sarma, R. H. Conformational Properties of Purine-Pyrimidine and Pyrimidine-Purine Dinucleoside Monophosphates. *Biochemistry* **1977**, *16*, 1977–1987. https://doi.org/10.1021/bi00628a035.

(45) Lee, C.-H.; Ezra, F. S.; Kondo, N. S.; Sarma, R. H.; Danyluk, S. S. Conformational Properties of Dinucleoside Monophosphates in Solution: Dipurines and Dipyrimidines. *Biochemistry* **1976**, *15*, 3627–3639. https://doi.org/10.1021/bi00661a034.

(46) Frechet, D.; Ehrlich, R.; Remy, P.; Gabarro-Arpa, J. Thermal Perturbation Differential Spectra of Ribonucleic Acids. II. Nearest Neighbour Interactions. *Nucleic Acids Res.* **1979**, *7*, 1981–2001. https://doi.org/10.1093/nar/7.7.1981.

(47) Hayatshahi, H. S.; Henriksen, N. M.; Cheatham, T. E. Consensus Conformations of Dinucleoside Monophosphates Described with Well-Converged Molecular Dynamics Simulations. *J. Chem. Theory Comput.* **2018**, *14*, 1456–1470. https://doi.org/10.1021/acs.jctc.7b00581.

(48) Nehira, T.; Tanaka, K.; Takakuwa, T.; Ohshima, C.; Masago, H.; Pescitelli, G.; Wada, A.; Berova, N. Development of a Universal Ellipsoidal Mirror Device for Fluorescence Detected Circular Dichroism: Elimination of Polarization Artifacts. *J. Appl. Spectrosc.* **2005**, *59*, 121–125. https://doi.org/10.1366%2F0003702052940459.

(49) Kolassa, N.; Roos, H.; Pfleger, K. A Separation of Purine Derivatives by Thin-Layer Chromatography on Silica Gel Plates Suitable for Metabolic Studies. *J. Chromatogr. A* **1972**, *66*, 175–177. https://doi.org/10.1016/S0021-9673(01)82946-0.

(50) Greiner, V. J.; Kovalenko, L.; Humbert, N.; Richert, L.; Birck, C.; Ruff, M.; Zaporozhets, O. A.; Dhe-Paganon, S.; Bronner, C.; Mély, Y. Site-Selective Monitoring of the Interaction of the SRA Domain of UHRF1 with Target DNA Sequences Labeled with 2-Aminopurine. *Biochemistry* **2015**, *54*, 6012–6020. https://doi.org/10.1021/acs.biochem.5b00419.

CHAPTER IV: Probing and Perturbing

(1) Sherwood, A. V. and Henkin, T. M. (2016) Riboswitch-mediated gene regulation: Novel RNA architectures dictate gene expression responses. *Annu. Rev. Microbiol.* **70**, 361–374. https://doi.org/10.1146/annurev-micro-091014-104306.

(2) Caron, M.-P., Bastet, L., Lussier, A., Simoneau-Roy, M., Massé, E. and Lafontaine, D. A. (2012) Dual-acting riboswitch control of translation initiation and mRNA decay. *Proc. Natl. Acad. Sci.* **109**, E3444–E3453. https://doi.org/10.1073/pnas.1214024109.

(3) Li, S. and Breaker, R. R. (2013) Eukaryotic TPP riboswitch regulation of alternative splicing involving long-distance base pairing. *Nucleic Acids Res.* **41**, 3022–3031. https://doi.org/10.1093/nar/gkt057.

(4) Rieder, U., Kreutz, C. and Micura, R. (2010) Folding of a transcriptionally acting $PreQ_1$ riboswitch. *Proc. Natl. Acad. Sci. USA* **107**, 10804–10809. https://doi.org/10.1073/pnas.0914925107/-/DCSupplemental/pnas.0914925107_SI.pdf.

(5) Harbaugh, S. V., Goodson, M. S., Dillon, K., Zabarnick, S. and Kelley-Loughnane, N. (2017) Riboswitch-based reversible dual color sensor. *ACS Synth. Biol.* **6**, 766–781. https://doi.org/10.1021/acssynbio.6b00199.

(6) You, M., Litke, J. L. and Jaffrey, S. R. (2015) Imaging metabolite dynamics in living cells using a Spinach-based riboswitch. *Proc. Natl. Acad. Sci. USA* **112**, E2756–E2765. https://doi.org/10.1073/pnas.1504354112.

(7) Jia, X., Zhang, J., Sun, W., He, W., Jiang, H., Chen, D. and Murchie, A. I. H. (2013) Riboswitch control of aminoglycoside antibiotic resistance. *Cell* **152**, 68–81. https://doi.org/10.1016/j.cell.2012.12.019.

(8) Blount, K. F. and Breaker, R. R. (2006) Riboswitches as antibacterial drug targets. *Nat. Biotechnol* **24**, 1558–1564. https://doi.org/10.1038/nbt1268.

(9) Klein, D. J., Edwards, T. E. and Ferré-D'Amaré, A. R. (2009) Cocrystal structure of a class I preQ$_1$ riboswitch reveals a pseudoknot recognizing an essential hypermodified nucleobase. *Nat. Struct. Mol. Biol.* **16**, 343–344. https://doi.org/10.1038/nsmb.1563.

(10) Kang, M., Peterson, R. and Feigon, J. (2009) Structural insights into riboswitch control of the biosynthesis of queuosine, a modified nucleotide found in the anticodon of tRNA. *Mol. Cell* **33**, 784–790. https://doi.org/10.1016/j.molcel.2009.02.019.

(11) Zhang, Q., Kang, M., Peterson, R. D. and Feigon, J. (2011) Comparison of solution and crystal structures of preQ$_1$ riboswitch reveals calcium-induced changes in conformation and dynamics. *J. Am. Chem. Soc.* **133**, 5190–5193. https://doi.org/10.1021/ja111769g.

(12) Widom, J. R., Nedialkov, Y. A., Rai, V., Hayes, R. L., Brooks, C. L., III, Artsimovitch, I. and Walter, N. G. (2018) Ligand modulates cross-coupling between riboswitch folding and transcriptional pausing. *Mol. Cell* **72**, 541–552. https://doi.org/10.1016/j.molcel.2018.08.046.

(13) Suddala, K. C., Rinaldi, A. J., Feng, J., Mustoe, A. M., Eichhorn, C. D., Liberman, J. A., Wedekind, J. E., Al-Hashimi, H. M., Brooks, C. L., III and Walter, N. G. (2013) Single transcriptional and translational preQ$_1$ riboswitches adopt similar pre-folded ensembles that follow distinct folding pathways into the same ligand-bound structure. *Nucleic Acids Res.* **41**, 10462–10475. https://doi.org/10.1093/nar/gkt798.

(14) Suddala, K. C., Wang, J., Hou, Q. and Walter, N. G. (2015) Mg^{2+} shifts ligand-mediated folding of a riboswitch from induced-fit to conformational selection. *J. Am. Chem. Soc.* **137**, 14075–14083. https://doi.org/10.1021/jacs.5b09740.

(15) Sarkar, B., Ishii, K. and Tahara, T. (2021) Microsecond folding of preQ$_1$ riboswitch and its biological significance revealed by two-dimensional fluorescence lifetime correlation spectroscopy. *J. Am. Chem. Soc.* **143**, 7968–7978. https://doi.org/10.1021/jacs.1c01077.

(16) Petrone, P. M., Dewhurst, J., Tommasi, R., Whitehead, L. and Pomerantz, A. K. (2011) Atomic-scale characterization of conformational changes in the preQ$_1$ riboswitch aptamer upon ligand binding. *J. Mol. Graph. Model.* **30**, 179–185. https://doi.org/10.1016/j.jmgm.2011.07.006.

(17) Ward, D. C. and Reich, E. (1969) Fluorescence studies of nucleotides and polynucleotides. *J. Biol. Chem.* **244**, 1228–1237. https://doi.org/10.1016/S0021-9258(18)91833-8.

(18) Widom, J. R. and Hoeher, J. E. (2022) Base-stacking heterogeneity in RNA resolved by

fluorescence-detected circular dichroism spectroscopy. *J. Phys. Chem. Lett.* **13**, 8010–8018. https://doi.org/10.1021/acs.jpclett.2c01778.

(19) Rachofsky, E. L., Osman, R. and Ross, J. B. A. (2001) Probing structure and dynamics of DNA with 2-aminopurine: Effects of local environment on fluorescence. *Biochemistry* **40**, 946–956. https://doi.org/10.1021/bi001664o.

(20) Dallmann, A., Dehmel, L., Peters, T., Mügge, C., Griesinger, C., Tuma, J. and Ernsting, N. P. (2010) 2-Aminopurine incorporation perturbs the dynamics and structure of DNA. *Angew. Chem. Int. Ed.* **49**, 5989–5992. https://doi.org/10.1002/anie.201001312.

(21) Butcher, S. E. and Pyle, A. M. (2011) The molecular interactions that stabilize RNA tertiary structure: RNA motifs, patterns, and networks. *Acc. Chem. Res.* **44**, 1302–1311. https://doi.org/10.1021/ar200098t.

(22) Gaied, N. B., Glasser, N., Ramalanjaona, N., Beltz, H., Wolff, P., Marquet, R., Burger, A. and Mély, Y. (2005) 8-vinyl-deoxyadenosine, an alternative fluorescent nucleoside analog to 2′-deoxyribosyl-2-aminopurine with improved properties. *Nucleic Acids Res.* **33**, 1031–1039. https://doi.org/10.1093/nar/gki253.

(23) Rovira, A. R., Fin, A. and Tor, Y. (2017) Expanding a fluorescent RNA alphabet: synthesis, photophysics and utility of isothiazole-derived purine nucleoside surrogates. *Chem. Sci.* **8**, 2983–2993. https://doi.org/10.1039/C6SC05354H.

(24) Rovira, A. R., Fin, A. and Tor, Y. (2015) Chemical mutagenesis of an emissive RNA alphabet. *J. Am. Chem. Soc.* **137**, 14602–14605. https://doi.org/10.1021/jacs.5b10420.

(25) Soulière, M. F., Haller, A., Rieder, R. and Micura, R. (2011) A powerful approach for the selection of 2-aminopurine substitution sites to investigate RNA folding. *J. Am. Chem. Soc.* **133**, 16161–16167. https://doi.org/10.1021/ja2063583.

(26) Haller, A., Soulière, M. F. and Micura, R. (2011) The dynamic nature of RNA as key to understanding riboswitch mechanisms. *Acc. Chem. Res.* **44**, 1339–1348. https://doi.org/10.1021/ar200035g.

(27) Weeks, K. M. (2010) Advances in RNA structure analysis by chemical probing. *Curr. Opin. Struct. Biol.* **20**, 295–304. https://doi.org/10.1016/j.sbi.2010.04.001.

(28) Hardman, S. J. O., Botchway, S. W. and Thompson, K. C. (2008) Evidence for a nonbase stacking effect for the environment-sensitive fluorescent base pyrrolocytosine—Comparison with 2-aminopurine. *Photochem. Photobiol.* **84**, 1473–1479. https://doi.org/10.1111/j.1751-1097.2008.00368.x.

(29) Roth, A., Winkler, W. C., Regulski, E. E., Lee, B. W. K., Lim, J., Jona, I., Barrick, J. E., Ritwik, A., Kim, J. N., Welz, R., Iwata-Reuyl, D. and Breaker, R. R. (2007) A riboswitch selective for the queuosine precursor preQ$_1$ contains an unusually small aptamer domain. *Nat. Struct. Mol. Biol.* **14**, 308–317. https://doi.org/10.1038/nsmb1224.

(30) Frener, M. and Micura, R. (2016) Conformational rearrangements of individual nucleotides during RNA-ligand binding are rate-differentiated. *J. Am. Chem. Soc.* **138**, 3627–3630. https://doi.org/10.1021/jacs.5b11876.

(31) Schroeder, G. M., Dutta, D., Cavender, C. E., Jenkins, J. L., Pritchett, E. M., Baker, C. D., Ashton, J. M., Mathews, D. H. and Wedekind, J. E. (2020) Analysis of a preQ$_1$-I riboswitch in effector-free and bound states reveals a metabolite-programmed nucleobase-stacking spine that controls gene regulation. *Nucleic Acids Res.* **48**, 8146–8164. https://doi.org/10.1093/nar/gkaa546.

(32) Leontis, N. B. and Westhof, E. (2003) Analysis of RNA motifs. *Curr. Opin. Struct. Biol.* **13**, 300–308. https://doi.org/10.1016/S0959-440X(03)00076-9.

(33) Mergny, J.-L. and Lacroix, L. (2003) Analysis of thermal melting curves. *Oligonucleotides* **13**, 515–537.

(34) Greiner, V. J., Kovalenko, L., Humbert, N., Richert, L., Birck, C., Ruff, M., Zaporozhets, O. A., Dhe-Paganon, S., Bronner, C. and Mély, Y. (2015) Site-selective monitoring of the interaction of the SRA domain of UHRF1 with target DNA sequences labeled with 2-aminopurine. *Biochemistry* **54**, 6012–6020. https://doi.org/10.1021/acs.biochem.5b00419.

(35) Jean, J. M. and Hall, K. B. (2001) 2-Aminopurine fluorescence quenching and lifetimes: Role of base stacking. *Proc. Natl. Acad. Sci.* **98**, 37–41. https://doi.org/10.1073/pnas.98.1.37.

(36) Eichhorn, C. D., Feng, J., Suddala, K. C., Walter, N. G., Brooks, C. L., III and Al-Hashimi, H. M. (2012) Unraveling the structural complexity in a single-stranded RNA tail: implications for efficient ligand binding in the prequeuosine riboswitch. *Nucleic Acids Res.* **40**, 1345–1355. https://doi.org/10.1093/nar/gkr833.

(37) Gong, Z., Zhao, Y., Chen, C., Duan, Y. and Xiao, Y. (2014) Insights into ligand binding to preQ$_1$ riboswitch aptamer from molecular dynamics simulations. *PLOS ONE* **9**, e92247. https://doi.org/10.1371/journal.pone.0092247.

(38) Jerabek-Willemsen, M., André, T., Wanner, R., Roth, H. M., Duhr, S., Baaske, P. and Breitsprecher, D. (2014) MicroScale Thermophoresis: Interaction analysis and beyond. *J. Mol. Struct.* **1077**, 101–113. https://doi.org/10.1016/j.molstruc.2014.03.009.

(39) Bastos, M., Abian, O., Johnson, C. M., Ferreira-da-Silva, F., Vega, S., Jimenez-Alesanco, A., Ortega-Alarcon, D. and Velazquez-Campoy, A. (2023) Isothermal titration calorimetry. *Nat. Rev. Methods Primer* **3**, 1–23. https://doi.org/10.1038/s43586-023-00199-x.

(40) Jean, J. M. and Hall, K. B. (2004) Stacking−unstacking dynamics of oligodeoxynucleotide trimers. *Biochemistry* **43**, 10277–10284. https://doi.org/10.1021/bi049701p.

(41) Somsen, O. J. G., Keukens, L. B., de Keijzer, M. N., van Hoek, A. and van Amerongen, H. (2005) Structural heterogeneity in DNA: Temperature dependence of 2-aminopurine fluorescence in dinucleotides. *Chem. Phys. Chem.* **6**, 1622–1627. https://doi.org/10.1002/cphc.200400648.

(42) Somsen, O. J. G., Hoek, van A. and Amerongen, van H. (2005) Fluorescence quenching of 2-aminopurine in dinucleotides. *Chem. Phys. Lett.* **402**, 61–65. https://doi.org/10.1016/j.cplett.2004.11.122.

(43) Guest, C. R., Hochstrasser, R. A., Sowers, L. C. and Millar, D. P. (1991) Dynamics of mismatched base pairs in DNA. *Biochemistry*, **30**, 3271-3279. https://doi.org/10.1021/bi00227a015

(44) Xu, D., Evans, K. O. and Nordlund, T. M. (1994) Melting and premelting transitions of an oligomer measured by DNA base fluorescence and absorption. *Biochemistry*, **33**, 9591-9599. https://doi.org/10.1021/bi00198a027

(45) Johnson, K. H. and Gray, D. M. (1992) Analysis of an RNA pseudoknot structure by CD spectroscopy. *J. Biomol. Struct. Dyn.* **9**, 733–745.

(46) Burin, A. L., Armbruster, M. E., Hariharan, M. and Lewis, F. D. (2009) Sum rules and determination of exciton coupling using absorption and circular dichroism spectra of biological polymers. *Proc. Natl. Acad. Sci.* **106**, 989–994. https://doi.org/10.1073/pnas.0808513106.

(47) Ji, H., Johnson, N. P., von Hippel, P. H. and Marcus, A. H. (2019) Local DNA base conformations and ligand intercalation in DNA constructs containing optical probes. *Biophys. J.* **117**, 1101–1115. https://doi.org/10.1016/j.bpj.2019.08.006.